

ABSTRACT

Title of Thesis: FORWARD SCATTERING METER FOR VISIBILITY MEASUREMENTS

Nathaniel A. Ferlic, Master of Science in Electrical Engineering, 2019

Thesis Directed By: Directed by Minta Martin Professor of Engineering, Dr. Christopher C. Davis, Electrical and Computer Engineering & Co-Directed by Dr. Miranda Van Iersel, Electrical and Computer Engineering.

Atmospheric aerosols, containing water, constitute most of the air during non-ideal weather conditions including fog, haze, and mist. These aerosols cause light to be attenuated while propagating through the atmosphere causing the effective visibility to decrease. The visibility is dependent on the extinction coefficient of the aerosol distribution that can be found using Mie scattering theory. In the case of a real environment a distribution of particle sizes must be considered where the particles present are described by a weighted value relative to the number density. In this thesis a forward scattering meter is devised that measures the amount of scattered light at a specific forward scattering angle under the assumption that the scattered light is linearly related to the extinction coefficient of different weather conditions. To validate the design, it will be compared against a commercial visibility meter along with using a fog chamber to simulate various weather conditions.

FORWARD SCATTERING METER FOR VISIBILITY MEASUREMENTS

by

Nathaniel A. Ferlic

Thesis submitted to the Faculty of the Graduate School of the
University of Maryland, College Park, in partial fulfillment
of the requirements for the degree of
Master of Science
2019

Advisory Committee:
Professor Christopher C. Davis, Chair/Advisor
Professor Julius Goldhar
Dr. Linda Mullen, U.S. Navy

© Copyright by
Nathaniel A. Ferlic
2019

Dedication

To my dearest Mother
Thank you for everything

Acknowledgements

I would like to start this thesis by saying thanks to my colleagues Dr. Rzasa, Mr. Paulson, and Dr. Wu in the Maryland Optics Group (MOG) at the University of Maryland, College Park for insightful conversations regarding this thesis and other research projects. Also, a thank you for letting me accompany the group to Florida in December 2018. A special thanks goes out to Dr. Christopher Davis, of MOG, for guidance during this thesis. Thank you for everything through the difficult times.

Along with co-directing this thesis I would like to say thank you to Dr. Miranda Van Iersel for taking one of my forward scattering meter designs down to Florida a second time to test it with the TISTEF team from the University of Central Florida (UCF).

Thank you to the University of Central Florida TISTEF team for allowing MOG and I to test our devices on the NASA shuttle landing facility in December 2018 and on the TISTEF range in February 2019. Along with providing visibility data from their Vaisala visibility meter at both tests.

I would like to thank you to Dr. Mullen, from NAVAIR, for putting me in contact with Mr. Novak, from the Naval Research Lab (NRL), along with searching at other research labs for a way to generate aerosols.

A huge thank you goes out to Mr. Novak for taking the time out of his day to let me borrow their fog chamber and helping me take it off base. Along with my past co-worker and friend Mr. Johnson who was kind enough to use a day off to help take me down to NRL and pick up the equipment and take it back to my home.

I would lastly like to thank my loving mother and father for all the guidance and support through the past year. Although times have been extremely difficult, they stuck with me through it all and provided me with much needed assistance in the completion of this project. Along with allowing me to turn the home garage into a fog chamber and home built lab.

Table of Contents

<i>Dedication</i>	<i>ii</i>
<i>Acknowledgements</i>	<i>iii</i>
<i>Table of Contents</i>	<i>iv</i>
<i>List of Tables</i>	<i>vi</i>
<i>List of Figures</i>	<i>vii</i>
<i>Notation</i>	<i>x</i>
Acronyms.....	<i>x</i>
Symbols.....	<i>xi</i>
<i>Chapter 1: Introduction</i>	<i>1</i>
1.1 Background:.....	<i>1</i>
1.2 Commercial Availability.....	<i>3</i>
1.3 Objective:.....	<i>4</i>
1.4 Limitations:.....	<i>5</i>
1.5 Thesis Outline.....	<i>6</i>
<i>Chapter 2: Theory</i>	<i>8</i>
2.1 Attenuation of light: Beer’s Law.....	<i>10</i>
2.2 Extinction in the Atmosphere.....	<i>12</i>
2.3 Absorptive Processes.....	<i>13</i>
2.4 Scattering Processes.....	<i>14</i>
2.5 Particle Scattering: Mie Scattering.....	<i>15</i>
2.5.1 Particle Cross-Sections.....	<i>22</i>
2.5.2 Particle Extinction Efficiencies.....	<i>23</i>
2.5.3 Volume Extinction Coefficients.....	<i>25</i>
2.5.4 Angular Dependence of Scattered Light.....	<i>26</i>
2.5.5 Asymmetry Parameter.....	<i>35</i>
2.5.6 Generalizing Mie Theory to Polydisperse Systems.....	<i>36</i>
2.6 Molecular Scattering: Rayleigh Scattering.....	<i>42</i>
2.7 Visibility During Daytime.....	<i>46</i>
2.8 Visibility at Night: Allard’s Law.....	<i>50</i>
2.9 Visibility in Fog: Wavelength Dependence.....	<i>51</i>
2.10 Meteorological Optical Range.....	<i>53</i>
2.11 Atmospheric Aerosols.....	<i>54</i>
2.11.1 Clouds and Aerosols.....	<i>55</i>
2.11.2 Choice of Aerosol Distributions for Atmospheric Models.....	<i>55</i>
2.11.3 Aerosol Phase Function Characteristics.....	<i>61</i>
Chapter 2 Summary.....	<i>68</i>
<i>Chapter 3: Computation</i>	<i>68</i>
3.1 Single Particle Code.....	<i>71</i>

3.2 Distribution Code.....	76
<i>Chapter 4: Forward Scattering Meter.....</i>	<i>79</i>
<i>Chapter 5: Experimental Design.....</i>	<i>89</i>
5.1 FSM Design One: 2ml Sampling Volume.....	89
5.1.1 Optical Design.....	89
5.1.2 Electronics Design.....	92
5.1.3 Mechanical Design.....	96
5.1.4 Data Processing.....	100
5.1.5 Calibration.....	103
5.2 FSM Design Two: 150ml Sampling Volume.....	104
5.2.1 Optical Design.....	104
5.2.2 Electronics Design.....	105
5.2.3 Mechanical Design.....	105
5.2.4 Data Processing.....	106
<i>Chapter 6: Experimental Verification.....</i>	<i>106</i>
6.1 Florida December 2018: 2ml FSM.....	106
6.2 Florida February 2019: 2ml FSM.....	110
6.3 Qualitative Humidifier Experiment.....	113
6.4 Fog Chamber.....	116
6.4.1 Fog Chamber Distribution Spectra.....	116
6.4.2 Fog Chamber Experiment.....	119
6.5 Outside testing: Design 2.....	127
<i>Chapter 7: Discussion.....</i>	<i>131</i>
7.1 Experimental Results.....	131
7.1.1 2ml FSM Intrinsic Problems and Solutions.....	132
7.1.2 150ml FSM Intrinsic Problems and Solutions.....	133
7.2 Future Work.....	135
7.2.1 Multi-Wavelength Forward Scattering Meter.....	135
7.2.2 Multi-Angle Measurements to Determine Wavelength Dependence of Extinction.....	136
7.2.3 Multi-Angle Single Scattering Phase Function Measurements.....	137
7.2.4 Inclusion of Precipitation.....	138
7.2.5 Image Processing.....	139
7.3 Conclusion.....	139
<i>Appendix.....</i>	<i>142</i>
Mie Scattering Code.....	142
Code for ADS1256 ADC.....	142
References.....	143

List of Tables

Table #:	Description	Page
Table 1:	Visibility for uncontrolled airspace	2
Table 2:	Commercial forward scattering meters	4
Table 3:	Summary of Vision	8
Table 4:	Molecular absorption in the atmosphere	12
Table 5:	Various atmospheric particle sizes	14
Table 6:	Rayleigh cross section calculations	51
Table 7:	Background light dependent visibility	54
Table 8:	Weather dependent extinction	56
Table 9:	Equation summary of chapter two	69
Table 10:	Mie coefficient comparison	73
Table 11:	Mie distribution comparison	78
Table 12:	Comparison of commercial and lab-built FSMs	134

List of Figures

Figure #: Description	Page
Figure 1: Electromagnetic spectrum	9
Figure 2: Atmospheric opacity versus wavelength	10
Figure 3: Depiction of incoming light with cross section highlighted	22
Figure 4: Extinction efficiency for various size particles	25
Figure 5: 1 μm particle phase function and degree of polarization	32
Figure 6: 5 μm particle phase function and degree of polarization	33
Figure 7: Various particle size single scattering phase functions	34
Figure 8: Polar distribution plots for 1 μm and 5 μm particles	35-36
Figure 9: Scattering information for a Gaussian polydisperse system	41-42
Figure 10: Rayleigh particle scattering information	45
Figure 11: Diagram for depicting an observer viewing a target	48
Figure 12: Relative luminous efficiency of the human eye	55
Figure 13: Deirmendjian's aerosol distributions	58
Figure 14: Varying modified gamma distributions	60
Figure 15: Scattering information for cloud C distribution	62-63
Figure 16: Scattering information for a modified gamma distribution	65-66
Figure 17: Scattering information for a haze distribution	68
Figure 18: Logarithmic derivative forward and backwards recursion	72
Figure 19: Comparison of phase function and degree of polarization	74-75
Figure 20: Comparison of polar plots	76

Figure 21: Various phase functions to determine scattering angle	82
Figure 22: Proportionality between scattered intensity and extinction	85-86
Figure 23: Linear best fit for intensity versus extinction	88
Figure 24: Root means squared error versus scattering angle	89
Figure 25: 2 ml optical layout	92
Figure 26: Circuits created for FSMs	94-95
Figure 27: PCB's created for FSMs	96
Figure 28: Raspberry PI with ADS1256	97
Figure 29: 2 ml mechanical enclosure	99
Figure 30: 2 ml back add-on	100
Figure 31: 2 ml optical layout with calibration plate	104
Figure 32: 150 ml optical layout	106
Figure 33: Photo of 150 ml FSM	107
Figure 34: First field test data and experimental setup	109
Figure 35: Second field test experimental setup	111
Figure 36: Second field test experimental data	113
Figure 37: Humidifier setup	115
Figure 38: Humidifier example experiment data run	116
Figure 39: Fog chamber characterization	118-120
Figure 40: Fog chamber setup on March 18 th , 2019	122-123
Figure 41: Fog chamber March 18 th , 2019 example data run	124
Figure 42: Fog chamber March 19 th , 2019 experimental setup	126

Figure 43: Fog chamber March 19 th , 2019 example data run	126
Figure 44: Time-lapse of fog chamber on March 20 th , 2019	127
Figure 45: Fog chamber data run on March 20 th , 2019	128
Figure 46: 150 ml outside experimental setup on March 19 th , 2019	129
Figure 47: 150 ml outside example data run on March 19 th , 2019	130
Figure 48: 150 ml outside during rain on March 21 st , 2019	131

Notation

Acronyms

Acronym	Meaning
ADC	Analog to Digital Converter
AFIT	Air Force Institute of Technology
APSHEL	Atmospheric Propagation Studies for High Energy Lasers Program
EMI	Electromagnetic Interference
FSM	Forward Scatter Meter
HGPF	Heney-Greenstein Phase Function
HTAWS	Helicopter Terrain Awareness and Warning System
IC	Integrated Circuit
ICAO	International Civil Aviation Organization
IR	Infrared
LED	Light Emitting Diode
MOG	Maryland Optics Group
MOR	Meteorological Optical Range
NASA	National Aeronautics and Space Administration
NFET	N-channel Field Effect Transistor
NIR	Near-Infra-Red
NRL	Naval Research Lab
NVIS	Night Vision Imaging System
ONR	Office of Naval Research
PCB	Printed Circuit Board
PLA	Polylactic Acid
PVC	Polyvinyl Chloride
RP	Raspberry PI
SLF	Shuttle Landing Facility
SM	Statute Miles
SM1	1-inch diameter optical tubing
SM2	2-inch diameter optical tubing
SSPF	Single Scattering Phase Function
STL	Stereolithography
TIA	Transimpedance Amplifier
TISTEF	Townes Institute Science and Technology Experimentation Facility
UCF	University of Central Florida
VFR	Visibility Flight Rules
VSF	Volume Scattering Function
WMO	World Meteorological Organization

Symbols

Symbol	Meaning	Units
A	Detector area	m^{-2}
B, B'	Luminance	$cd m^{-2}$
B_H	Background horizon luminance	$cd m^{-2}$
\bar{C}	Contrast	$cd m^{-2}$
C_{atmos}	Atmospheric contrast	$cd m^{-2}$
C_{Ray}	Rayleigh scattering cross-section	m^2
C_{abs}	Absorption cross-section	m^2
C_{ext}	Extinction cross-section	m^2
C_f	Transimpedance feedback capacitance	F
C_{sca}	Scattering cross-section	m^2
$\frac{dC_{sca}}{d\Omega}$	Differential scattering cross-section	$m^2 sr^{-1}$
$D_n(mx)$	Logarithmic derivative	–
E	Illuminance	lux
F_k	King correction function	–
f	Modulation frequency	Hz
g	Asymmetry parameter	–
I	Intensity, specifics will be marked with subscripts	$W m^{-2}$
I_{pd}	Photodiode current	A
$i_j(\theta)$	Angular dependent scattered intensity specified by subscripts	$W m^{-2}$
k	Wave number in media	m^{-1}
$m = n_1 n_0^{-1}$	Relative refraction index	–
N	Particle density	m^{-3}
N_c	Mie series convergence number	–
N_d	Derivative convergence number	–
$n(r)$	Particle distribution in terms of radius	m^{-3}
$n(x)$	Particle distribution in terms of Mie size parameter	–
n_0	Refractive index of media	–
n_1	Refractive index of particles	–
$P_j(\theta)$	Normalized phase function components	–
P_{sca}	Scattered power	W
Q_{abs}	Absorption efficiency	–
Q_{ext}	Extinction efficiency	–
Q_{sca}	Scattering efficiency	–
R_g	Gas radius in King correction function	m
R_f	Transimpedance feedback resistance	Ω

$Resp$	Detector responsibility	AW^{-1}
r	Particle radius	m
r_c	Distribution mean radius	m
V	Visibility	m
V_{sca}	Scattering volume	$ml (cm^{-3})$
Vol_{sca}	Scattering volume	m^3
$x = kr$	Mie Size parameter	—
z	Propagation distance	m
α	Distribution shape parameter	—
δ	De-polarization factor	—
ε	Contrast threshold	—
θ	Scattering angle	$^\circ (Degrees)$
λ	Incident Wavelength	m
$\rho(\theta)$	Normalized scattering phase function	—
$\sigma(\theta)$	Scattering matrix	—
σ_{abs}	Absorption coefficient	km^{-1}
σ_{ext}	Extinction coefficient	km^{-1}
σ_{Ray}	Rayleigh scattering coefficient	km^{-1}
σ_{sca}	Scattering coefficient	km^{-1}
σ_{Aabs}	Aerosol absorption coefficient	km^{-1}
σ_{Asca}	Aerosol scattering coefficient	km^{-1}
σ_{Mabs}	Molecular absorption coefficient	km^{-1}
σ_{Msca}	Molecular scattering coefficient	km^{-1}
τ	Optical depth	—
$d\Omega = \sin(\theta) d\theta d\varphi$	Differential solid angle	sr^{-1}

Chapter 1: Introduction

1.1 Background:

Most of the information taken in on a daily basis is obtained through human's vision through the atmosphere. The eye detects the relative differences in brightness rather than the overall brightness level of an afar object. The distance at which an observer can view an object clearly- is known as visibility. Traditionally visibility has been quantified by holding an ideally black object against a bright background and determining the distance until the object disappears, also known as the contrast threshold. This is done today for aeronautical visibility measurements along with state-of-the-art instrumentation [1]. In the case of underwater visibility, a device called a Secchi disk is used as a black and white target.

Understanding real-time visibility is of utmost concern for aeronautical and general weather knowledge. Aeronautical applications involve knowing the visibility in statute miles (SM), $1 \text{ SM} = 5280 \text{ ft} = 1609\text{m}$, rather than using nautical miles due to the visual flight rules (VFR) being in statute miles. VFR guidelines, in table 1, are what pilots follow to determine if it is safe to fly during adverse weather for corresponding altitude and class of airspace. Airports typically use forward scattering meters in conjunction with transmissometers to obtain real-time visibility data that is then used to determine the flight visibility.

Location	Day		Night		Night using an Approved NVIS or HTAWS	
	Ceiling	Flight Visibility	Ceiling	Flight Visibility	Ceiling	Flight Visibility
Non-mountainous local flying area	800 ft	2 SM	1000 ft	3 SM	800 ft	3 SM
Non-mountainous non-local flying areas	800 ft	3 SM	1000 ft	5 SM	1000 ft	3 SM
Mountainous local flying areas	800 ft	3 SM	1500 ft	3 SM	1000 ft	3 SM
Mountainous non-local flying areas	1000 ft	3 SM	1500 ft	3 SM	1000 ft	5 SM

Table 1: VFR Ceiling and visibility for uncontrolled airspace (class G). NVIS and HTAWS located in the acronyms section (Cornell [2]).

The visibility is also important to know in general for safety concerns for other forms of transportation besides flying. In the case of seafaring applications, it is important to know visibility to prevent ship collisions with the analogous case for drivers to prevent accidents. Thick and light fog can be quantified differently by their visibility which raises the question on how to quantify the real-time visibility practically.

To determine the visibility in real-time becomes a sensing related problem. To sense visibility, one must sense how light is affected by atmospheric conditions. The atmosphere is a complicated medium to travel through due to many different disturbances along the light's path. The disturbances can include temperature, turbulence, wind, cloud cover, precipitation, and pollution. In the case of adverse visibility conditions, the key effects of interest are scattering and absorption of light. In low visibility conditions, the main constituents in the atmosphere are known as aerosols. During foggy weather, water-bearing aerosols are higher in concentrations unlike in polluted conditions, other aerosols such as carbons are present. This thesis

will discuss how atmospheric aerosols affect light and how visibility measurements can be obtained from exploiting these aerosol effects.

1.2 Commercial Availability

To address visibility concerns there were several variants of devices explored in a literature review that included transmissometers, polar nephelometers, integrating nephelometers, and visibility meters. Transmissometers have a light transmitter and an optical receiver that measure the visibility over a long path generally larger than one hundred meters. The light used in transmissometers can vary between using a white light source to a monochromatic laser [3], [4]. Whereas polar and integrating nephelometers sample a much smaller scattering volume that is generally blocked by the device structure or in a closed environment [5] - [9]. Due to the small or enclosed sampling volume, the nephelometer's were not the instrument of choice whereas visibility meters have an open scattering volume. The visibility meter is then chosen to be the commercial design to pursue for this thesis.

To address real-time visibility measurements companies such as Campbell Scientific (CS), Vaisala, and R.M. Young Company (RMYC) have devised high-performance visibility meters. Each of their performance characteristics is described in table 2. The designs presented are a select few of what the commercial market has to offer. The devices are fairly expensive because as their sensitivity increases, as seen for the Vaisala FD12P which is above thirty thousand dollars, their price increases.

Maker	FSM	Range (km)	λ (nm)	Angle (°)	Pulse Rate (kHz)	Sample Volume (L)	Cost (Thousand Dollars)
CS	CS120A	0.01-75	850 LED	42°	1	-	4-6
Vaisala	FD12P	0.01-50	875 LED	33°	2.3	0.1	31
Vaisala	PWD22	0.01-20	875 LED	45°	2	0.1	10.3
RMYC	7300	0.03-16	850 LED	42°	-	-	8-10

Table 2: Commercial visibility meter specifications that are fundamental to their operation taken from their respective user manuals.

The companies follow visibility standards set by the World Meteorological Organization (WMO) and the International Civil Aviation Organization (ICAO) regarding visibility definitions and measurement procedures. By following these procedures their contrast threshold is set to 0.05 which will be discussed in section 2.10. By design, each meter works in all weather conditions including rain and snow. To account for precipitation built-in sensors are used to measure the amount of rain or snowfall. It is important to note that each meter is calibrated by putting a metal plate/screen in the scattering volume with a known, factory calibrated, visibility/extinction value. More information about their design can be read in each of their user manuals that can be found from their designer's respective websites [10], [11], [12], and [13].

1.3 Objective:

The overall goal of this project is to understand how atmospheric aerosols scatter light to measure visibility in non-ideal weather conditions. The objective for this master thesis is to construct a cheaper than commercial forward scatter meter first

principles in order to make accurate visibility measurements when compared to commercial products.

To accomplish this goal a forward scattering meter (FSM) will be produced in order to obtain a measurement for the atmospheric extinction coefficient that can be related to the visibility. This will be done by understanding how water-bearing aerosols, present in visibility limiting conditions, affect light propagation through the atmosphere using electromagnetic theory. Visibility theory for daytime, nighttime, and heavy fog conditions will be discussed due to their fundamental differences. Various assumptions taken into account for the design of the FSM will be presented through the theory considered. The result will provide a cheaper novel approach to measuring the atmospheric extinction coefficient using a lab-developed procedure with full control over the measurement rather than using a commercially available instrument.

It is also noted that the Maryland Optics Group (MOG) has previously built a transmissometer in [3] that this thesis' visibility meter can be compared against. The forward scattering meter is pursued due to the MOG's need for a secondary instrument that is cheaper than a commercial device to compare and calibrate the transmissometer to.

1.4 Limitations:

- Contains only select particle distributions for the weather types chosen which include: clear weather, mist, haze, and fog.
- Measurements will be considered inaccurate in the presence of any precipitation.

- First and second prototype do not include wavelength dependent extinction coefficient for thick fog.
- Small sampling volume of a forward scatter meter only represents a small portion of the, assumed homogeneous, atmosphere.
- Does not measure particle number density or any information about the particle distribution directly except for scattering at a specific angle.

1.5 Thesis Outline

At the start of this thesis acronyms and symbolism adopted by this thesis are presented. This is for reference for confusion with any variable names and acronyms. A summary of each chapter after the introduction is provided below:

Chapter two provides the necessary background to understand the atmospheric effects on the propagation of light. The chapter highlights Mie and Rayleigh scattering, definitions of visibility in daytime, nighttime, and fog, visibility restrictions, absorption of light, and aerosol properties in adverse weather conditions that include haze, mist, and fog.

Chapter three re-iterates scattering theory by presenting a computational method to solve for light scattering off of a single particle which then is generalized to polydisperse systems. The computational methods are then compared to published data to see if they are effective computational techniques.

Chapter four provides the theoretical background of the principle of operation for a forward scattering meter. The calculations in this chapter will be the grounding for the forward scattering meter optical design,

Chapter five guides the reader through the construction procedure of both the 2 ml and 150 ml forward scattering meter designs. The details of the optical design, electronic design, mechanical design, calibration, and signal processing will be discussed in detail.

Chapter six describes various experiments that test the 2ml and 150ml FSM designs and problems faced and how they were solved by each experiment.

Chapter seven gives a summary of the experimental results and what problems arose with each design in more detail and how they were solved. Future directions of the FSM project will also be described to make the device applicable to solving more problems regarding visibility in adverse weather conditions.

Chapter eight will conclude this thesis and provide a summary of what has been accomplished with respect to the thesis objective. The future directions of the project will also be discussed that can be added to the literature.

Chapter 2: Theory

The theory portion of this thesis provides the necessary background on light in general, atmospheric attenuation mechanisms, visibility through the atmosphere, visibility standards, and atmospheric aerosol properties. Each part plays a key role in understanding the physical processes that affect light propagation through the atmosphere in clear and adverse weather conditions. To obtain more information on scattering theory one can reference Bohren and Huffman [14] and Van de Hulst [15] whereas for atmospheric visibility W.E.K Middleton [16].

Visible light is an electromagnetic wave that falls between 380 – 750 nm. The human eye is sensitive at these wavelengths which allows humans to see color. Light is made up of small discrete units of electromagnetic energy called photons. Where shorter wavelengths of light contain higher energy. The eye has two forms of vision called photopic and scotopic which are summarized in table 3. The light condition levels are given in terms of luminance with units of candelas per meter squared. The mesopic vision is the most common vision that is encountered daily since light levels vary during the day [17]. The values in table 1 will be discussed and applied later on in section 2.10.

Vision	Luminance Levels ($cd\ m^{-2}$)	Peak Wavelength (μm)
Photopic	$> 10\ cd\ m^{-2}$	~ 0.500
Scotopic	$< 0.01\ cd\ m^{-2}$	~ 0.550
Mesopic	$0.001\ to\ 3\ cd\ m^{-2}$	$\sim 0.500 - 0.550$

Table 3: Summary of vision type corresponding to luminance levels and peak wavelength

The electromagnetic spectrum, figure 1, encompasses more than just visible light but in this thesis, only the visible and infrared (IR) regions are of importance. The visible range corresponds to visibility since this allows humans to see objects whereas

the IR region cannot be seen by the human eye. The IR region is important for remote sensing applications through the atmosphere as used in this thesis as the final forward scatter meters will use a wavelength at 850 nm. The region between visible and IR light is also known as the near infrared (NIR).

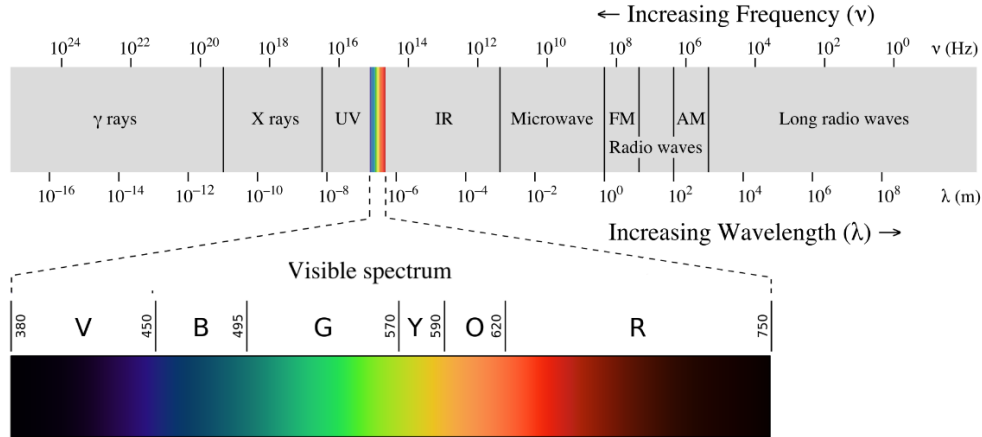


Figure 1: The electromagnetic spectrum where wavelength is given in nm and frequency is given in Hz.

To illuminate an object light must travel from the object to the observer's eye. When outside the light travels through a path in the atmosphere which is an attenuation medium. In figure 2, the atmospheric opacity versus wavelength is plotted in other words – how well different electromagnetic waves can propagate through the atmosphere. If the atmosphere has a high opacity that wavelength cannot propagate well through the atmosphere whereas a small opacity means the wavelength will propagate. As the wavelength increases into the IR and far IR well-known transmission windows open where the atmospheric opacity goes to nearly zero. In the case of visible light and NIR, both are able to propagate but will still be attenuated by various atmospheric mechanisms. The atmosphere is a highly transient environment which can also affect how electromagnetic waves propagate in adverse weather conditions.

Propagation of light through an attenuating medium will be discussed in the next section leading into atmospheric attenuation.

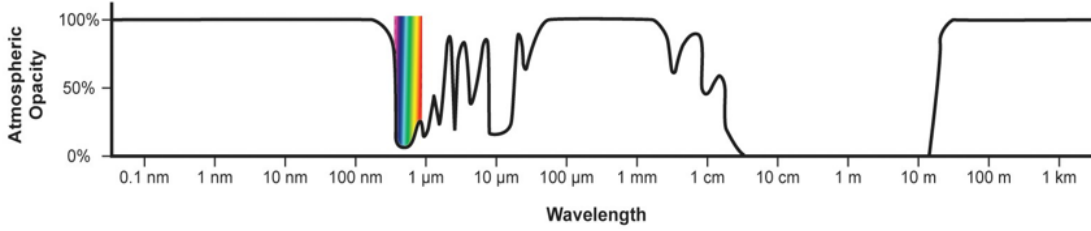


Figure 2: Atmospheric opacity versus wavelength from X-rays to radio waves going left to right.

2.1 Attenuation of light: Beer's Law

To understand how the atmosphere affects laser beam propagation it is important to understand the general case of when a light beam undergoes attenuation in a medium. By modelling the medium as infinitesimally small slabs of particles starting at length z to length $z + dz$ [14], [18]. The change in the intensity, I , of light at z can be related to the amount of light at point $z + dz$ by the extinction coefficient, $\sigma_{ext}(z)$, usually given in inverse kilometers [km^{-1}] as

$$dI = -\sigma_{ext}(z)I dz. \quad (2.1.1)$$

Where the extinction coefficient is defined as:

$$\sigma_{ext} = N C_{ext} = N(C_{abs} + C_{sca}). \quad (2.1.2)$$

Here N is the number density of the particles in inverse cubic meters, C_{ext} is the extinction cross-section, C_{abs} is the absorption cross-section, and C_{sca} is the scattering cross-section. The extinction is made up of both the scattering and absorption of the

medium the light is travelling through. Solving this differential equation, 2.1.1, for, I , using an integration factor the solution becomes:

$$I(z) = I(z_0)e^{-\int_{z_0}^z \sigma_{ext}(z)dz}. \quad (2.1.3)$$

The solution is known as Beer's law. It is generally assumed that the material of interest is homogenous so that the extinction coefficient is independent of where the measurement is made in the material [14]. Thus, Beer's law becomes:

$$I(z) = I(z_0)e^{-\sigma_{ext}z}. \quad (2.1.4)$$

This assumption on the extinction also requires that the measurements are within the limit of $\sigma_{ext}z \ll 1$ which will be noted important later in this chapter. An important term to take away from Beer's law is called optical depth that is the product

$$\tau = \sigma_{ext}z. \quad (2.1.5)$$

When the product is small the attenuating medium is considered optically thin meaning light can propagate with small attenuation. The opposite being an optically thick material when the product is large light propagates with large attenuation.

2.2 Extinction in the Atmosphere

In the atmosphere there exist aerosol particles along with the molecules that add to the scattering and absorption of light. This inclusion of both kinds of particles changes the definition of the extinction coefficient [19]

$$\sigma_{ext} = \sigma_{Mabs} + \sigma_{Msca} + \sigma_{Aabs} + \sigma_{Asca}. \quad (2.2.1)$$

Over short path lengths the effect of molecular absorption can be neglected when in the presence of high concentrations of aerosols. As shown in table 3, for small distances considered in this thesis, the amount of absorption is small compared to the scattering coefficient which is generally three to four orders of magnitude larger. The molecular absorption data in column two of table 3 is provided by [19]. When the path length becomes large, as in kilometers, the effects must be accounted for since the optical depth starts to become comparable to 1. For a small path length, the atmosphere becomes optically thin and the optical depth becomes small (see table 3). This means that in the atmosphere, even on the clearest of days, the total extinction will be limited by the molecular extinction.

Wavelength	Molecular Absorption (dB/km)	τ (1 km)	τ (40 cm)
550	0.13	0.030	7.48E-06
690	0.01	0.0023	5.76E-07
850	0.41	0.094	2.36E-05
1550	0.01	0.0023	5.76E-07

Table 4: Molecular absorption from [19] with calculated optical depth for a kilometer path length and 40cm path length.

The molecular scattering coefficient can also be neglected since molecular scattering can be more than five orders less than aerosol scattering. This can be attributed to the ratio of the particle radius and wavelength which will be discussed in

sections 2.5 and 2.6. The aerosol particles considered in the theory will be assumed spherical as a first approximation but this will introduce errors when particles are aspherical [20]. In general aerosol particles are aspherical which increases the difficulty to determine their effects on light extinction.

The two components that contribute the most are scattering and absorption of aerosols. As previously mentioned in the introduction, aerosols in adverse weather are dominantly water-bearing. Water-bearing aerosols produce larger scattering coefficients since they are less absorptive compared to other aerosols such as carbon-based aerosols.

2.3 Absorptive Processes

Absorption is a wavelength dependent process due to the energy that the photons carry. In the case of molecules, the light is absorbed due to transferring the electromagnetic energy to rotational, translational, vibrational, or electronic processes in the molecule. Absorption is a transfer of energy that does not re-emit the incident light. The main aerosols that absorb light are water, carbon-based molecules, and ozone. The absorption processes of different molecules open up several lines of wavelength where the transmission through the atmosphere is less than 0.2 dB/km in bands between 700-1600 nm shown in figure 2 [19]. Absorption is a factor in choosing the wavelength used in the visibility meter in chapter 4. This thesis will not discuss absorption into full detail due to the importance of scattering processes in this particular application.

2.4 Scattering Processes

The second process light goes through when propagating through a medium is scattering. Scattering processes can be thought of as redirection of the incident light due to an interaction within the medium which is dependent on the composition of the medium. In the atmospheric case, the composition will be aerosol particles and molecules.

Scattering processes affect atmospheric transmission by scattering the light away from the detector which in turn will reduce the performance of the optical system. In the cases of imaging, scattering will affect the measurements due to backscatter into the detector along with forward scattering loss. These processes are highly dependent on the ratio of the size of the particle to the wavelength of light [14]. The various theoretical treatment of particle size can be seen in table 4.

Type	Radius (μm)	Scattering Process
Air Molecules	0.0001	Rayleigh
Haze	0.01 – 1	Rayleigh – Mie
Fog	1 – 20	Mie - Geometrical
Rain	100-10000	Mie - Geometrical
Snow	1000-5000	Geometrical
Hail	5000-50000	Geometrical

Table 5: Atmospheric particle sizes of different forms of water particles in the atmosphere (Kaushal [19]).

The relationship between the size of the particle and wavelength dives into the different theories to describe particle scattering. In this thesis, the particles in question, are aerosols and molecules will most likely be aspheric in nature since the atmosphere is a complex system. To obtain a good first-order approximation of how a plane wave scatters off of these particles they will be assumed to be spherical [14]. The three scattering processes, shown in table 4, for the particle sizes that give the best

approximations. For this thesis, geometrical scattering will not be discussed as it is not found to be applicable to the particle sizes in consideration but Mie scattering can also treat these particles within reason.

2.5 Particle Scattering: Mie Scattering

When the ratio of the size of the particle and wavelength of incident light reaches unity the well-known Mie theory is the appropriate way to treat the problem. Mie theory is used in this project to describe how a plane wave interacts with a spherical particle of refractive index n_1 immersed in a medium of refractive index n_0 . The extinction of a particle depends on the chemical composition (affecting the index of refraction), size, shape, orientation, surrounding medium, number of particles, polarization state of incident light, and frequency of the incident light. This derivation can be found in Bohren and Huffman [14] along with Van de Hulst [15].

The scattering theories presented by each author are in fundamental agreement due to their use of the original Lorenz-Mie-Debye theory better known as Mie theory after Gustav Mie. The differences in presentation lie in how the scattering matrix is presented. Both provide the same normalization of the angular dependence of scattered intensity since Bohren and Huffman [14] base some of their discussion off of Van de Hulst [15]. A reader looking for a computational approach to the problem will be advised to read Bohren and Huffman [14] due to their detailed presentation of the Mie coefficients which can be easily converted to computational Mie code.

To start the derivation a plane wave is incident on the particle with a perpendicular, E_{\perp} , and parallel, E_{\parallel} , component of the electric fields with respect to the scattering plane. The scattering plane is similar to the plane of reflection and

transmission at an interface. This says there are parallel, i_{\parallel} , and perpendicular, i_{\perp} , components of the intensity that can be related to E_{\perp} and E_{\parallel} . The components of the scattered intensity can be described by equation 2.5.1 where the incident intensity can be related to the scattered components with the scattering matrix $\sigma(\theta)$ where \hat{I} is the incident Stokes vector

$$\mathbf{I}(\theta) = I_0 \sigma(\theta) \cdot \hat{\mathbf{I}}. \quad (2.5.1)$$

Equation 2.5.1 can be written out in matrix notation with the elements of the scattering matrix given below in equation 2.5.3. The components of the stokes vector can be related to the electric field that is incident on the particle given by an i subscript for the incident field and the scattered electric field given by an s subscript on each component

$$I = E_{\parallel} E_{\parallel}^* + E_{\perp} E_{\perp}^*. \quad (2.5.2)$$

$$Q = E_{\parallel} E_{\parallel}^* - E_{\perp} E_{\perp}^*$$

$$U = E_{\parallel} E_{\perp}^* + E_{\perp} E_{\parallel}^*$$

$$V = i(E_{\parallel} E_{\perp}^* - E_{\perp} E_{\parallel}^*).$$

The definitions of S_1 and S_2 are in equations 2.5.4 and 2.5.5 used to describe the matrix elements in equation 2.5.3.

$$\begin{pmatrix} I_s \\ Q_s \\ U_s \\ V_s \end{pmatrix} = \frac{1}{k^2 r^2} \begin{pmatrix} S_{11} & S_{12} & 0 & 0 \\ S_{12} & S_{11} & 0 & 0 \\ 0 & 0 & S_{33} & S_{34} \\ 0 & 0 & -S_{34} & S_{33} \end{pmatrix} \begin{pmatrix} I_i \\ Q_i \\ U_i \\ V_i \end{pmatrix} \quad (2.5.3)$$

$$\begin{aligned}
S_{11} &= \frac{1}{2}(|S_2|^2 + |S_1|^2) & S_{12} &= \frac{1}{2}(|S_2|^2 - |S_1|^2) \\
S_{33} &= \frac{1}{2}(S_2^* S_1 + S_2 S_1^*) & S_{34} &= \frac{i}{2}(S_1 S_2^* - S_2 S_1^*)
\end{aligned}$$

The matrix elements are represented as slowly converging infinite sums, S_1 and S_2 , that represent the projection of the scattered electric field on the incident scattering field plane. N_c is defined as the truncation number when the series expansion is considered uniform.

$$S_1 = \sum_{n=0}^{N_c} \frac{2n+1}{n(n+1)} (a_n \pi_n + b_n \tau_n) \quad (2.5.4)$$

$$S_2 = \sum_{n=0}^{N_c} \frac{2n+1}{n(n+1)} (a_n \tau_n + b_n \pi_n) \quad (2.5.5)$$

Both equation 2.5.4 and 2.5.5 are made up of the functions τ_n and π_n , that carry the angular dependence, (see equations 2.5.6 and 2.5.7) with pre-factors a_n and b_n , otherwise known as the Mie coefficients. These are the most important equations in this section since the scattered intensity is written in terms of these functions. The rest of the section describes how to calculate equation 2.5.4 and 2.5.5.

The angular dependence functions are in terms of the associated Legendre polynomials and their first derivative where m is set to 1 due to electric field boundary conditions such that all other higher order polynomials vanish.

$$\pi_n(\cos(\theta)) = \frac{P_n^1(\cos(\theta))}{\sin(\theta)} \quad (2.5.6)$$

$$\tau_n(\cos(\theta)) = \frac{dP_n^1(\cos(\theta))}{d\theta} \quad (2.5.7)$$

$$P_n^m(\cos(\theta)) = (1 - \cos^2(\theta))^{\frac{m}{2}} \frac{d^m P_n(\cos(\theta))}{d(\cos(\theta))^m} \quad (2.5.8)$$

For later computational ease recursive relations can be used to find the terms of τ_n and π_n .

$$\pi_0(\cos(\theta)) = 0 \quad (2.5.9)$$

$$\pi_1(\cos(\theta)) = 1 \quad (2.5.10)$$

$$\pi_n(\cos(\theta)) = \left(\frac{2n-1}{n-1}\right) \cos(\theta) \pi_{n-1} - \left(\frac{n}{n-1}\right) \pi_{n-2} \quad (2.5.11)$$

$$\tau_0(\cos(\theta)) = 0 \quad (2.5.12)$$

$$\tau_1(\cos(\theta)) = \cos(\theta) \quad (2.5.13)$$

$$\tau_n(\cos(\theta)) = n \cos(\theta) \pi_n - (n+1) \pi_{n-1} \quad (2.5.14)$$

The argument, θ , represents the scattering angle where it lies in the range $[0, 180^\circ]$ only because the scattering from $[-180^\circ, 0]$ is assumed to be symmetric. It is also noted that the scattering does not depend on the azimuth angle in spherical coordinates. To continue the derivation of the scattering matrix components the Mie scattering coefficients, a_n and b_n , must be defined.

$$a_n = \frac{m\psi_n(mx)\psi'_n(x) - \psi_n(x)\psi'_n(mx)}{m\psi_n(mx)\xi'_n(x) - \xi_n(x)\psi'_n(mx)} \quad (2.5.15)$$

$$b_n = \frac{\psi_n(mx)\psi'_n(x) - m\psi_n(x)\psi'_n(mx)}{\psi_n(mx)\xi'_n(x) - m\xi_n(x)\psi'_n(mx)} \quad (2.5.16)$$

The functions in equations 2.5.15 and 2.5.16 are known as the Riccati-Bessel functions given in 2.5.17 with an argument of ρ .

$$\psi_n(\rho) = \rho j_n(\rho) \quad (2.5.17)$$

$$\xi_n(\rho) = \rho h_n^1(\rho) \quad (2.5.18)$$

The function $\xi_n(\rho)$ is written in terms of the spherical Hankel functions

$$h_n^1(\rho) = j_n(\rho) + iy_n(\rho). \quad (2.5.19)$$

The spherical Hankel function and $\psi_n(\rho)$ are both written in terms of the spherical Bessel functions of the first and second kind

$$j_n(\rho) = \sqrt{\frac{\pi}{2\rho}} J_{n+\frac{1}{2}}(\rho) \quad (2.5.20)$$

$$y_n(\rho) = \sqrt{\frac{\pi}{2\rho}} Y_{n+\frac{1}{2}}(\rho). \quad (2.5.21)$$

The Stokes parameters of equation 2.5.3 can be related by the equations in 2.5.22 for parallel polarization and equations in 2.5.23 for perpendicular polarization.

$$I_{s\parallel} = (S_{11} + S_{12})I_{i\parallel} \quad (2.5.22)$$

$$Q_{s\parallel} = I_{s\parallel}$$

$$U_{s\parallel} = V_{s\parallel} = 0$$

$$I_{s\perp} = (S_{11} - S_{12})I_{i\perp} \quad (2.5.23)$$

$$Q_{s\perp} = -I_{s\perp}$$

$$U_{s\perp} = V_{s\perp} = 0$$

Then the scattered intensity can be related to the Stokes parameters by equation 2.5.24 and 2.5.8 in terms of the matrix elements in equation 2.5.3. These two equations below represent the scattered irradiance per unit incident irradiance given that the incident light is either parallel or perpendicular to the scattering plane.

$$i_{\parallel} = S_{11} + S_{12} = |S_2|^2 \quad (2.5.24)$$

$$i_{\perp} = S_{11} - S_{12} = |S_1|^2 \quad (2.5.25)$$

With these simplifications to the Stokes parameters the scattering matrix $\boldsymbol{\sigma}(\boldsymbol{\theta})$ can be simplified to equation 2.5.26 with its matrix elements written below.

$$\boldsymbol{\sigma}(\boldsymbol{\theta}) = \frac{1}{r^2} \begin{pmatrix} \sigma_1(\boldsymbol{\theta}) & 0 & 0 & 0 \\ 0 & \sigma_2(\boldsymbol{\theta}) & 0 & 0 \\ 0 & 0 & \sigma_3(\boldsymbol{\theta}) & \sigma_4(\boldsymbol{\theta}) \\ 0 & 0 & -\sigma_4(\boldsymbol{\theta}) & \sigma_3(\boldsymbol{\theta}) \end{pmatrix} \quad (2.5.26)$$

$$\sigma_1(\boldsymbol{\theta}) = \frac{1}{k^2} i_1(\boldsymbol{\theta}) = \frac{1}{k^2} S_1 S_1^*$$

$$\sigma_2(\theta) = \frac{1}{k^2} i_2(\theta) = \frac{1}{k^2} S_2 S_2^*$$

$$\sigma_3(\theta) = \frac{1}{k^2} i_3(\theta) = \frac{1}{2k^2} (S_1 S_2^* + S_2 S_1^*) = \frac{1}{k^2} \text{Re}\{S_1 S_2^*\}$$

$$\sigma_4(\theta) = \frac{1}{k^2} i_4(\theta) = \frac{i}{2k^2} (S_1 S_2^* - S_2 S_1^*) = \frac{-1}{k^2} \text{Im}(S_1 S_2^*)$$

In equation 2.5.27 the scattering matrix is simplified to a 2x2 Mueller matrix in the case when the light is 100% polarized with respect to the scattering plane. The scattered light is taken to be reradiated as a spherical wave that originates at the origin of the spherical particle in question [14].

$$\begin{pmatrix} E_{\parallel s} \\ E_{\perp s} \end{pmatrix} = \frac{e^{ikr(r-z)}}{-ikr} \begin{pmatrix} S_1 & 0 \\ 0 & S_2 \end{pmatrix} \begin{pmatrix} E_{\parallel i} \\ E_{\perp i} \end{pmatrix} \quad (2.5.27)$$

To find the scattered fields the terms of S_1 and S_2 must be computed which are defined in equations 2.5.4 and 2.5.5 and how they are calculated from equations 2.5.6 – 2.5.21. From this point on all the necessary information is known to calculate the scattered fields $E_{\perp s}$ and $E_{\parallel s}$ thus making it possible to calculate the matrix elements of equation 2.5.27. Once the Mie coefficients and matrix elements are known, particle

scattering capabilities can be quantified along with the intensity distribution of the scattered light. The next sub-sections will address this information.

2.5.1 Particle Cross-Sections

Particle cross-sections quantify the total area the light sees perpendicular to the propagation direction and highlighted in figure 3. The particle cross-section is the effective area that scatters the incoming light.

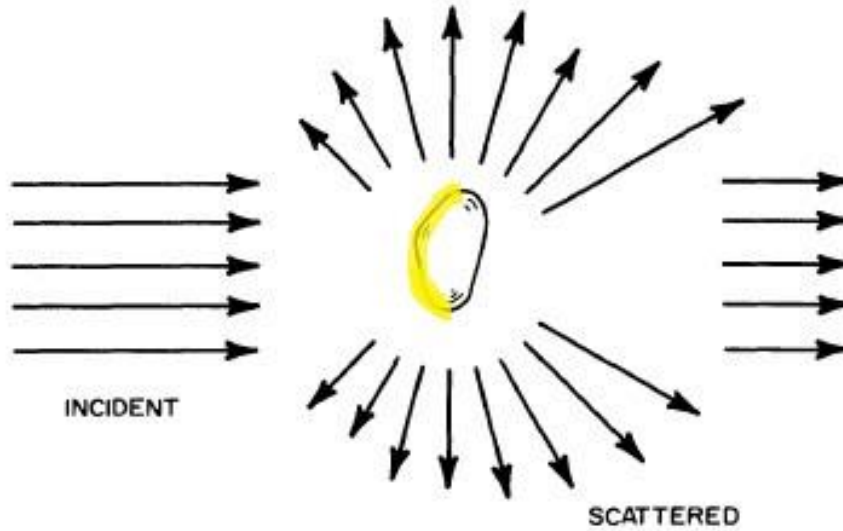


Figure 3: Depiction of incoming laser light on a single arbitrary particle. The highlighted section represents the effective cross-sectional area the incoming light interacts with [14].

The scattering and absorption cross-sections arise from conservation of energy. The total energy scattered in all directions is equal to the energy of the incident wave falling on the scattering cross-section, C_{sca} . Whereas the energy absorbed is that of the incident wave absorbed on the absorption cross-section, C_{abs} . These two coefficients make up the total extinction cross-section given in equation 2.5.28. They will depend on the incident light and particle orientation [15].

$$C_{ext} = C_{abs} + C_{sca} \quad (2.5.28)$$

The scattering and extinction coefficient can be explicitly calculated from Mie theory, equations 2.5.29 and 2.5.30, whereas the absorption coefficient will be found using equation 2.5.28. In the cases of the particle having a real refractive index, $C_{ext} = C_{sca}$, there will be no absorption. Equations 2.5.29 and 2.5.30 are two of the most important equations in describing how a particle interacts with light.

$$C_{ext} = \frac{2\pi}{k^2} \sum_{n=1}^{N_c} (2n + 1) \Re\{a_n + b_n\} \quad (2.5.29)$$

$$C_{sca} = \frac{2\pi}{k^2} \sum_{n=1}^{N_c} (2n + 1) (|a_n|^2 + |b_n|^2) \quad (2.5.30)$$

2.5.2 Particle Extinction Efficiencies

A quantity of interest is how “efficiently” the particle can scatter or absorb light. The efficiency is defined as the particle cross-section divided by the total area of the particle. The term is also used for mathematical simplification. Since each particle has a geometrical cross-section each efficiency factor is represented by

$$Q_{ext} = \frac{C_{ext}}{\pi r^2} \quad (2.5.31)$$

$$Q_{sca} = \frac{C_{sca}}{\pi r^2} \quad (2.5.32)$$

$$Q_{abs} = Q_{ext} - Q_{sca}. \quad (2.5.33)$$

It can be noted that during extinction efficiency calculations the total efficiency can be above a ratio of 1 as shown in figure 4 for different wavelengths. It can be seen that the efficiency asymptotically approaches 2. This raises a question of why the extinction efficiency is greater than 1 since it is a ratio of the effective particle area to the extinction cross-section. This paradox can be argued with scalar diffraction theory and geometrical optics as done by Bohren [14]. Simply put, the particle affects the light in its vicinity due to interference effects of the reradiated light.

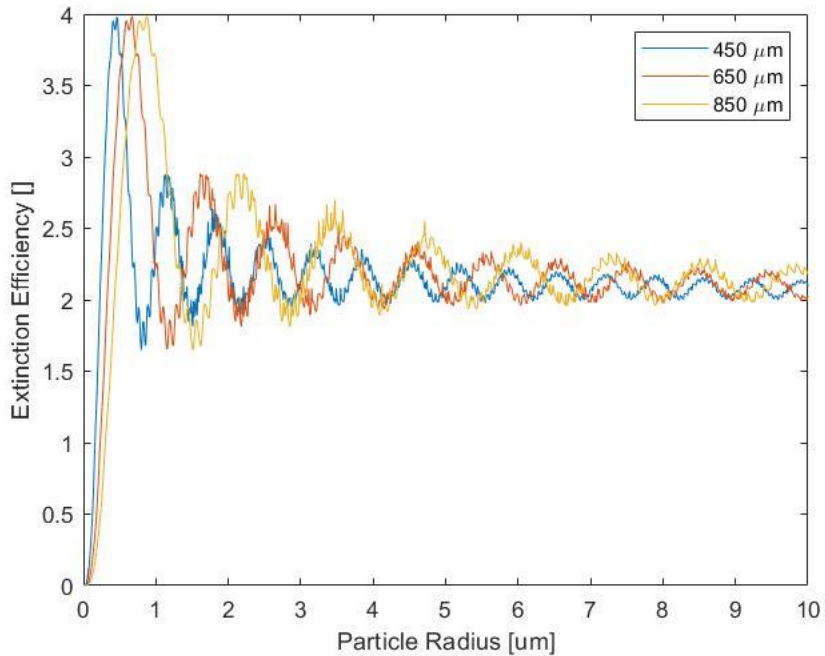


Figure 4: Extinction efficiency for various size particles at 0.450, 0.650, and 0.850 μm . The noticeable ripple effect in extinction efficiency can be seen asymptotically approaching 2.

It can be seen for particles much smaller than the wavelength that the extinction efficiency is small. When the particle radius gets closer to the wavelength the extinction efficiency reaches its maximum of roughly four, meaning that particles equal to the wavelength will scatter light most efficiently. One of these effects can be seen during the sunset. Red light is seen as the sun is lower in the sky due to the blue light being

extinguished more effectively. This is due to the light's path length traveling further through the horizontal atmosphere being scattered off of larger particles which scatter red light better than blue. In the case of water droplets in fog, mist or haze the extinction efficiency is largely from scattering which will be key for the study of aerosols in section 2.11.

2.5.3 Volume Extinction Coefficients

Volume extinction coefficients represent the total extinction by a volume of homogenous or inhomogeneous particles. For the inhomogeneous case of polydisperse systems see section 2.5.6. For the homogenous case the extinction coefficients are [14]

$$\sigma_{ext} = N\pi r^2 Q_{ext} \quad (2.5.34)$$

$$\sigma_{sca} = N\pi r^2 Q_{sca} \quad (2.5.35)$$

$$\sigma_{abs} = N\pi r^2 Q_{abs}. \quad (2.5.36)$$

The volume extinction coefficients are defined in terms of their respective scattering efficiency and the number density, N , given in inverse cubic meters. This value is the same, σ_{ext} , that is defined in section 2.1 where this term appears in the exponential of Beer's Law for atmospheric attenuation. The volume extinction coefficient will be brought back throughout this thesis.

2.5.4 Angular Dependence of Scattered Light

To visualize the angular dependence of the scattered light a plot of angle versus relative intensity is used coined as the phase function¹. This is a misnomer because the graph conveys no information about the complex phase, the only information it carries is how much relative intensity is re-radiated by the particle in the scattering plane. In the case of the atmosphere, it is assumed to be optically homogeneous and isotropic material so then the volume scattering function (VSF) and phase function are azimuthally symmetric [21]. It is noted the particles themselves can be anisotropic which will not affect the symmetry of the VSF or phase function but will affect molecular scattering in section 2.6.

In general, the angular dependence of the scattered light is described by a volume scattering function (VSF) with units of inverse meters inverse steradians. This describes the scattered light per unit volume of scattering medium which also describes multi-scattering processes [22]. To simplify the problem to adopt the single scattering phase function (SSPF) the scattering measurements must be in the regime where $\sigma_{sca}l \ll 1$, where, l , is the path length and σ_{sca} is the volume scattering coefficient.

The SSPF, equation 2.5.37, adopted in this thesis will be that of Van de Hulst [15] but with the added factor of 4π for normalization as Deirmendjian [21].

¹ The term originated in astronomy where the “phase angle” is the direction of light hitting objects in space. The term “phase” came from the sunlight being reflected by the moon depending on the phase of the moon hence “phase function” [22].

$$\rho(\theta) = \frac{4\pi}{C_{sca}} \frac{dC_{sca}}{d\Omega} \quad (2.5.37)$$

Where the differential scattering cross-section, $dC_{sca}/d\Omega$, is the energy scattered per unit time into a unit solid angle per unit incident irradiance and C_{sca} is the scattering cross-section. The phase function can be thought of as a probability distribution of where each photon of incident light will be scattered to. The normalization of the probability distribution is the scattering cross-section.

To obtain the normalization there are two procedures to go through the first being that the intensity should go to that of the source, I_s , for small source unit solid angle, $\Delta\omega_0$, and the second is that the scattering cross-section must be normalized around a unit solid angle $\Delta\omega$. To start the normalization the scattered intensity is given by $I(\theta)$ for small unit solid angle and then taking the limit of equation 2.5.38 for small source solid angle.

$$I(\theta)\Delta\omega = I_0\sigma(\theta) \cdot \hat{I}\Delta\omega_0\Delta\omega \quad (2.5.38)$$

$$\lim_{\Delta\omega_0 \rightarrow 0} I_0\Delta\omega_0 = I_{source} \quad (2.5.39)$$

After equation 2.5.39 is satisfied, equation 2.5.38 can be rewritten in terms of the incident intensity which is given in equation 2.5.1 initially. It can be noted that equation 2.5.1, restated below, can be thought of as a matrix transformation of the Stokes vectors scaled by the incident intensity

$$\mathbf{I}(\boldsymbol{\theta}) = I_0 \boldsymbol{\sigma}(\boldsymbol{\theta}) \cdot \hat{\mathbf{I}}. \quad (2.5.1)$$

The second normalization condition is that $I_1 + I_2 = I_0$ for any incident polarization of light where I_0 is the incident intensity. Using the expressions that the scattering cross-section must be normalized over all solid angle, in equation 2.5.40 the normalization condition can be found to be

$$C_{sca}(m, x) = \int_{\Omega} d\sigma(m, x, \theta) = \frac{1}{2k^2} \int_{\Omega} (S_1 S_1^* + S_2 S_2^*) d\omega. \quad (2.5.40)$$

Then by replacing the scattering cross-section with the scattering efficiency the condition is found

$$1 = \frac{1}{4\pi} \int_{\Omega} \frac{2}{x^2 Q_{sca}(x)} (i_1(\theta) + i_2(\theta)) d\omega. \quad (2.5.41)$$

The scattering matrix in equation 2.5.26 can be rewritten in terms of the normalized phase function components.

$$P_j(\theta) = \frac{4i_j(\theta)}{x^2 Q_{sca}(x)} = \frac{4\sigma_j(\theta)}{r^2 Q_{sca}(x)} \quad (2.5.42)$$

$$\boldsymbol{\sigma}(\boldsymbol{\theta}) = \frac{\pi r^2 Q_{sca}(x)}{4\pi} \begin{pmatrix} P_1(\theta) & 0 & 0 & 0 \\ 0 & P_2(\theta) & 0 & 0 \\ 0 & 0 & P_3(\theta) & P_4(\theta) \\ 0 & 0 & -P_4(\theta) & P_3(\theta) \end{pmatrix} \quad (2.5.43)$$

Now in terms of the normalized phase function the original equations in equation 2.5.1 can be rewritten as

$$\mathbf{I}(\boldsymbol{\theta}) = I_0 \sigma_{sca} \frac{\mathbf{P}(\boldsymbol{\theta})}{4\pi} \cdot \hat{\mathbf{I}}. \quad (2.5.44)$$

In the case of unpolarized light the differential scattering cross-section can be defined by equation 2.5.45. Where the phase function then becomes 2.5.45.

$$\frac{dC_{sca}}{d\Omega} = \frac{(i_{\perp} + i_{\parallel})}{2k^2} \quad (2.5.45)$$

$$\rho(\theta) = \frac{4\pi}{C_{sca}} \frac{(i_{\perp} + i_{\parallel})}{2k^2} = \frac{4}{x^2 Q_{sca}} \frac{(i_{\perp} + i_{\parallel})}{2}$$

$$\frac{\rho(\theta)}{4\pi} = \frac{1}{C_{sca}} \frac{i_{\perp} + i_{\parallel}}{2k^2} \quad (2.5.46)$$

In the case of unpolarized light the normalized SSPF will take on the form in equation 2.5.47 written in terms of the normalized matrix elements. The SSPF can also be normalized to the extinction cross-section or scattering cross-section depending on what physical quantity is being measured. If the incident light is perpendicularly or parallel polarized with respect to the scattering plane then the phase function will only be represented by a single normalized matrix element $P_1(\theta)$ and $P_2(\theta)$ respectively.

$$\rho_{unpol}(\theta) = \frac{1}{2} \left(\frac{P_1(\theta)}{4\pi} + \frac{P_2(\theta)}{4\pi} \right). \quad (2.5.47)$$

An interesting quantity that can be measured is called the degree of polarization, related to the phase function, defined in equation 2.5.48.

$$P = -\frac{S_{12}}{S_{11}} = \frac{i_{\perp} - i_{\parallel}}{i_{\perp} + i_{\parallel}} \quad (2.5.48)$$

Equation 2.5.48 is the ratio of the matrix elements given in equation 2.5.3 but rewritten in terms of the perpendicular and parallel unit irradiance. The degree of polarization is useful to visualize how much of the scattered light at each angle is polarized in each direction. If P is positive, the scattered light is more polarized perpendicular to the scattering plane and if P is negative, the scattered light is more polarized parallel to the scattering plane. There will be no discussion on circularly polarized light but is continued in Bohren [14].

To demonstrate the angular dependence of scattered light from spherical particles, figures 5-7 contain SSPF's for single particles along with the degree of polarization. As the particle radius increases the number of interference lobes increase with the main scattering peak increases in magnitude meaning as particles get large their forward-peaked scattering becomes more dominant. In figure 5 and 7 single particles with 1 μm and 5 μm radii respectively are plotted to show how the scattered light depends on the polarization of the incoming light.

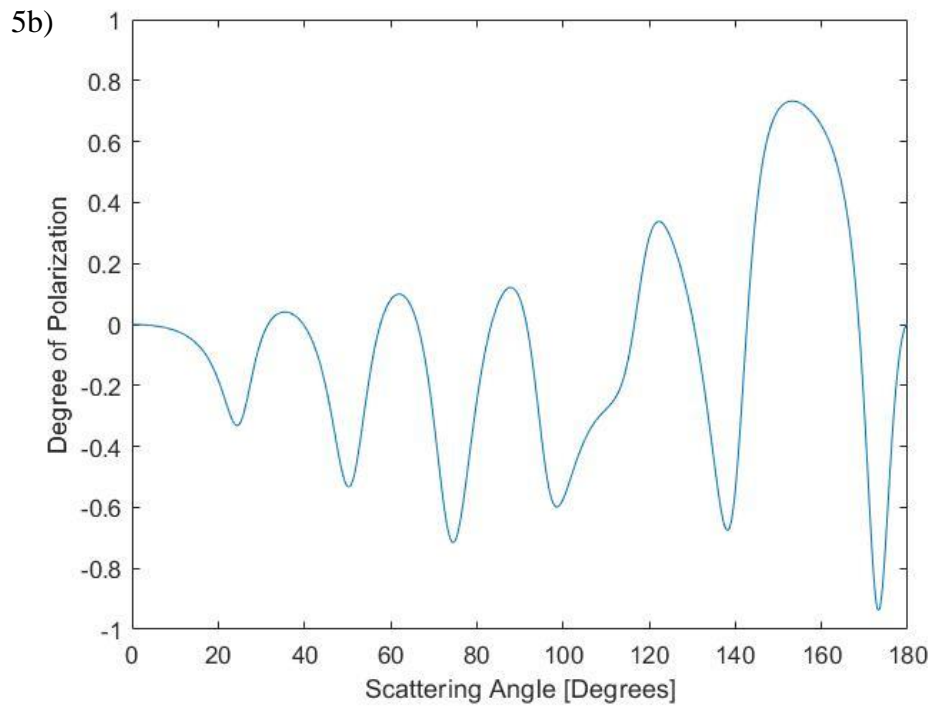
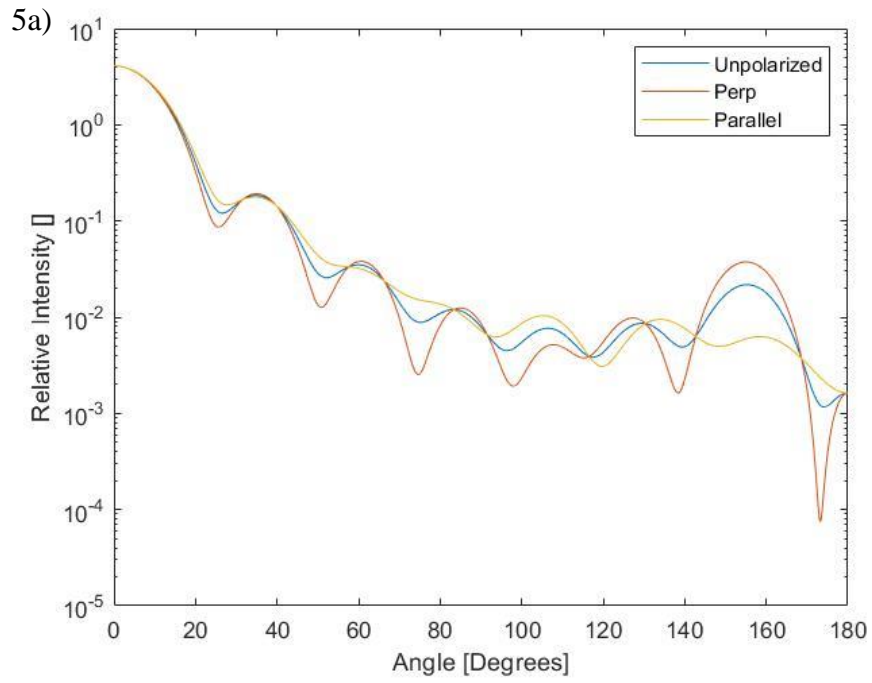


Figure 5: Plot of SSPF for a $1\mu\text{m}$ particle radius (5a) with perpendicular, parallel, and unpolarized incident light. with degree of polarization (5b). The parameters are $\lambda = 0.850\ \mu\text{m}$, $n_0 = 1$, and $n_1 = 1.335$.

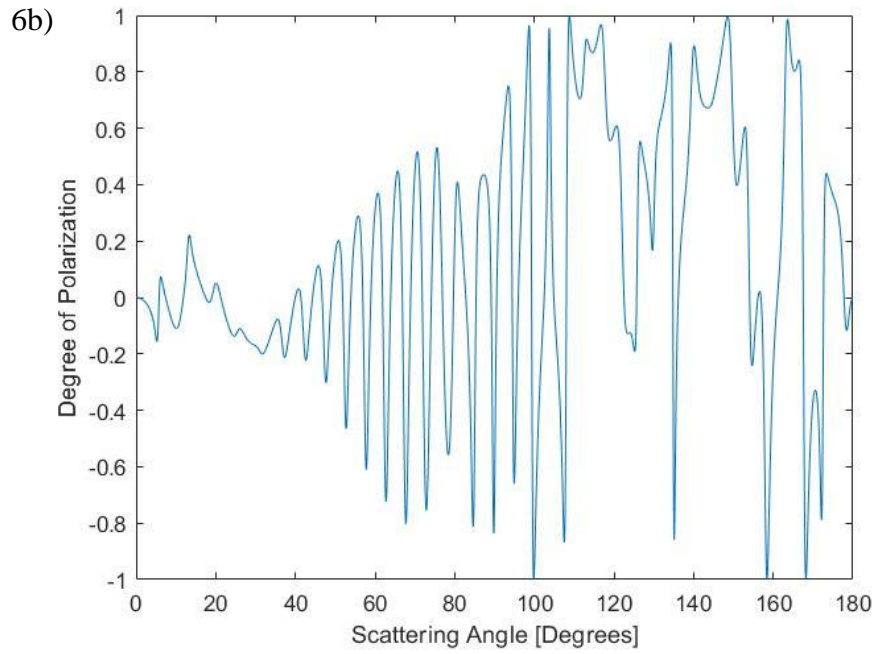
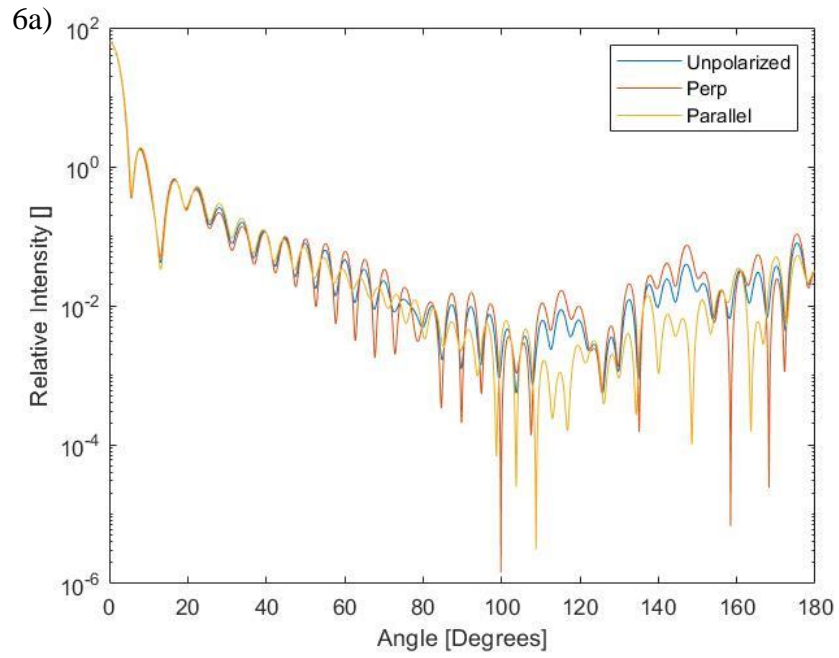


Figure 6: Plot of SSPF for a $5\mu\text{m}$ particle radius with perpendicular, parallel, and unpolarized incident light (6a) with degree of polarization (6b). The parameters are $\lambda = 0.850\mu\text{m}$, $n_0 = 1$, $n_1 = 1.335$.

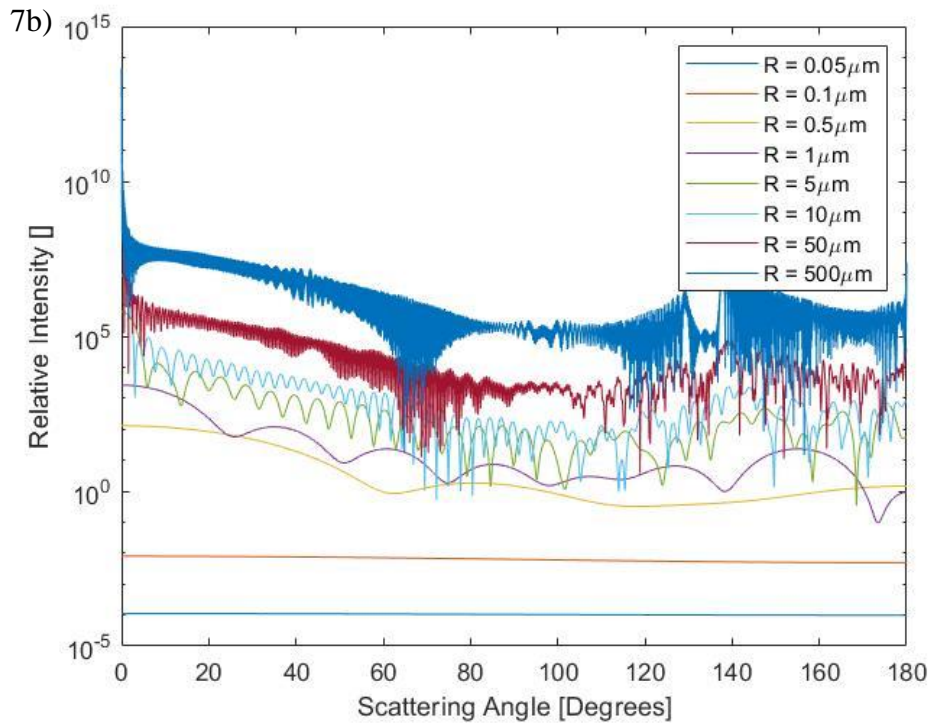
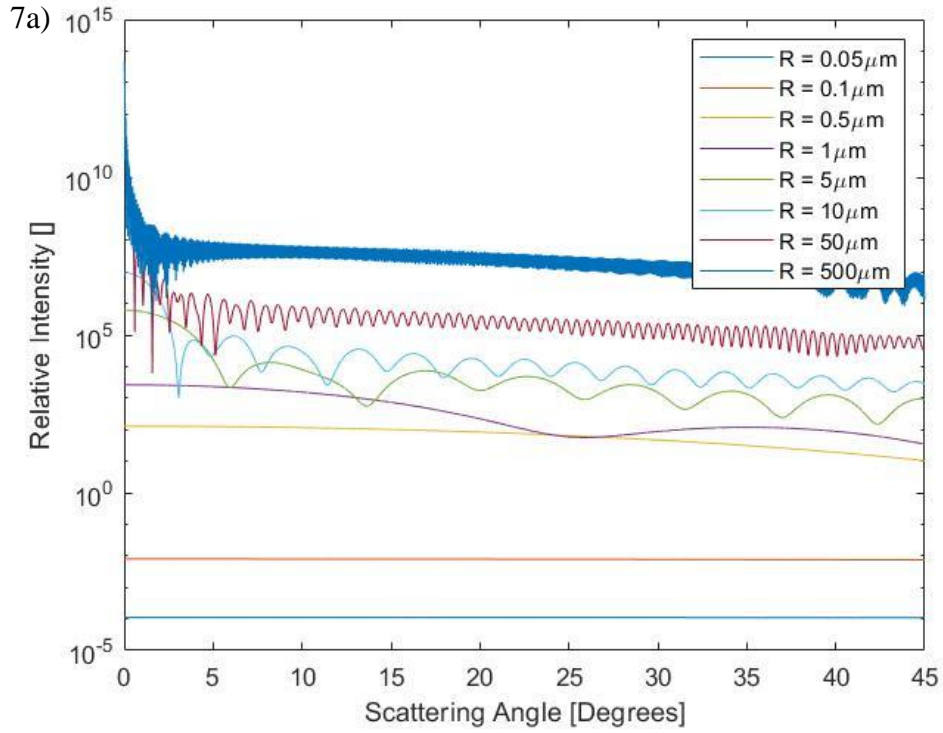
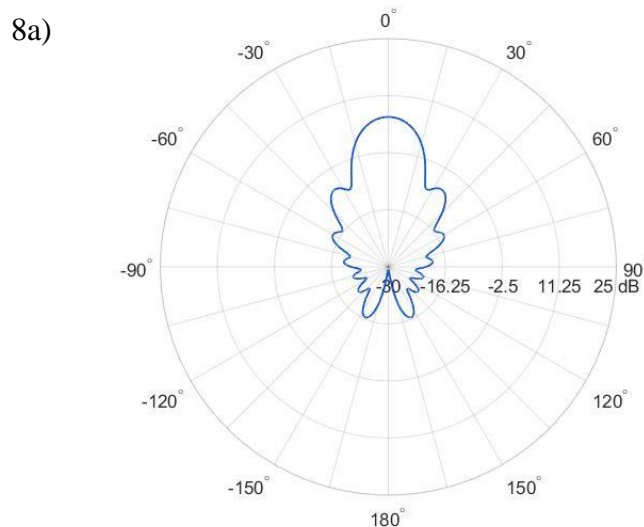


Figure 7: Comparison of phase functions for large particles and small particle radii between scattering angles $0-180^\circ$ (7a) with a plot of small scattering angles between $0-45^\circ$ (7b). Parameters used are $\lambda = 0.850 \mu\text{m}$, $n_0 = 1$, and $n_1 = 1.335$. As the particle size increases the forward scattering peak and structure of the SSPF increase.

In figures 5a and 6a, the forward scattering at 0° can be seen to increase as along with the diffraction effects as the particle size gets larger than the wavelength. The degree of polarization can also be seen to oscillate between parallel and perpendicular polarized scattered light. Figure 7a and 7b display various SSPF's for various particle radii with unpolarized incident light at $0.850\mu\text{m}$. The particles at $0.05\mu\text{m}$ and $0.1\mu\text{m}$ are considered Rayleigh scatterers since their scattering symmetry is throughout all scattering angles. As the particle size increases to $0.5\mu\text{m}$ and greater diffractive effects can be seen as the phase function gains structure in figure 7b. Once the particle size is much larger most light is scattered in the forward direction. Another useful way to visualize the angular scattering dependence is to plot the scattered radiation on a polar plot in decibels as in figure 8. The structure at each angle is easier to visualize if thought as the pattern around an oscillating dipole.



8b)

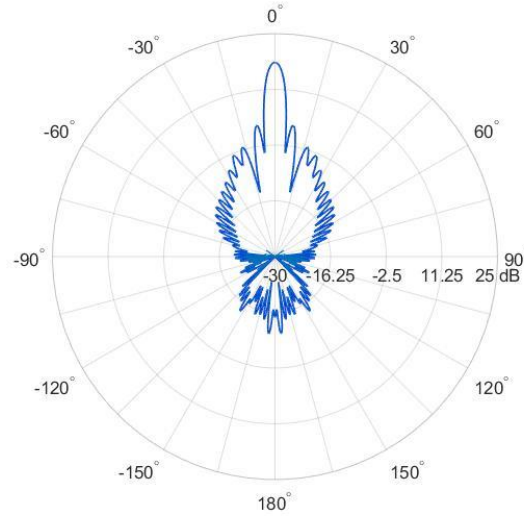


Figure 8: To the top (8a) is the $1\mu\text{m}$ radius polar scattering pattern and (8b) is the $5\mu\text{m}$ radius polar scattering pattern. Notice the stronger forward scattering for the Mie particles and backward scattering magnitudes are greater than other angles.

2.5.5 Asymmetry Parameter

The phase functions in the previous section can be seen to have a distinct shape depending on the particle size compared to wavelength in figures 5-7. The shape can be represented by the dimensionless asymmetry parameter g sometimes called the form-factor. The definition of g is the same as Bohren [14] and Van De Hulst [15] in equation 2.5.49. For ease of computational applications equation 2.5.59 can be rewritten in terms of a truncated series of the Mie coefficients in equations 2.5.4 and 2.5.5 that becomes equation 2.5.50.

$$g = \langle \cos(\theta) \rangle = \int_{4\pi} \rho(\theta) \cos(\theta) d\Omega \quad (2.5.49)$$

$$d\Omega = \sin(\theta) d\theta d\phi$$

$$g = \frac{4}{x^2 Q_{sca}} \sum_{n=1}^{N_c} \left(\frac{n(n+2)}{n+1} \Re\{a_n a_{n+1}^* + b_n b_{n+1}^*\} + \frac{2n+1}{n(n+1)} \Re\{a_n b_n^*\} \right) \quad (2.5.50)$$

The asymmetry parameter can be thought of as the phase function averaged over a cosine function for unit solid angle. It describes if the phase function is more favored towards forward scattering or backward scattering. When g is positive, the phase function favors forward scattering whereas if g is negative the phase function favors backward scattering. If g is close to zero there is no specific direction the scattered light is reradiated in, which points to the limit of Rayleigh scattering.

2.5.6 Generalizing Mie Theory to Polydisperse Systems

In the case of a system with many different particle sizes present the system, assumed to be spherical particles, will be represented by a distribution. A system of this nature is said to be polydisperse. A polydisperse system is considered because in reality particles will not take on the same size. Particles will be formed to various sizes and when considering atmospheric aerosols in fog mist and haze this will be the case. The following generalization of Mie theory to a polydisperse system will be used in chapter 3 and 4. The theory presented in Bohren [14] and Van de Hulst [15] discusses polydisperse systems briefly but two reports by Deirmendjian [21], [23] explicitly dealt with these systems. The and normalization from Deirmendjian is found easier to apply to aerosol distributions along with the relationship between the phase function and intensity expression in equation 2.5.1. A cross between the three different ways to approach scattering theory was decided upon for this thesis for the ease of calculating

the scattering intensity explicitly since that is a measurable phenomenon, unlike the SSPF.

In general, when a system contains particles with discrete sizes the results of scattering theory that depend on the number density of particles will be replaced with summations over the particle distributions. But noted in [21] it is more precise to replace the summations with integrals due to the particle distributions being continuous. The number density, N , of a distribution for all radii in the particle model will take on the form as given in equation 2.5.51, when $n(r)$ is taken as a continuous distribution. The number density can be thought of a normalization parameter.

$$N = \int_0^{\infty} n(r) dr = \frac{1}{k} \int_0^{\infty} n(x) dx \quad (2.5.51)$$

In this thesis the distributions will be written in terms of the particle radius. But in the literature the distributions are also re-written in terms of the size parameter x which leads to normalization confusion. The terms that will be useful later on are rewritten in terms of the particle distribution $n(r)$. Equations 2.5.52 - 2.5.57 represent the effective extinction cross-section, extinction coefficient, and extinction efficiency. The integral over the particle distribution can be thought of as a weighted average of the specific extinction parameter being found.

$$C_{ext} = \int_0^{\infty} \frac{2\pi}{k^2} \sum_{n=1}^{N_c} (2n + 1) \Re\{a_n + b_n\} n(r) dr \quad (2.5.52)$$

$$Q_{ext} = \int_0^{\infty} \frac{C_{ext}(r)}{\pi r^2} n(r) dr \quad (2.5.53)$$

$$\sigma_{ext} = \int_0^{\infty} \pi r^2 Q_{ext}(r) n(r) dr = \frac{\pi}{k^3} \int_0^{\infty} x^2 Q_{ext}(x) n(x) dx \quad (2.5.54)$$

$$C_{sca} = \int_0^{\infty} \frac{2\pi}{k^2} \sum_{n=1}^{N_c} (2n+1)(|a_n|^2 + |b_n|^2) n(r) dr \quad (2.5.55)$$

$$Q_{sca} = \int_0^{\infty} \frac{C_{sca}(r)}{\pi r^2} n(r) dr \quad (2.5.56)$$

$$\sigma_{sca} = \int_0^{\infty} \pi r^2 Q_{sca}(r) n(r) dr = \frac{\pi}{k^3} \int_0^{\infty} x^2 Q_{sca}(x) n(x) dx \quad (2.5.57)$$

The normalized matrix elements are redefined in terms of the particle distribution which will take the form of equation 2.5.58 after the numerator and denominator of equation 2.5.42 are multiplied by $\pi n(r)$ and integrated over all radii.

$$P_j(\theta) = \frac{4\pi \int_0^{\infty} i_j(\theta) n(r) dr}{k^2 \int_0^{\infty} Q_{ext} n(r) \pi r^2 dr} = \frac{4\pi}{k^2 \sigma_{ext}} \int_0^{\infty} i_j(\theta) n(r) dr$$

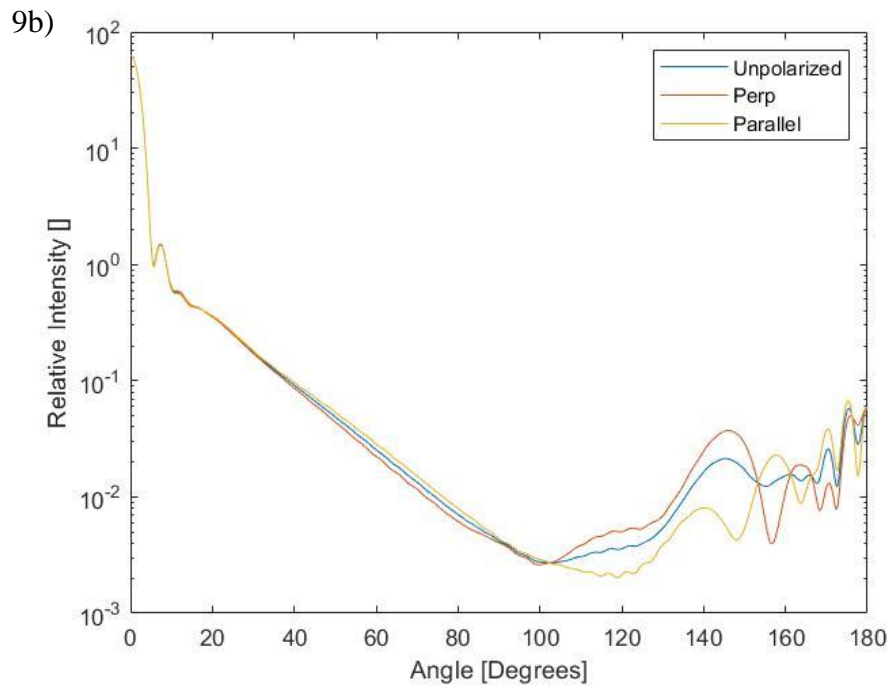
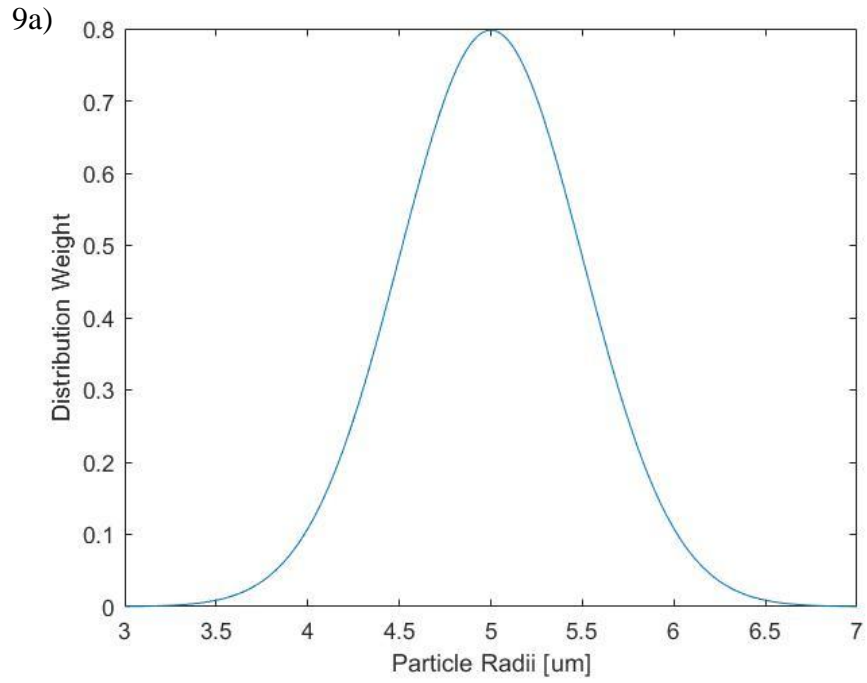
$$\frac{P_j(\theta)}{4\pi} = \frac{1}{k^2 \sigma_{sca}} \int_0^{\infty} i_j(\theta) n(r) dr \quad (2.5.58)$$

The unpolarized phase function is still of interest in a polydisperse system which will still take on the form of equation 2.5.47. When equation 2.5.47 is rewritten in terms of the weighted normalized matrix elements given in equation 2.5.58 equation 2.5.59 is obtained

$$\rho_{unpol}(\theta) = \frac{1}{k^2 \sigma_{sca}} \int_0^\infty \frac{i_1(\theta) + i_2(\theta)}{2} n(r) dr. \quad (2.5.59)$$

Although only the unpolarized phase function is given in equation 2.5.59 if the incident light is perpendicular or parallel polarized the same procedure follows for a polydisperse system as a single particle. A single normalized matrix element will be used to describe the phase function instead of a linear combination.

For the following Gaussian distribution of particles, given in figure 9a, the mean particle radius is given to be $5\mu\text{m}$ with a standard deviation of $0.5\mu\text{m}$. The phase function, figure 9b, can be seen to have three diffraction peaks with a smooth drop off. Particle distributions have smoother scattering patterns due to the scattered light from various particle sizes adding constructively and destructively. This will be observed later on again with aerosol distribution pattern.



s.

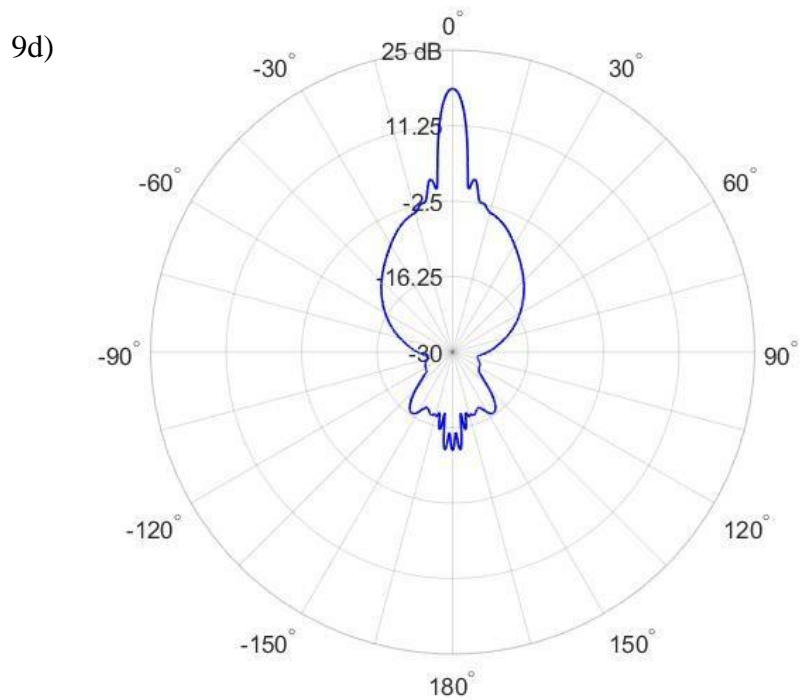
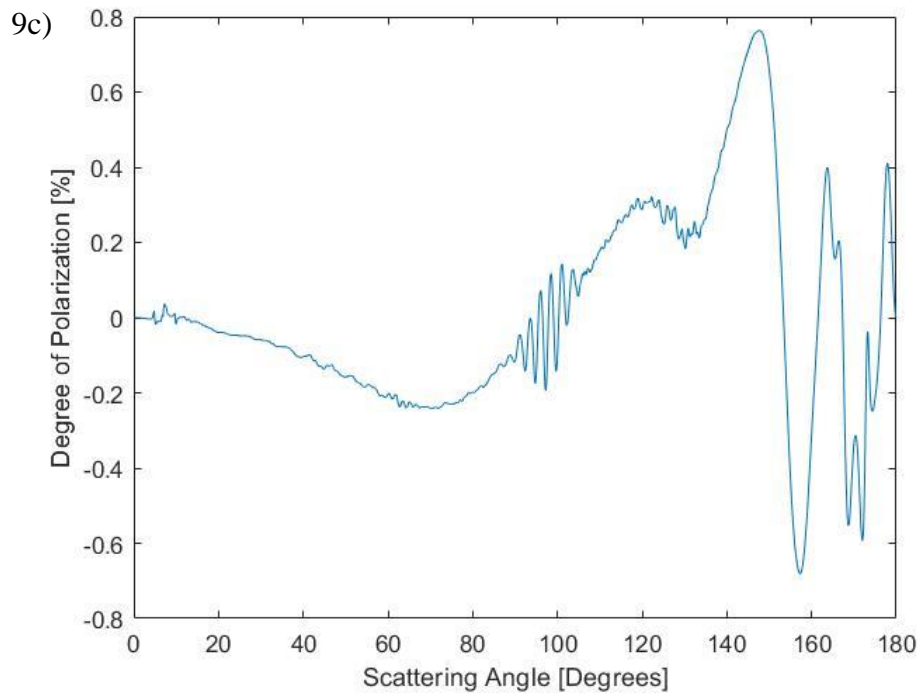


Figure 9: Gaussian distribution (9a) used to generate the phase function (9b) with a particle mean of $5\mu\text{m}$ and a standard deviation of $0.5\mu\text{m}$. (9c) Degree of polarization for a distribution given in percent instead on the range of -1 to 1 . (9d) Polar plot of the scattered light of the distribution clearly showing forward and backward scattering peaks whereas the rest of the angles are flat. The wavelength is $0.850\mu\text{m}$ with a particle index of refraction of 1.335 .

2.6 Molecular Scattering: Rayleigh Scattering

In section 2.5 Mie theory is discussed that describes the scattering of particles that are comparable to the wavelength. Section 2.4 mentioned the limit when the particle size is much less than the wavelength. This limit is better known as Rayleigh scattering. Rayleigh scattering will limit the atmospheric visibility in the case of no aerosol presence but since aerosols will always be present the effect of molecular scattering will be comparatively small at short propagation distances. Rayleigh scattering is what makes the sky blue due to the atmosphere being made up of mostly nitrogen molecules that scatter blue light better than other wavelengths [14]. The last term to define in equation 2.2.1 is scattering due to molecules, σ_{Mscat} , where the scattering is in the regime of $r \ll \lambda$ which will become non-negligible over long path lengths.

The Rayleigh scattering cross-section per molecule for unpolarized incident light can be given as [24]

$$C_{Ray} = \frac{24\pi^3}{\lambda^4 N^2} \left| \frac{m^2 - 1}{m^2 + 2} \right|^2. \quad (2.6.1)$$

The cross-section for a single molecule will not be that easy to calculate due to depolarization. The depolarization is due to molecular anisotropy which can be explained in figure 10. The anisotropy is referring to the orientation of the molecules being non-uniform. To calculate the Rayleigh scattering cross-section of the atmosphere the atmosphere will be modeled in this thesis as nitrogen molecules for simplicity. The phase function of a nitrogen molecule, in figure 10a, can be seen to

have a dip in scattered light at 90° for parallel incident light which affects the unpolarized phase function. In a dense volume of nitrogen molecules orientated in various ways, which is anisotropy, the scattered light will add coherently thus changing the cross-section when viewed from different directions which is accounted for by adding a correction factor for depolarization called δ to equation 2.6.1 [25]

$$C_{Ray} = \frac{24\pi^3}{\lambda^4 N^2} \left| \frac{m^2 - 1}{m^2 + 2} \right|^2 \left(\frac{6 + 3\delta}{6 - 7\delta} \right). \quad (2.6.2)$$

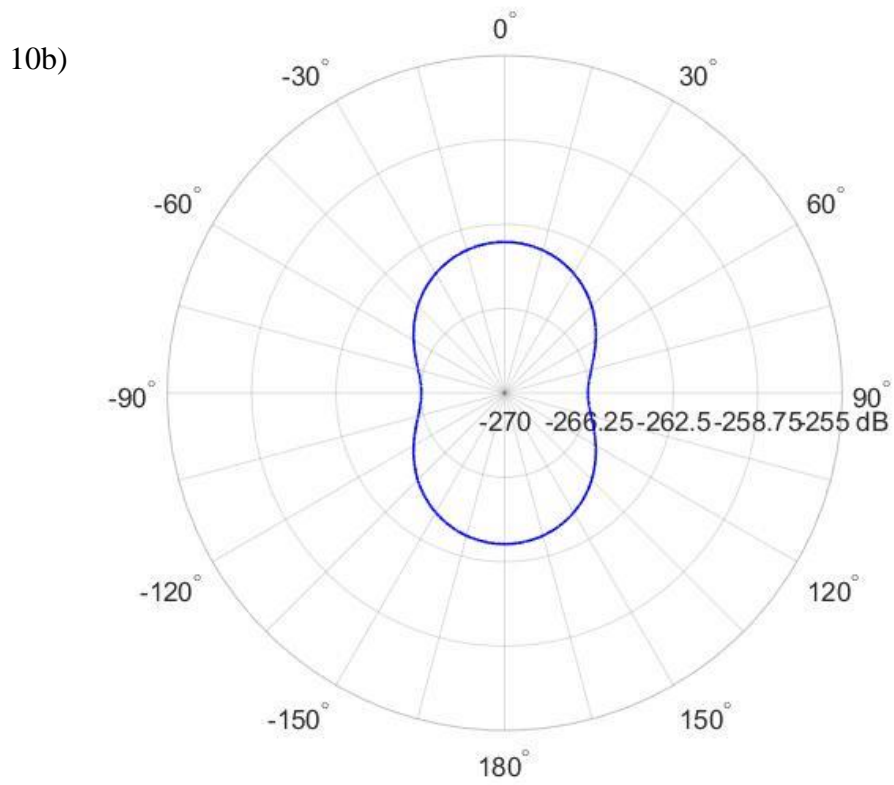
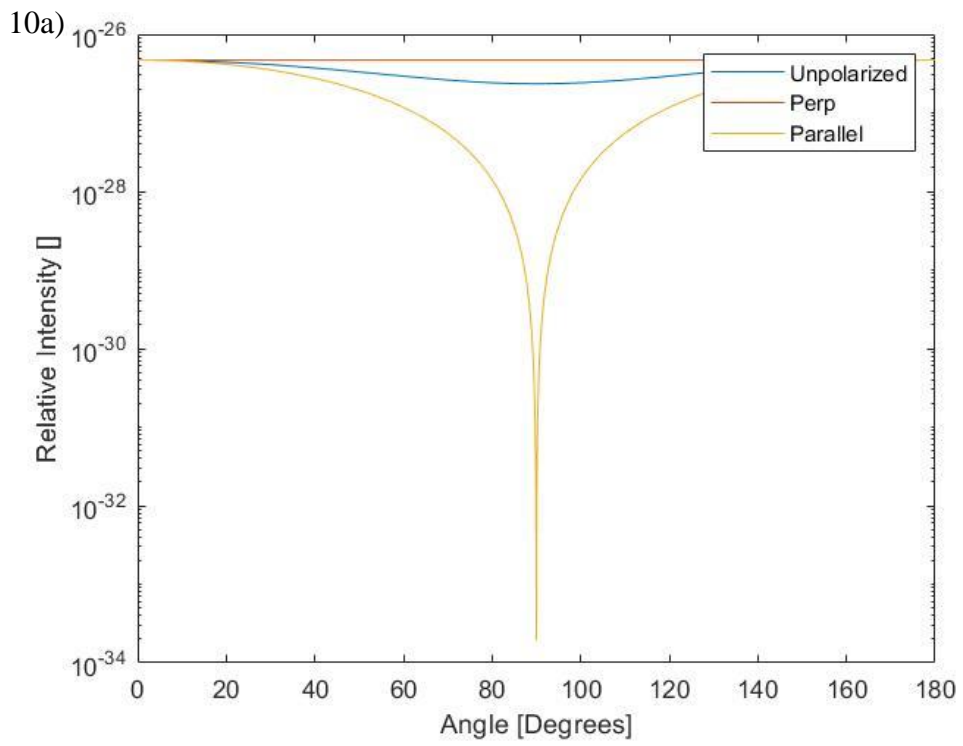


Figure 10: Rayleigh SSPF (10a) and polar distribution plot (10b) for a nitrogen molecule with number density of the atmosphere and index of refraction of a nitrogen molecule as 1.00029944 and the air as 1 at a wavelength of $0.850 \mu\text{m}$

The depolarization factor is also known as the King correction term, $F_k(R_g)$, where R_g is the radius of the gas particle taken into account, in this case R_g is that of nitrogen with a radius of 0.000182 μm . Using the King correction term equation 2.6.2 can be rewritten as

$$C_{Ray} = \frac{24\pi^3}{N^2\lambda^4} (n_1(R_g) - 1)^2 F_k(R_g). \quad (2.6.3)$$

Using the King correction term Bodhaine [25] and Bates [26] have calculated the King correction factor and found various Rayleigh cross-sections that are in agreement for different wavelengths that will be used in this thesis. The Rayleigh scattering coefficient, σ_{Ray} , will be calculated using the density of dry air as, $2.54 \times 10^{25} \text{ particles } m^{-3}$ from a density of 1.225 ($kg \text{ m}^{-3}$). This information will be used later on to find how Rayleigh scattering limits vision through the atmosphere from equation 2.6.4.z

$$\sigma_{Ray} = N C_{Ray} \quad (2.6.4)$$

The Rayleigh approximation for the SSPF of unpolarized light also shows the λ^{-4} law and is given by 2.6.5. In this case R is the distance, r is the particle radius, and I_0 is the incident intensity [14].

$$I_{Ray} = \frac{8\pi^4 r^6}{\lambda^4 R^2} \left| \frac{m^2 - 1}{m^2 + 2} \right|^2 (1 + \cos^2(\theta)) I_0 \quad (2.6.5)$$

This equation can be used to approximate the scattering of particles in the regime $r \ll \lambda$ which would be the case for molecules in the air such as nitrogen, oxygen, and carbon dioxide. Equation 2.6.5 is an approximation of the Mie theory calculation shown in figure 8a for the unpolarized phase function.

2.7 Visibility During Daytime

The full derivation of visibility will be defined in this thesis to clarify the term “visibility” and what implications its consequences have on atmospheric visibility measurements. The simple, and most widely accepted, definition of visibility comes from Koschmieder’s derivation of the visibility equation [16], [27]. For more reading on the subject W.E.K Middleton’s, “*Vision Through the Atmosphere*” [16] goes into great detail.

The diagram of an observer viewing an object, in figure 11, provides a physical definition for the terms used throughout the derivation of visibility. Koschmieder’s derivation starts with defining visibility in terms of contrast, C , which is an object’s luminance, B , against a background luminance, B'

$$C = \frac{(B - B')}{B'}. \quad (2.7.1)$$

When the contrast is negative the object is darker than the background and when the contrast is positive the object is lighter.

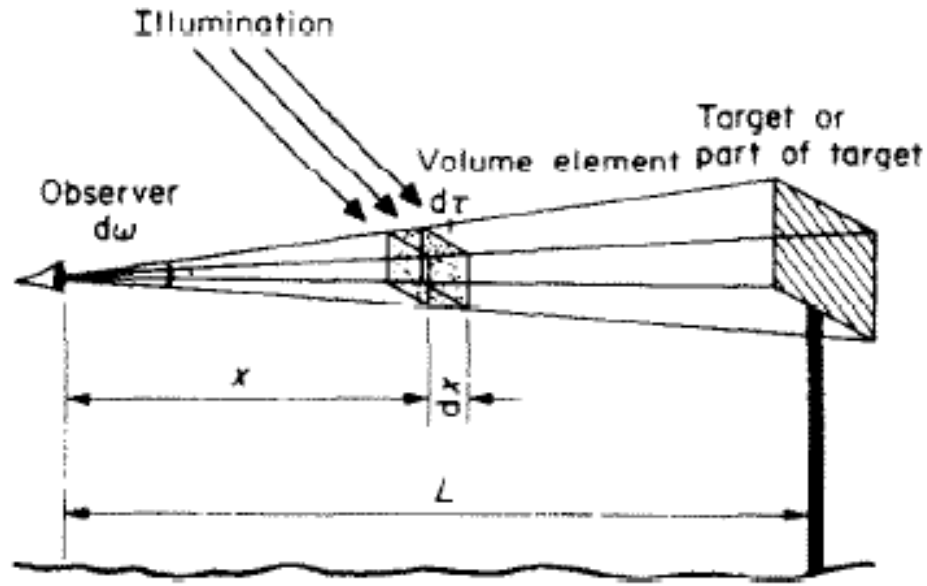


Figure 11: Derivation of the contrast reduction formula. Where all the light from the volume elements $d\tau$ are added together to find the contrast of the target, (Horvath [27]).

The same assumption is used as in section 2.1 where the atmosphere is regarded as homogeneous where the luminance of the target also degrades exponentially similar to the intensity of a light source

$$B(0) = B(L)e^{-\sigma_{ext}L}. \quad (2.7.2)$$

Where $B(L)$ is the luminance of the target at the starting distance, $B(x)^2$ is the luminance seen by the observer, and σ_{ext} is the same extinction coefficient as defined previously. In order for the light to reach the observers eye it must be scattered by the aerosols in the volume between the target and observer which will undergo extinction.

$$dI = \xi\sigma_{ext}d\tau \quad (2.7.3)$$

² The luminance of the target is a function of, x , the distance between the observer and the target. This x is not the Mie size parameter as defined in the previous sections. Only for section 2.7 is this a distance as shown in figure 11.

From figure 11, dI is the light through each volume element $dx d\tau$, ξ is a constant of proportionality defined from boundary conditions, and $d\tau$ is the volume element. The illuminance at the observer due to the scattered light is then given in 2.7.4

$$dE = dI x^{-2} e^{-\sigma_{ext} x}. \quad (2.7.4)$$

To find the illuminance the intensity is scaled by the inverse square loss and atmospheric loss accounted for in equation 2.7.4, where x is the distance of the volume element to the observer. Then by dividing the illuminance by the portion of solid angle the luminance, dB , can be defined

$$dB = \frac{dE}{d\omega} = \xi \sigma_{ext} e^{-\sigma_{ext} x} dx. \quad (2.7.5)$$

By integrating equation 2.7.5, the total amount of light scattered in the light cone from object to observer becomes

$$\begin{aligned} B_0 &= \int_0^L \xi \sigma_{ext} e^{-\sigma_{ext} x} dx \\ &= \xi (1 - e^{-\sigma_{ext} L}). \end{aligned} \quad (2.7.6)$$

The luminance of the target seen by the observer through the atmosphere then becomes a sum of the light scattered and the original luminance through the atmosphere from equation 2.7.2.

$$B_T = \xi (1 - e^{-\sigma_{ext} L}) + B(L) e^{-\sigma_{ext} L} \quad (2.7.7)$$

The boundary condition to find ξ can be taken when L is taken to infinity which physically is the horizon. ξ then becomes the luminance of the horizon B_H . As

previously defined in, equation 2.7.1, equation 2.7.7 can be rewritten in the same form to see how contrast scales in the atmosphere

$$C_{atmos} = e^{-\sigma_{ext}L} \left(\frac{B(L)-B_H}{B_H} \right) = \bar{C} e^{-\sigma_{ext}L}. \quad (2.7.8)$$

To find the visibility of a given object the contrast threshold must be assumed along with the contrast of the object. The contrast threshold, ε , in this derivation is assumed to be that of the human eye $\varepsilon = 0.02$. Whereas the object routinely used for this calculation is an ideally black target against the background so that the contrast, \bar{C} , will be -1. With these known values, equation 2.7.8, can be rearranged to solve for the distance L to be the visibility V

$$V = \frac{-1}{\sigma_{ext}} (\ln|\varepsilon| - \ln|\bar{C}|). \quad (2.7.9)$$

Substitution of the assumed value of contrast threshold and object contrast the Koschmieder formula is obtained in equation 2.7.10

$$V = -\frac{\ln|0.02|}{\sigma_{ext}} \approx \frac{3.91}{\sigma_{ext}}. \quad (2.7.10)$$

The main assumptions in the theory that make this an applicable estimate are that:

- a. The atmosphere is taken to be homogenous.
- b. The scattered light is proportional to the scattering volume.

- c. The target is black to give an object contrast of -1 assuming the horizon is the background.
- d. The contrast threshold is 0.02.

The visibility theory presented by Koschmieder is a good estimate but not going to be exactly the real-time visibility due to fluctuations of the extinction coefficient and boundary condition used to find the background luminance. The visibility during the day time at 550 nm can be seen from table 5 to be roughly 260 km from calculations provided in section 2.6 assuming no molecular absorption and no aerosols present. Wavelengths that are closer to the size of molecule constituents have shorter visibility in a Rayleigh limited atmosphere due to stronger interaction with the molecules which can be seen in table 6.

$\lambda (\mu m)$	$C_{Ray}(m^2) \times 10^{-30}$	$\sigma_{Ray}(m^{-1}) \times 10^{-5}$	$V (km)$
0.450	1.027	2.614	114.6
0.550	0.4513	1.1488	260.8
0.650	0.2288	0.5824	514.4
0.750	0.1282	0.3263	918.1
0.850	0.07739	0.1970	1520.7

Table 6: Calculations at different wavelengths to find the Rayleigh limited visibility from the calculations of the Rayleigh cross-section provided in section 2.6.

2.8 Visibility at Night: Allard’s Law

The Koschmieder equation presented in the previous section is good for daytime applications but not during the night. The nighttime visibility does not account for the illuminance at the observer’s eye from the background light sources such as the sun. In the original theory the proportionality constant, ξ , took into account all the daytime background which is not present at night. The visibility at night is given as

Allard's law which describes the attenuation of light from a point source and no other background light as boundary conditions [16].

$$\varepsilon = Ex^{-2}e^{-\sigma_{ext}x} \quad (2.8.1)$$

Allard's law is written in terms of the illuminance of the point source, E , to find the visibility. If we take the contrast to be 0.02, as before in section 2.7, the visibility can be solved for using an iterative computational root finding technique.

$$V + \frac{1}{\sigma_{ext}} \ln \left| \frac{V^2 \varepsilon}{E} \right| = 0 \quad (2.8.2)$$

In the case of Allard's law, the source intensity must be known. When using a measurement system, the light source illuminance, E , should be known allowing for computation of the visibility when σ_{ext} is known since ε is taken to be a fixed value.

2.9 Visibility in Fog: Wavelength Dependence

In thick fogs the visibility is changed due to the extinction coefficient being strongly dependent on wavelength. By assuming the function form of equation 2.9.1 for the extinction coefficient and substituting Koschmieder's formula to equation 2.9.1 the wavelength dependence can be obtained as 2.9.2 [28].

$$\sigma_{ext} = A\lambda^{-q} \quad (2.9.1)$$

$$V = -\frac{\ln(0.02)}{\sigma_{ext}} \left(\frac{\lambda}{550} \right)^q \quad (2.9.2)$$

The exponent q has been determined by experimental data by Middleton and Lohle [16] but then later refined by Kim [29] who modified the original theory to fit the transition between visibilities better with equation 2.9.4 where V is given in kilometers in both.

$$q = \begin{cases} 1.6 & V > 50 \\ 1.3 & 6 < V < 50 \\ 0.0585V^{\frac{1}{3}} & V < 6 \end{cases} \quad (2.9.3)$$

$$q = \begin{cases} 1.6 & V > 50 \\ 1.3 & 6 < V < 50 \\ 0.16V + 0.34 & 1 < V < 6 \\ V - 0.5 & 0.5 < V < 1 \\ 0 & V < 0.5 \end{cases} \quad (2.9.4)$$

Middleton [16] explains the phenomena based off of experimental observations between blue, green, and red light where, in thick fog, the extinction changes drastically. This raises the question if using Koschmieder's formula, equation 2.7.10, still holds as a decent approximation since it is meant for 550nm. According to Nebuloni's theoretical computations, it has been noted that wavelengths into the mid-infra-red (NIR) can safely be adopted [28]. Along with this finding commercial visibility meters produced by Vaisala, CS, and RMYC in section 1.2 adopted equation 2.7.10 to find visibility during the day while using near-IR light sources.

This section of the theory is presented to show that this wavelength dependence of the extinction coefficient has been taken into account of the final project design. This phenomenon will be discussed later in future considerations for the FSM to measure the visibility by finding which value of q to adopt in real-time weather conditions.

2.10 Meteorological Optical Range

The meteorological optical range (MOR) is a standard set by WMO to define the contrast threshold used for making visibility measurements. The definition of visibility still taken to be used with the assumption of a black target against the horizon. But instead of taking a contrast threshold of 0.02, the MOR is taken to have a contrast threshold of 0.05 which changes equation 2.7.10 to equation 2.10.1 along with night and fog visibility (see table 7) [18].

Environment	Visibility Equation	
Daytime	$V = -\frac{\ln 0.05 }{\sigma_{ext}} \approx \frac{2.998}{\sigma_{ext}}$	(2.10.1)
Nighttime	$V + \frac{1}{\sigma_{ext}} \ln \left \frac{V^2(0.05)}{I} \right = 0$	(2.10.2)
Heavy Fog	$V = -\frac{\ln(0.05)}{\sigma_{ext}} \left(\frac{\lambda}{550} \right)^q$	(2.11.3)

Table 7: Equation for calculating visibility in various weather conditions.

MOR is defined relative to 550 nm light due to the fact that the human eye is most efficient at detecting light at this wavelength as shown in figure 10. The eye detects light at night most efficiency at ~500 nm as shown by the dotted peak in figure 12. The different kinds of vision are introduced in the introduction of chapter 2.

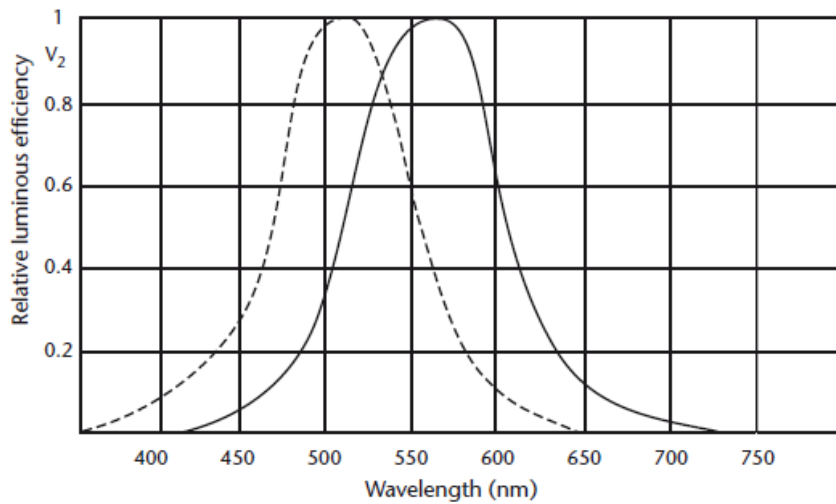


Figure 12: Relative luminous efficiency of the human eye of specific wavelengths. The dotted line is nighttime vision whereas the solid line is day time vision (WMO [18]).

Since MOR is defined at these wavelengths, it poses a problem of the definition of visibility in poor weather conditions such as fog which is discussed in section 2.9. The correction factor for visibility is given in equation 2.9.2 for wavelengths other than 550nm.

2.11 Atmospheric Aerosols

In the atmosphere there are various kinds of airborne particles, known as aerosols, that scatter and absorb light including water, pollutants, dust and so on. When in high concentrations, any form of aerosol can severely limit the visibility. In the case of weather conditions such as fog, mist, or haze the dominant aerosols are made up of water particles. It is assumed that water has a real index of refraction of 1.329 and a complex index of refraction of 2.93×10^{-7} at 25°C [30] for a source of 0.850 μm . The complex refractive index is much less than the real part in water, meaning that the dominant attenuation property of water is scattering. This thesis will not take into account the temperature dependence of the refractive index.

The formation of clouds/fog is due to warm air rising in the atmosphere since its density is smaller than cold air. When the temperature difference between the cold and warm air reaches the dew point the water condenses forming fog. These temperature inversions can be created by a few noted mechanisms such as advection (wind), radiation, precipitation, and valleys [31], [32].

2.11.1 Clouds and Aerosols

There are ten different kinds of clouds where the clouds of most interest lie low to the ground forming foggy weather conditions affecting visibility. Low level clouds include stratus and cumulus clouds. Stratus clouds develop horizontally and make up fog when on or near the ground, whereas cumulus clouds develop vertically. The density of the cloud can vary affecting if the particles present will be more of a fog, mist, or haze. Various weather conditions and fog density can change the visibility through the atmosphere that can be seen in table 8 below. There is a correlation between the density of the fog and particle size that will be mentioned in the next section.

Weather Condition	Visibility Range (km)	Loss (dB/km) at 785nm
Thick Fog	0.2	89.6
Moderate Fog	0.5	34
Light Fog	0.770 to 1	20 to 14
Thin Fog/Heavy Rain	1.9 to 2	7.1 to 6.7
Haze/Medium Rain	2.8 to 4	4.6 to 3
Light Haze/Light Rain	5.9 to 10	1.8 to 1.1
Clear/Drizzle	18 to 20	0.6 to 0.53
Very Clear	23 to 59	0.46 to 0.21

Table 8: Visibility and loss conditions for various weather conditions (Kaushal [19]).

2.11.2 Choice of Aerosol Distributions for Atmospheric Models

To choose the particle distributions that make up fog, mist, and haze, particle counting data is reviewed to determine the mean particle size and shape of the

distribution. Previously Deirmendjian [21] chose six models that represent haze and fog distributions with three shown in figure 13.

The haze distributions devised are based on the modified gamma distribution, equation 2.10.1, with a mean radius of $0.1 \mu\text{m}$ and varying radii between $0.01 \mu\text{m}$ and $5 \mu\text{m}$. Whereas the fog distributions are centered around $2\text{-}5 \mu\text{m}$ and vary from $0.1 \mu\text{m}$ to $14 \mu\text{m}$ to include cumulus clouds with higher water content. In both cases the value of the shape parameter, α , is between 1 and 6 and the number density for each of the distributions is normalized to 100 cm^{-3} . Kaushal [19] presents fog/haze distributions to center around $0.1 \mu\text{m}$ and cloud distributions to center around $10 \mu\text{m}$ which are in the same region as Deirmendjian [21]. Durbin [33] collected particle data by flying through low-mid level cumulus clouds where the mean particle radius varied between $3.35 \mu\text{m}$ to $11.7 \mu\text{m}$. The average diameter changed depending on the thickness of the cloud and water content where 230-760 meter thick clouds have a mean radius of $4 \mu\text{m}$ and 1220-2130 meter thick clouds have a mean radius of $9 \mu\text{m}$. Durbin [33] did an analysis of 150 experimental trials of cloud particle characterization and obtained a droplet distribution that goes exponentially with the droplet diameter similar to that as presented by Derimendjian [23].

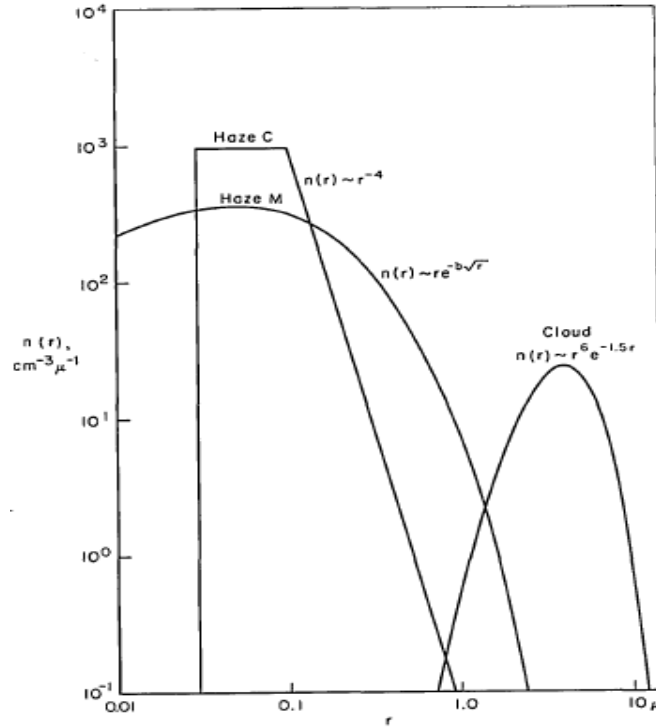


Figure 13: Plot of Deirmendjian's three main models of haze and clouds/fog from [23].

Miles [34] reviewed many different particle counting experiments in the atmosphere stressing particles in stratus clouds. For stratus clouds the mean diameters varied from a radius of 1-9 μm . Their summary produced a mean radius of stratus clouds to be 4.1 μm and an effective mean radius of 5.4 μm which accounts for aspherical particles. Through their study the modified gamma function, in similar form to equation 2.10.1, is used to represent particle distributions where the shape parameter, α , took on values between 1 and 4. The mean number density found in continental stratus clouds is 288 cm^{-3} whereas maritime stratus clouds took on a number density of 74 cm^{-3} .

Winstanley [35] used a similar distribution to [21], [33], and [34] for modeling the distributions, same as equation 2.10.1, accounted for in their visibility meter design. The model radii were between size factors of 0.2 to 90 in increments of 0.2, whereas in terms of radius it varied from 0.0271 μm to 12.17 μm in steps of 0.0271

μm , with a mean model radius, r_c , of $0.2 \mu\text{m}$ to $1.6 \mu\text{m}$ in increments of $0.2 \mu\text{m}$. The mean radius does not have anything to do with a variance of the distribution but only a maximum value of the gamma distribution.

$$n(r) = ar^\alpha e^{-br} \quad (2.10.1)$$

All the distributions used by [35] were normalized to a density of 100 cm^{-3} which changes the parameter, a , that can be found from the normalization condition of all radii.

$$N = \int_0^{\infty} n(r)dr = ab^{-(\alpha+1)}\Gamma(\alpha + 1) \quad (2.10.2)$$

Where, $\Gamma(\rho)$, is the standard gamma function. The second parameter, b , can be related to the mean by finding the maximum of the distribution.

$$\frac{d}{dr}n(r) = ar^{\alpha-1}e^{-br}(\alpha - br_c) = 0 \quad (2.10.3)$$

$$b = \frac{\alpha}{r_c} \quad (2.10.4)$$

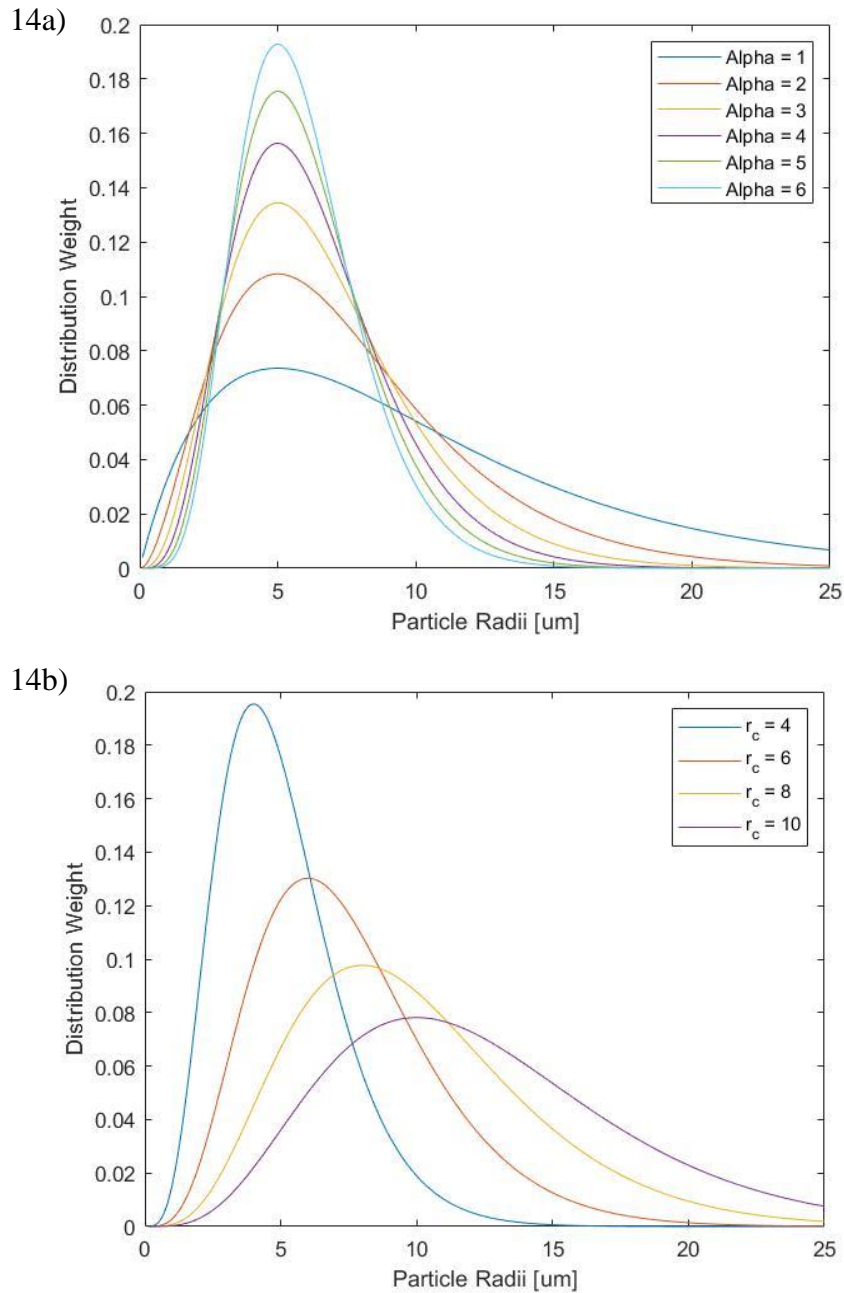


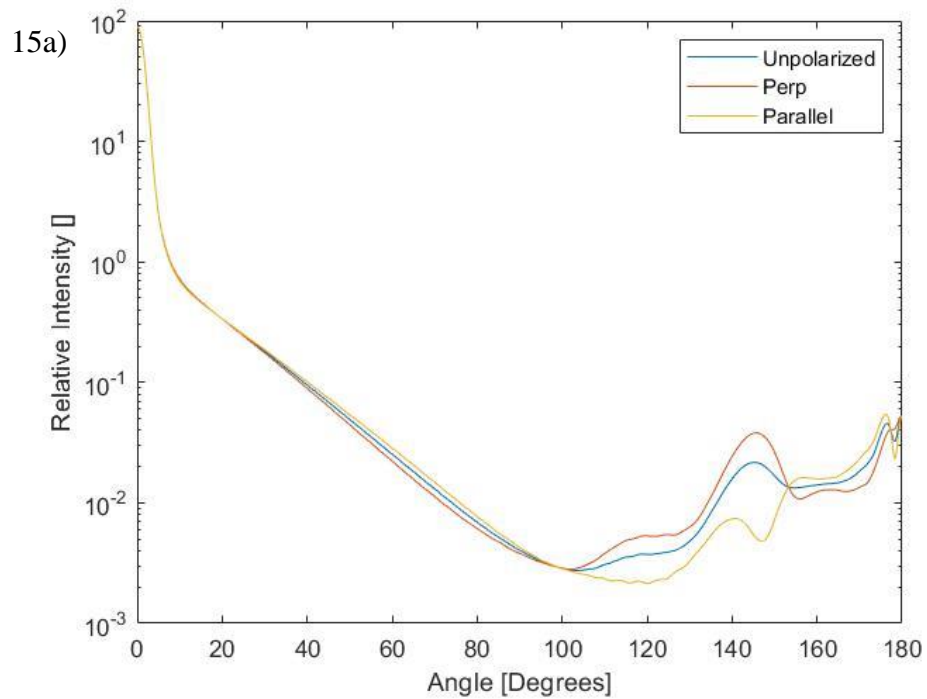
Figure 14: Modified gamma distributions with varying r_c (14a) with a fixed shape parameter of $\alpha = 4$, varying the mean radius stretches and shrinks the distributions. Whereas varying the shape parameter increases the weight of the mean particle or decreases the weight (14b). In both cases the max radius of $25\mu\text{m}$ is modeled to see the full effect of the change in distribution shape.

By comparing these distributions presented in [19], [21], and [35] to particle counter data in [33] and [34] the models for this thesis were developed. To model the aerosols the modified gamma distribution in equation 2.10.1 is adopted along with the

r_c as the maximum value and normalization conditions. The number density adopted is fixed at 100 cm^{-3} since it can be extended to weather with less dense mist or haze, not including fog or cloud cover. The shape parameter, α , is chosen to be varied between 1 and 4 to include multiple shapes of the gamma distribution around the mean radius. The entire particle radii to be modeled falls in between $0.1 \mu\text{m} - 17 \mu\text{m}$ with a step size of $0.1 \mu\text{m}$. This will include the smaller particles that make up haze and most fog conditions. The model particle size will not account for large radii aerosol particles that can make up fog with high levels of water concentration at higher elevations which can exceed radii of $25 \mu\text{m}$ [33]. Lastly, the mean radii, r_c , modeled are between $0.2 \mu\text{m} - 9 \mu\text{m}$ which is determined to contain most stratus fog, cumulus fog, haze, and mist that are studied in the particle counting data. Distributions containing these characteristics are shown in figure 14. Computations using these distributions parameters will be discussed in the next chapter.

2.11.3 Aerosol Phase Function Characteristics

Previously mentioned in section 2.5.6 the SSPF of a polydisperse system can be found using the particle distribution as a weight average. The modified gamma distribution phase function for different particle distributions are shown in figures 15 - 17. In figure 15a, using a replicated model to that of Deirmendjian's cloud C in figure 13, the forward scattering can be seen prominently.



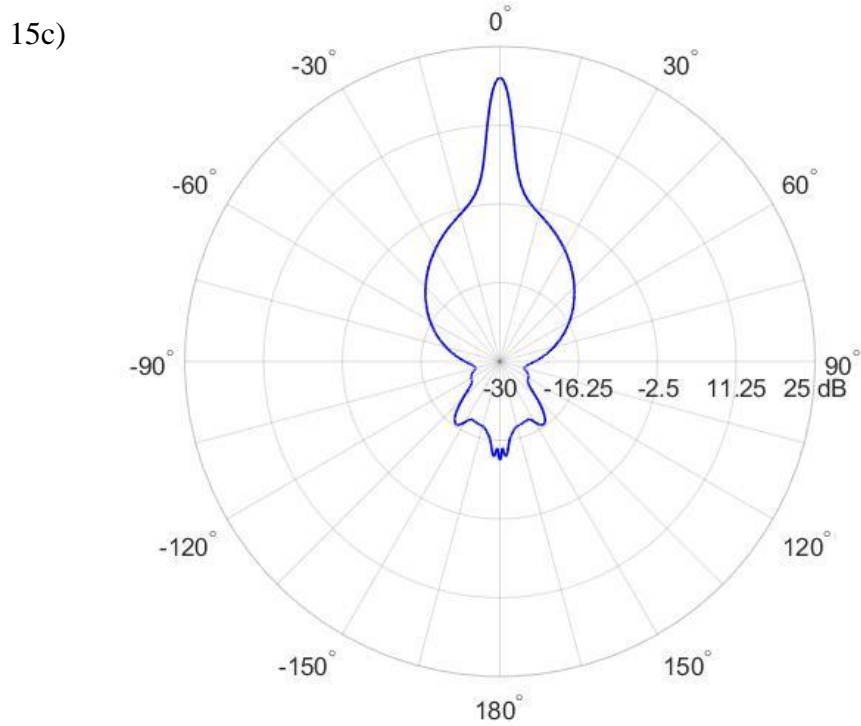
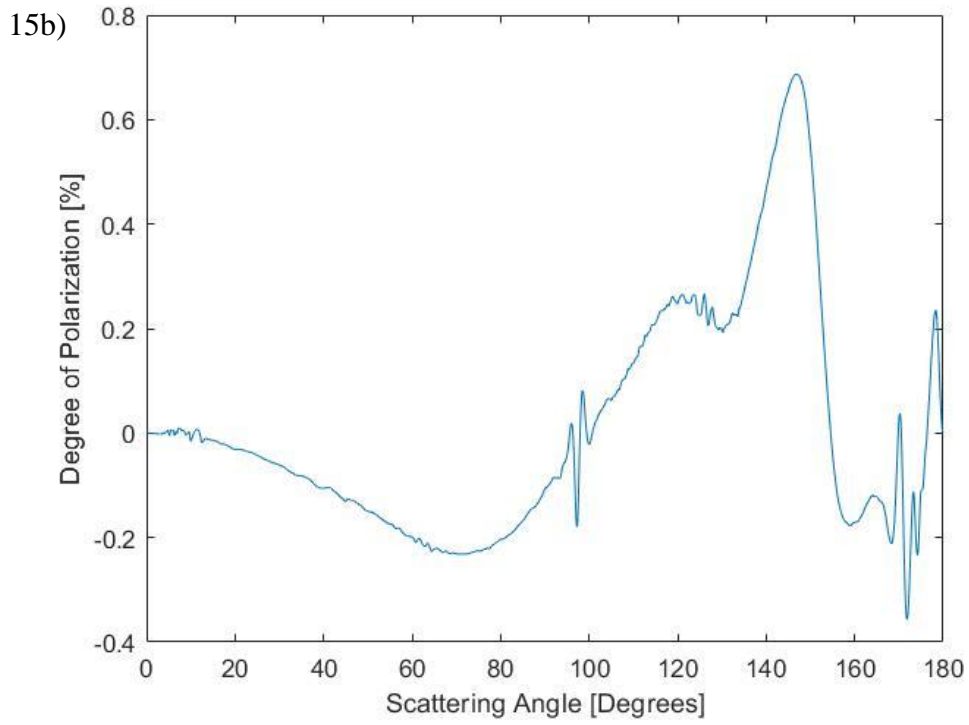
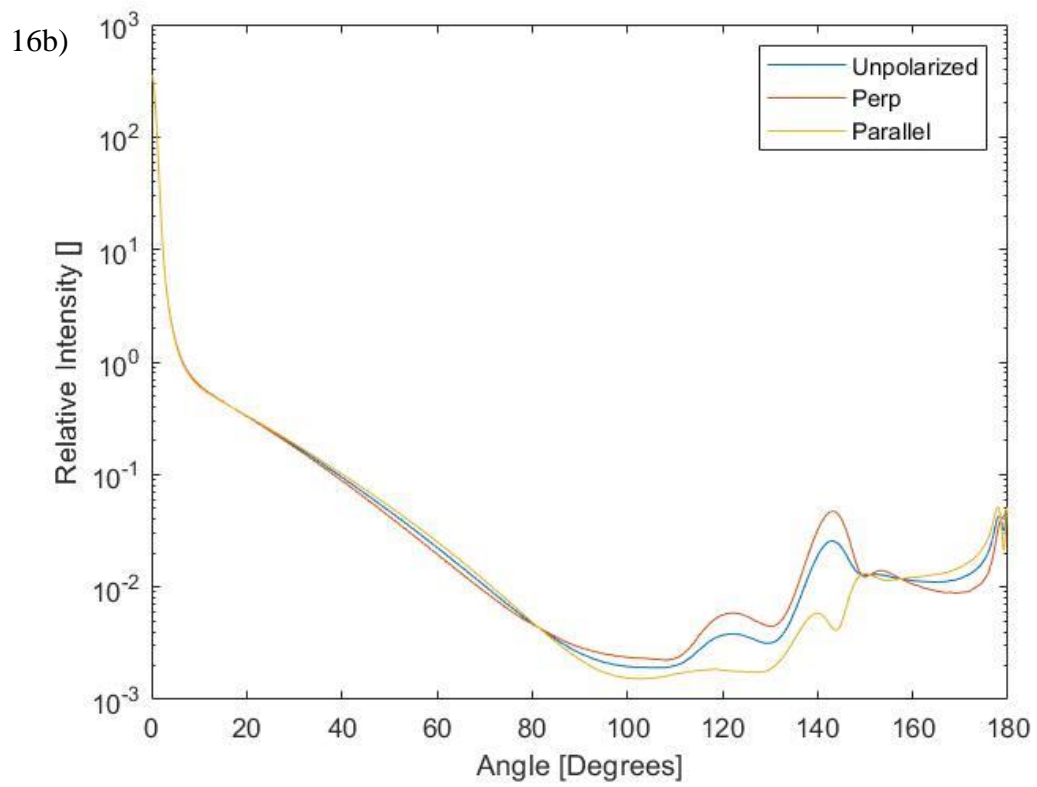
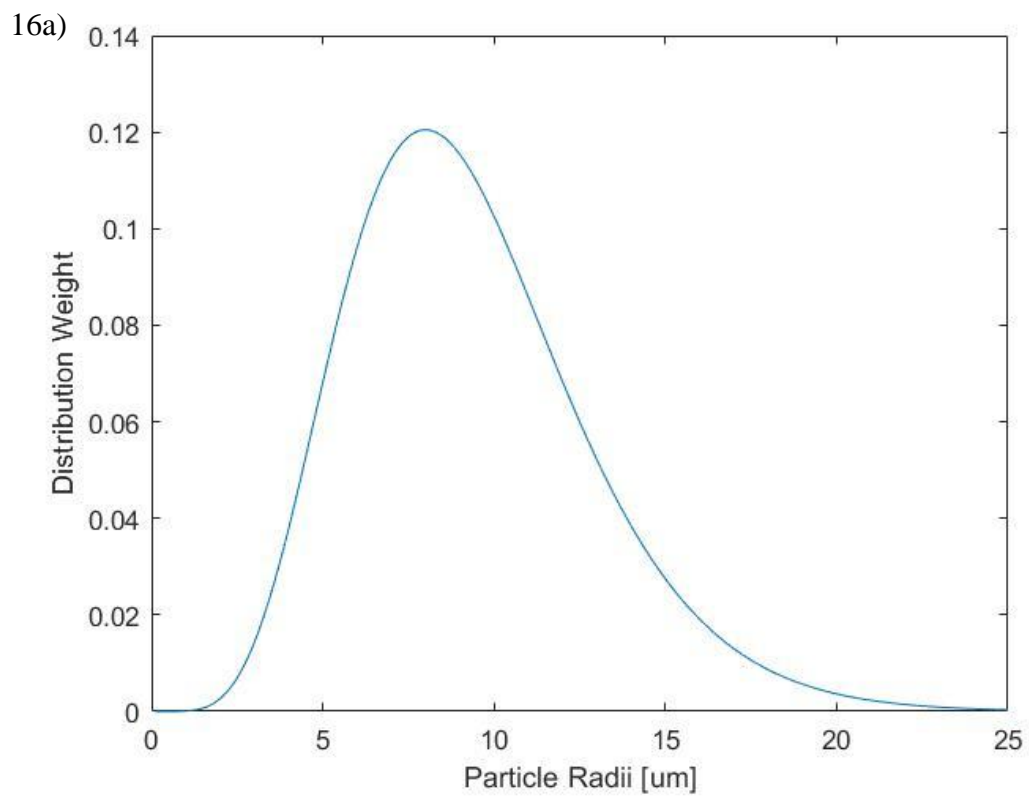


Figure 15: Phase function (15a) calculated from a replicated distribution to cloud C in figure 13 with strong forward scattering (15b). Backscattered light is seen to be polarized stronger in the perpendicular direction than parallel for this fog distribution (15c).

The cloud C model is meant to encompass thick low lying stratus clouds used as a good approximation for thick fog in Deirmendjian's work where he studied aerosol scattering for various atmospheric conditions [21] [23]. The peak of the scattering is roughly 20 dB greater than the, rather flat, side scattering. The cloud C model also has noticeable backscatter. When driving in thick fog the increased backscatter is noticeable when high beam headlights are turned on. In figure 15b it is also noticeable that much of the light backscattered is perpendicularly polarized to the scattering plane. The fog modeled in the cloud C model has a calculated extinction of 16.99 km^{-1} making this dense fog. In figure 16 the plots are of thick fog with larger particle size where the SSPF, figure 14a, can be seen to have a half order of magnitude increase. The fog in figure 14a is modeled with a gamma distribution with $\alpha = 6$, $N = 100 \text{ cm}^{-3}$, particle index $n_1 = 1.34$, and incident wavelength of $0.850 \mu\text{m}$. The particle radii are between $0.1 \mu\text{m}$ and $25 \mu\text{m}$ in steps of $0.2 \mu\text{m}$ and a mean radius, r_c , of $8 \mu\text{m}$. The fog distribution has a calculated extinction coefficient of 65.62 km^{-1} for an incident wavelength of $0.850 \mu\text{m}$.



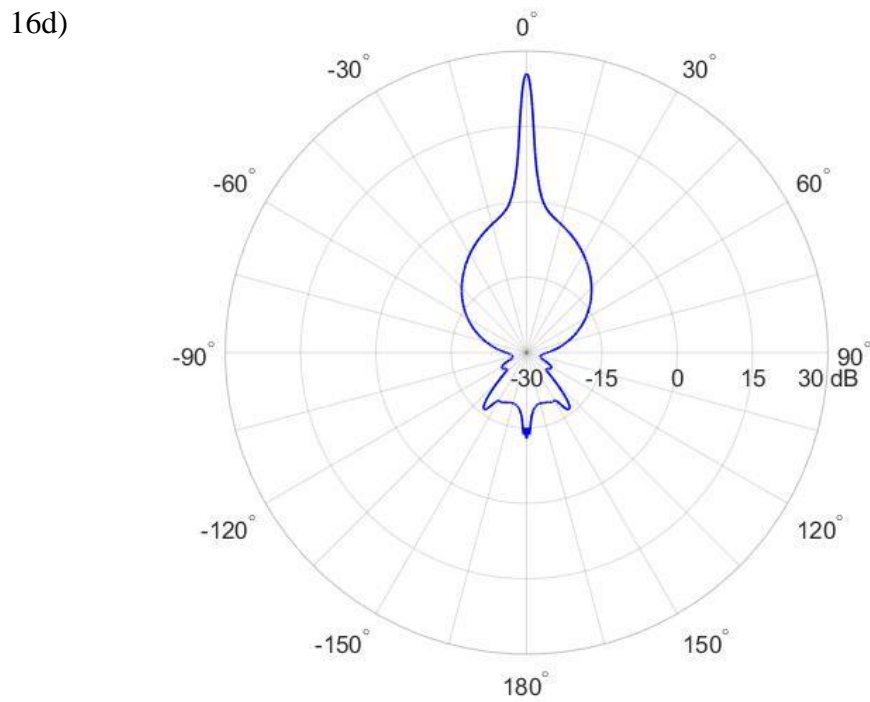
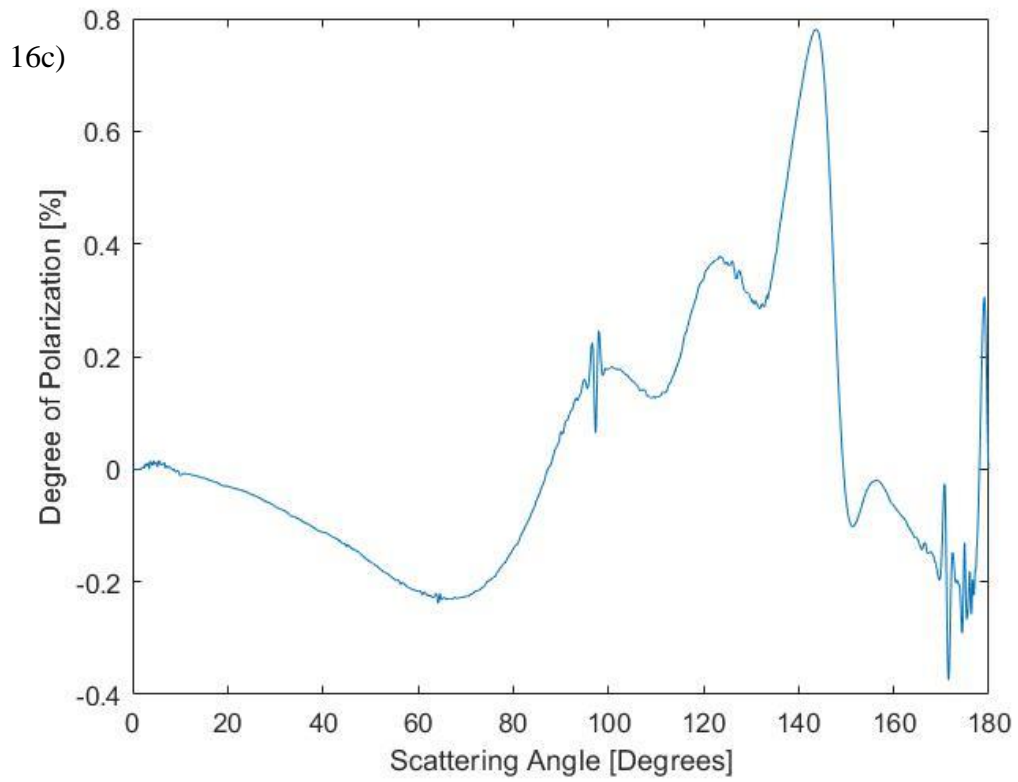


Figure 16: Similar model to that of Deirmendjian's Cloud C. 16a is the distribution used to produce the phase function (16b), degree of polarization (16c), polar plot (16d) for the respective distribution

The haze model M of Deirmendjian has also been modeled but not to the exact function as shown in figure 13. The discussion of comparing this model to Deirmendjian's is mentioned in section 3.2. In figure 17 the SSPF and polar distribution of the scattered light is shown for a replicated haze M distribution. The particles in haze conditions are smaller than fog and lie between $0.01 \mu\text{m}$ and $2\mu\text{m}$. Since the particles are now on the same order of magnitude as visible light the scattering will not be as well defined in the forward direction as seen in the discussion of figure 7. In comparison to figure 7, the smaller particles have distinct diffraction peaks whereas for the haze distribution the peaks have been smoothed out by constructive and destructive interference. The same effect is seen in the fog distributions in figures 15 and 16 along with the Gaussian distribution in section 2.5.6. The aerosol distributions presented in this section will be used later on in chapter 4.

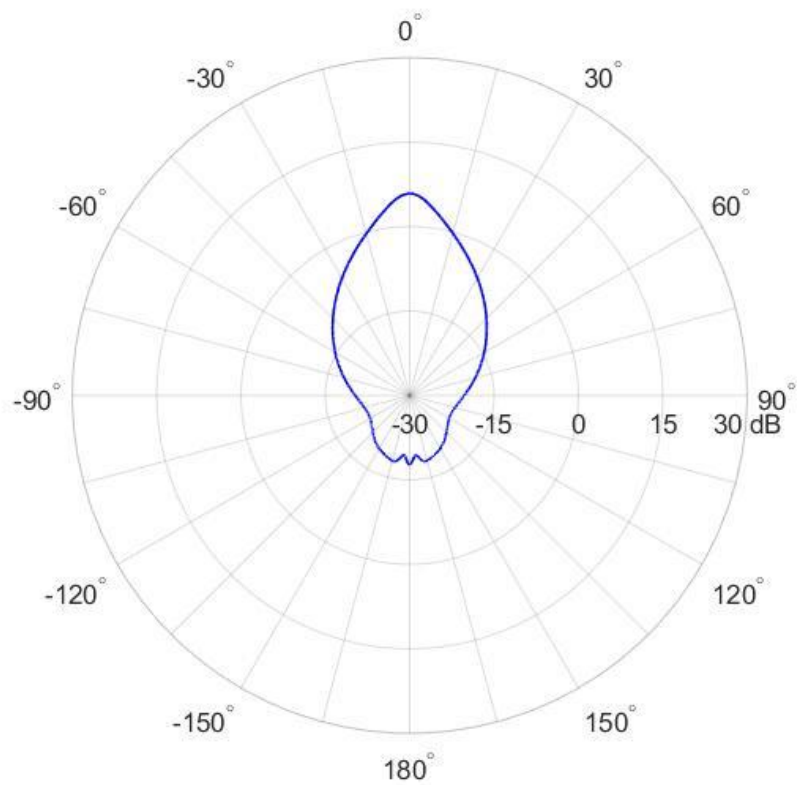
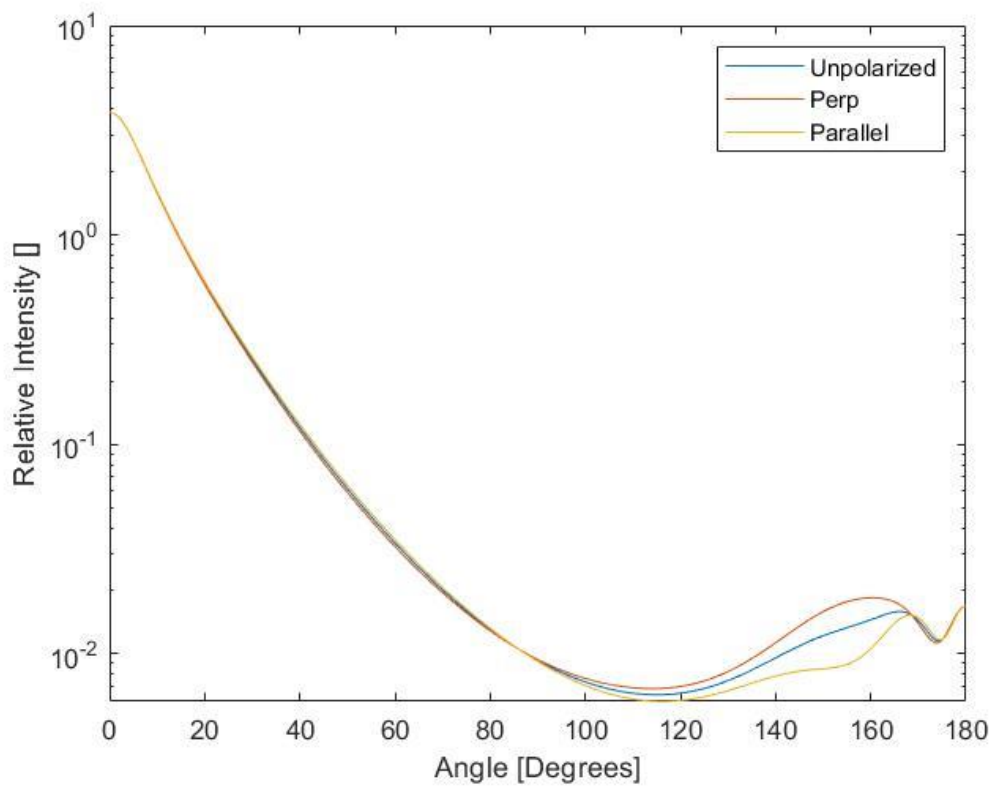


Figure 17: (17a) The SSPF for haze distributions can be seen to lack the well-defined forward scattering peak and have a more uniform scattering distribution (17b).

Chapter 2 Summary

To summarize the most important equations to describe how light interacts with particles table 9 shows which equations are most pertinent to this paper. The first two equations 2.5.4 and 2.5.5 will be used in all computational Mie calculations in the next section. Equation 2.5.59 will be used throughout the rest of this paper to describe the amount of scattered light per unit volume per unit incident intensity for polydisperse systems. Equation 2.10.1 will be used in the forward scatter meter design to calculate the daytime visibility range.

Section	Describes	Equation
2.5	S_1 parameter relating to parallel incident light	2.5.4
2.5	S_2 parameter relating to perpendicular incident light	2.5.5
2.5.4	Single particle scattering phase function for unpolarized light	2.5.47
2.5.1	Polydispersion scattering phase function for unpolarized light	2.5.59
2.10	Visibility range during the day with a 5% contrast threshold	2.10.1

Table 9: Summary of important information used in chapter 4 from chapter 2.

Chapter 3: Computation

To make the theory from chapter two practical computational techniques must be used to calculate Mie theory parameters. The Mie coefficients and matrix elements presented in chapter 2.5 are difficult to calculate and visualize without computation. Many authors have used plots obtained by Mie scattering code which include Bohren [14], Van de Hulst [15], Deirmendjian [21] [23], and Dave [36]. The most concise discussion of Mie scattering code can be found in Dave [36]. All plots obtained in previous chapters were produced using the coding procedure derived in this chapter. The code will be provided in the appendix.

To start the computation the coefficients defined in equations 2.5.15 and 2.5.16 are found by rewriting them in terms of the logarithmic derivative of $\psi_n(mx)$ called $D_n(mx)$ defined in equation 3.1.1.

$$\frac{d[\ln(\psi_n(mx))]}{d(mx)} = \frac{\psi'_n(mx)}{\psi_n(mx)}$$

$$D_n(mx) = -\frac{n}{mx} + \frac{j_{n-1}(mx)}{j_n(mx)} = -\frac{n}{mx} + \frac{1}{\frac{n}{mx} - D_{n-1}(mx)} \quad (3.1.1)$$

$$D_0(mx) = \frac{j_{-1}(mx)}{j_0(mx)} = \cot(mx)$$

Where the Mie scattering coefficients can be rewritten and calculated from equations 3.1.2 and 3.1.3.

$$a_n = \frac{\left\{ \frac{D_n(mx)}{m} + \frac{n}{x} \right\} Re(\zeta_n(x)) - Re(\zeta_{n-1}(x))}{\left\{ \frac{D_n(mx)}{m} + \frac{n}{x} \right\} \zeta_n(x) - \zeta_{n-1}(x)} \quad (3.1.2)$$

$$b_n = \frac{\left\{ mD_n(mx) + \frac{n}{x} \right\} Re(\zeta_n(x)) - Re(\zeta_{n-1}(x))}{\left\{ mD_n(mx) + \frac{n}{x} \right\} \zeta_n(x) - \zeta_{n-1}(x)} \quad (3.1.3)$$

ζ , can be found by the recursion relations:

$$\zeta_n(x) = \frac{2n-1}{x} \zeta_{n-1}(x) - \zeta_{n-2}(x) \quad (3.1.4)$$

$$\zeta_{-1}(x) = \cos(x) - i\sin(x)$$

$$\zeta_0(x) = \sin(x) + i\cos(x)$$

Now that the Mie coefficients are redefined in a more computation friendly approach the function $D_n(mx)$ must be looked at closely as discussed by Dave [36].

To look at the computation instability, $D_0(mx)$ is expanded in terms of hyperbolic functions.

$$D_0(mx) = \frac{\sin(n_0x) \cos(n_0x) + i \sinh(n_1x) \cosh(n_1x)}{\sin^2(n_0x) + \sinh^2(n_1x)} \quad (3.1.5)$$

When $D_0(mx)$ is rewritten in this form it is seen that there will be a division by zero if $n_1x = 0$ and if n_0x is an integer multiple of π . Another issue with this form of the recursion happens when the product of, n_2x , comes close to $\pi/2$ since the function starts to increase drastically [36]. To bypass these instabilities the downward recursive form of equation 3.1.1 will be used

$$D_{n-1}(mx) = \frac{n}{mx} - \frac{1}{D_n(mx) + \frac{n}{mx}}. \quad (3.1.6)$$

First, the function $D_n(mx)$ will be tested using a check proposed by Dave [36]. The relative refraction index is set to, $m = 1.342 - 1.0i$, and the size parameter to, $x = 50\pi$. The forward recurrence and backward recurrence are shown in figure 18.

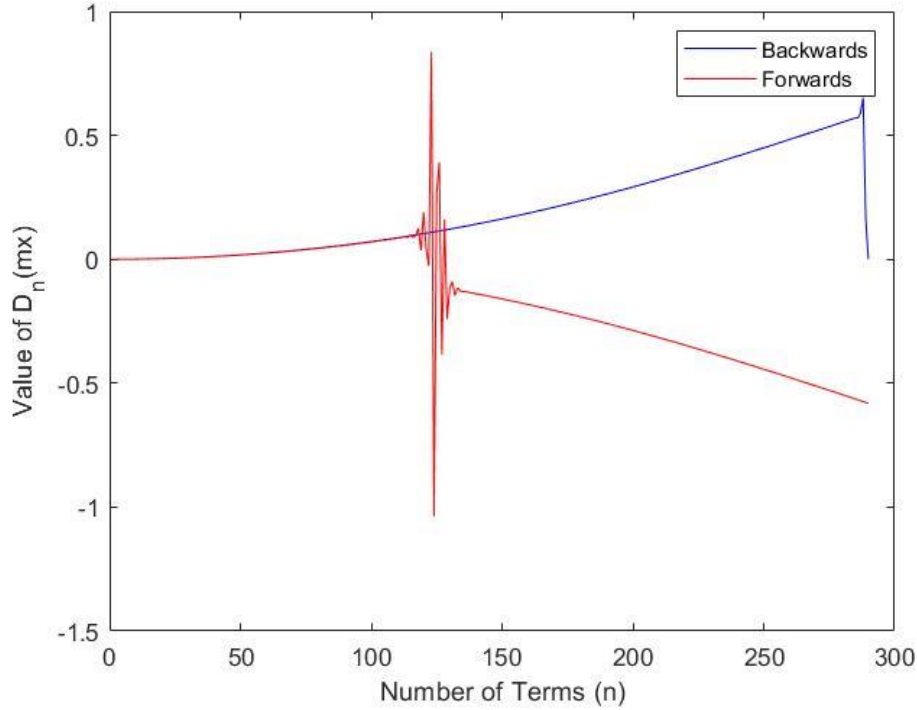


Figure 18: Values of the backward vs. forwards recursion for 290 terms.

The instability of the forward recursion can be seen when the number of terms reaches 120 as seen in figure 18. The trick is to pick enough terms to calculate the backward recursion correctly depending on the size of the particle. As the backward recursion and series terms must reach enough terms. To reach enough terms the backward recursion is calculated out to N_d terms where $N_d = 2N_c$. This gives the series in equations 2.5.4 and 2.5.5 enough terms to converge correctly. By choosing these number of terms the backward recursion of $D_n(mx)$ also has enough terms to converge correctly.

3.1 Single Particle Code

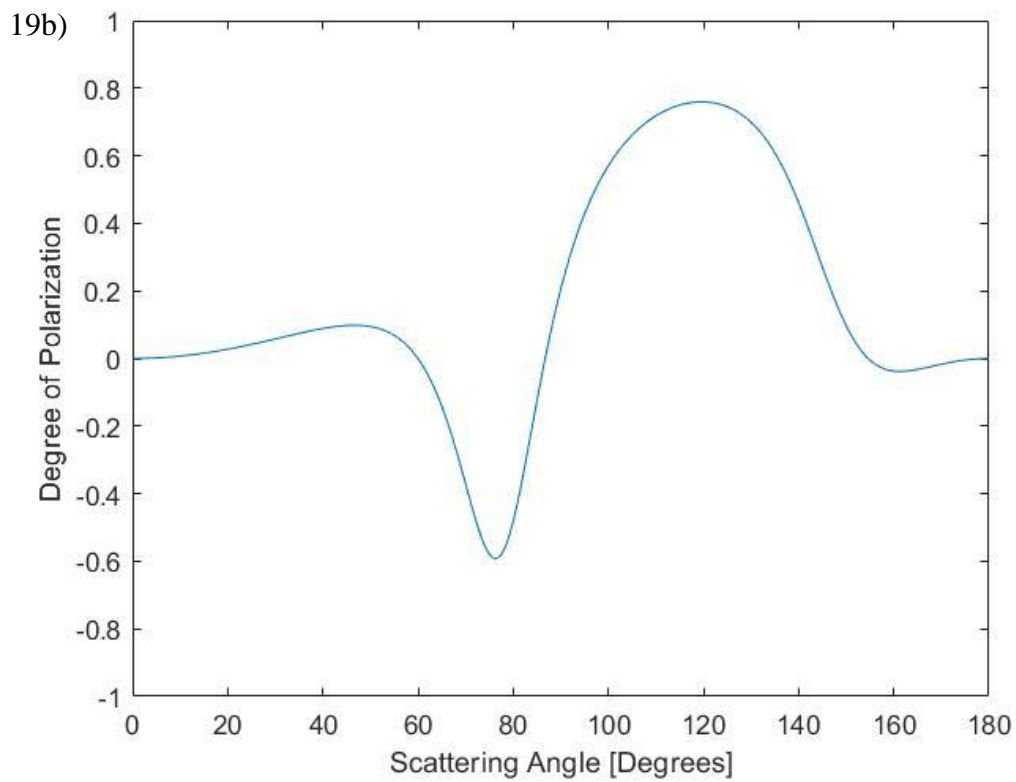
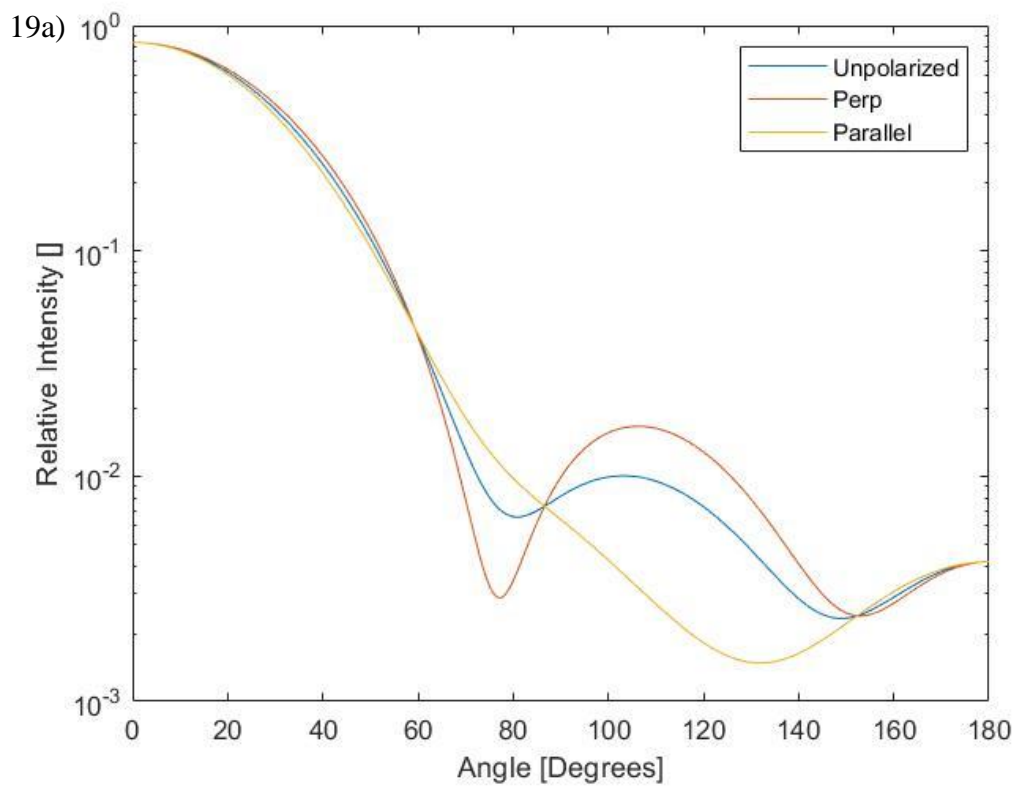
The two series in equations 2.5.4 and 2.5.5 can now be found with the equations for the Mie coefficients and the angular dependence functions $\pi(\theta)$ and $\tau(\theta)$. To test the code for a single particle calculation the code is tested against published figures in

[14]. For the case of a water droplet in air with a refractive index of $1.33 - 10^{-8}i$, size parameter of 3, and wavelength of $0.550 \mu\text{m}$ the first 5 Mie scattering coefficients are compared with their relative percent error.

Term (n)	Percent Error (%)			
	$\Re\{a_n\}$	$\Im\{a_n\}$	$\Re\{b_n\}$	$\Im\{b_n\}$
1	0.000812	0.000805	0.000254	1.17E-05
2	0.000151	0.000652	0.000646	0.000198
3	0.000453	0.000197	0.000247	0.000164
4	0.001588	0.000886	0.000776	6.13E-05
5	0.000535	0.000799	0.000308	0.000322

Table 10: Comparing real and imaginary components of the Mie coefficients of this papers Mie computation to Bohren [14]. Using: $n_0 = 1$, $n_1 = 1.33 - 10^{-8}i$, $x = 3$, $\lambda = 0.550 \mu\text{m}$

In table 10 it can be seen that the Mie coefficients are in agreement with the published numbers making this thesis' single particle code promising to use for more analysis of Mie theory. Using the above-mentioned particle parameters, the phase functions plots were also calculated where they were normalized in accordance with the matrix elements given in equation 2.5.42. The phase functions for perpendicular, parallel, and unpolarized input polarized light are shown in figure 19b and 19c. When compared to Bohren's [14] in figure 19a all noticeable features are included with the right order of magnitude drop off. The difference in maximum value is due to normalization differences of 4π in the SSPF adopted by this thesis since Bohren [14] does not adopt this normalization factor.



19c)

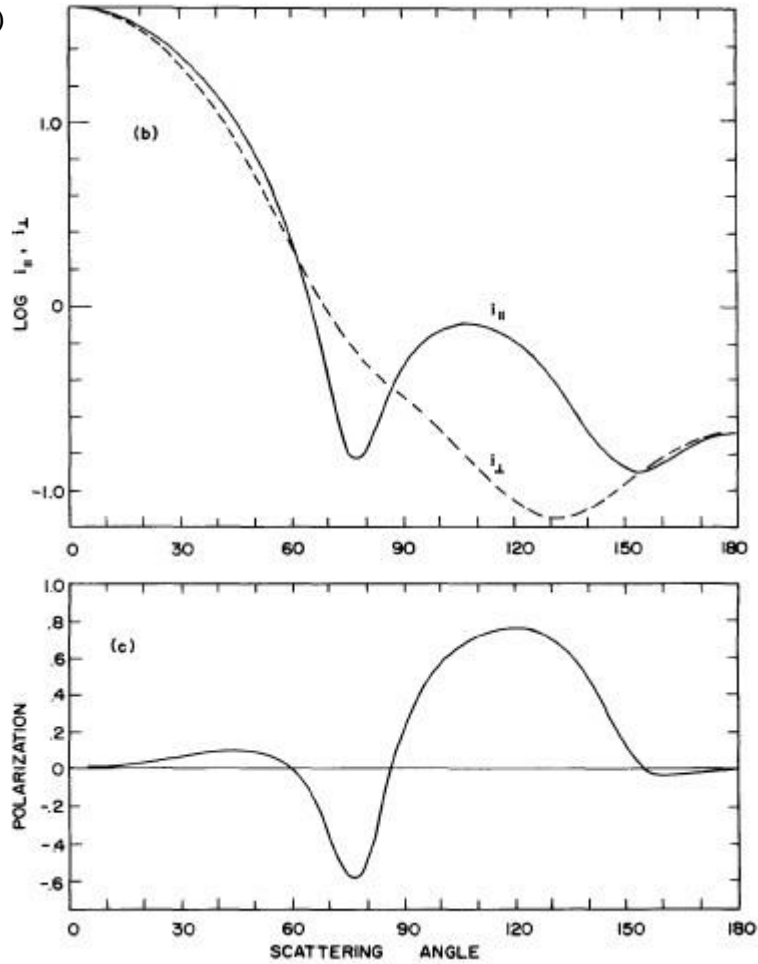


Figure 19: The original calculations of Bohren [14] in (19a and 19c). The plots computed by the procedure outlined above are figures 19b and 19c.

Presented in Bohren [14] is a logarithmic polar plot, figure 20a, to visualize the physically scattering pattern around the sphere. The polar plot generated in figure 20b emphasizes the angular dependence of the scattered light in dB. The pattern in polar coordinates also is in agreement with the results in Bohren [14] although not plotted in decibels the order of magnitude change in the scattering is correct.

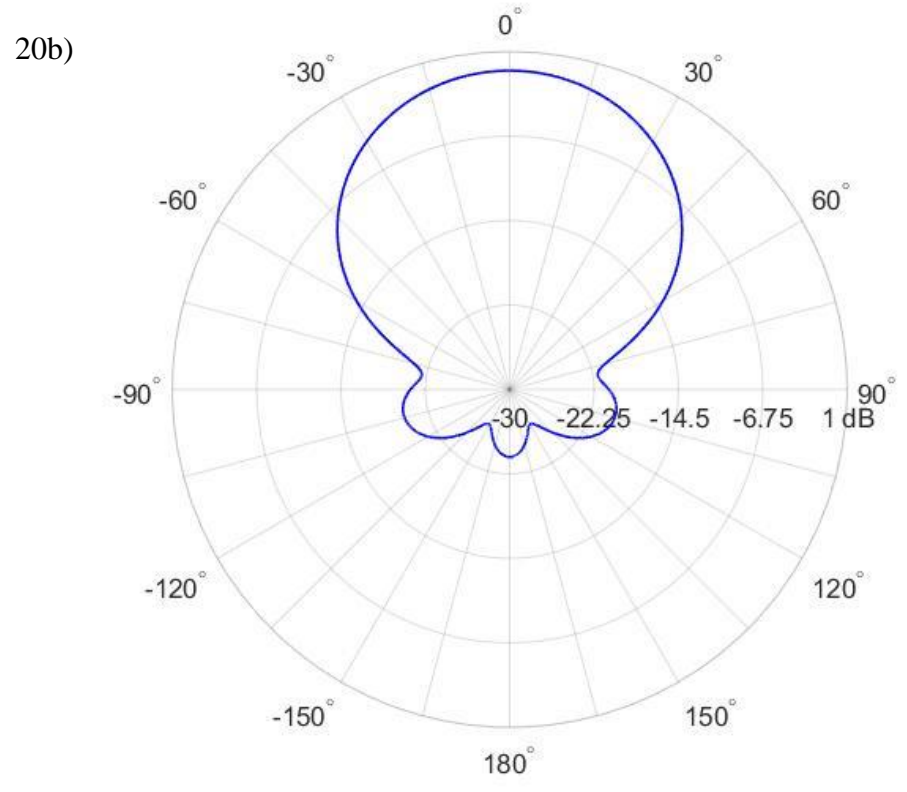
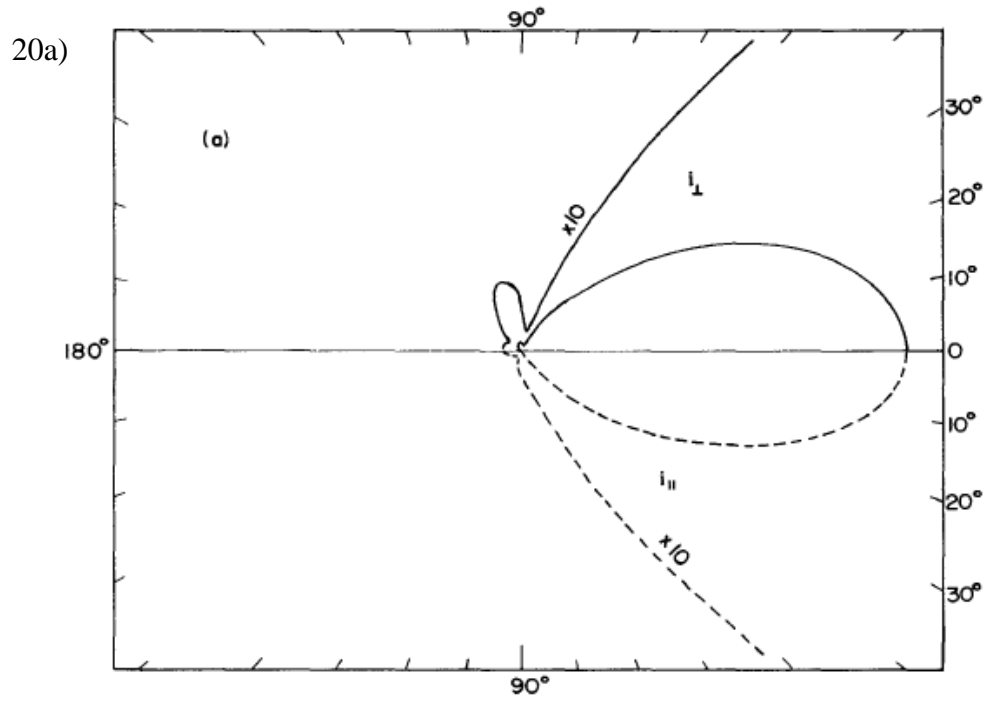


Figure 20: Logarithmic polar plot of Bohren [14] (20a) and this thesis' polar plot (20b) to visual the angular dependence of scattering.

3.2 Distribution Code

The next piece of code to test is the Mie scattering for a polydisperse system. To do this the single particle Mie code is turned into a function that returns the necessary parameters which are then weighted accordingly. The distributions modeled are of discrete particle sizes meaning the integrals in chapter 2.5.6 can be replaced with weighted summations for computational use [21].

To test this thesis' distribution code a test distribution is chosen to represent the particles. The distributions chosen are from Derimendjian's haze M and cloud C distributions models in [23]. The table of compared values with their percent error shown in table 11. The first tested distribution is the cloud C model given by Derimendjian (see equation 3.1.7) where the density is 100 cm^{-3} , the mean radius is $4 \text{ }\mu\text{m}$, and α as 6.

(3.1.7)

$$n(r) = 2.373r^6e^{-1.5r}$$

Then the second is the haze M model given by equation 3.1.8 with a mean radius of $0.05 \text{ }\mu\text{m}$ and $\alpha = 1$ with the same density. Each model is tested with different wavelengths and refractive indices where some albedo differed from unity.

$$n(r) = 5.33 \times 10^4 r e^{-8.944\sqrt{r}} \quad (3.1.8)$$

λ [μm]	$\Re\{m\}$	$\Im\{m\}$	Haze M			Cloud C		
			$\sigma_{true} km^{-1}$	$\sigma_{ext} km^{-1}$	Error (%)	$\sigma_{true} km^{-1}$	$\sigma_{ext} km^{-1}$	Error (%)
0.45	1.34	0	0.1206	0.1053	12.68	16.33	16.40	0.43
0.70	1.33	0	0.0759	0.0997	31.40	16.72	16.70	0.11
1.61	1.315	0	0.0312	0.0621	98.96	17.58	17.67	0.51
2.25	1.29	0	0.0194	0.0330	70.06	18.21	18.28	0.38
3.07	1.525	0.082	0.0289	0.0527	82.21	18.58	18.59	0.05
3.09	1.353	0.0059	0.0128	0.0259	102.1	20.65	19.07	7.65
5.30	1.315	0.0143	0.0075	0.0067	11.33	24.01	24.03	0.09

Table 11: Comparison calculations to data obtained from [23] for various wavelengths and albedos.

In table 11 the value from Derimendjian's calculations is taken to be σ_{true} for each distribution. A simple percent error has been calculated for the extinction coefficient, σ_{ext} , obtained from the code outlined above. The haze M and C models have been tested and compared. The cloud C data is within reasonable agreement for each of wavelength and albedo combinations tested. But for the haze M model, the calculated extinction coefficients are not within reasonable agreement. The large errors are attributed to Derimendjian giving the distribution equation 3.1.8 as the shape of the curve shown in figure 13 but not giving the exact model radii chosen. In figure 13 it can be seen that the particle radii are cut off at $0.01\mu\text{m}$ and a sharp cutoff around $2.1\mu\text{m}$. The range of model radii chosen strongly impact the extinction coefficient and if the incorrect model radii are chosen the extinction coefficients will differ. In the case of haze M, the function in 3.1.8 is still used but with a continuous radii distribution over the range of $0.01\mu\text{m}$ to $3\mu\text{m}$. This difference in the model radii used to represent the haze M distribution contribute to the large percent error.

Using computational techniques Mie theory has now been successfully implemented to predict how light scatters off of single particles along with polydisperse

systems. Atmospheric scattering in different weather conditions can now be approximated to first order which is presented in chapter 2.

Chapter 4: Forward Scattering Meter

The previous chapters provided the necessary background to understand how a forward scattering meter (FSM) works. The main working principles of the FSM are based on properties of atmospheric aerosol distributions. At a designated forward scattering angle, of 38° , the measured intensity scattered is seen to be directly proportional to the extinction coefficient regardless of the size distribution and maximum size of the particles. This relationship will be proven in this section of the paper so that the experimentally built FSM's final scattering angle will be proven to be an accurate angle to measure the atmospheric extinction coefficient.

The extinction coefficient does not become independent of particle size or density this is merely an observation of various particle distributions for haze, mist, and fog. This phenomena has been seen experimentally by Winstanley [35], Sakunov [37], Tyler [38], and Rozenberg [39] and theoretically by Derimendjian [23]. This section is intended to show this proportionality between scattered intensity and aerosol extinction coefficient using the theory and computational techniques discussed in the previous chapters.

To predict this forward angle a similar process is used from [35]. For the following calculations, the incident light on the aerosol distributions is assumed to be unpolarized, equation 4.1.1, so that the phase functions will have the same form as given in equation 2.5.59 for a polydisperse system.

$$I_{in} = \frac{I_{\perp} + I_{\parallel}}{2} \quad (4.1.1)$$

The distributions that are taken into consideration are models of haze, fog, and mist using the modified gamma distribution as in section 2.10. In figure 19a forty-five SSPFs are plotted with model radii of 0.01 μm to 25 μm in step sizes of 0.1 μm , shape parameter of 1, and mean radius varying from 0.2 μm to 9 μm in steps of 0.2 μm . Note that the mean radius does not have anything to do with a variance of the distribution, it merely is a place holder as the maximum value of the gamma distribution. Distributions with a larger particle mean produce more forward and backward scattered light compared to the smaller mean particle distributions. The phase functions plotted are now explicitly labeled as dependent mean particle radius and scattering angle

$$\rho(r_c, r, \theta) = \frac{1}{2} \left(\frac{P_1(r_c, \theta)}{4\pi} + \frac{P_2(r_c, \theta)}{4\pi} \right). \quad (4.1.2)$$

The phase functions do not depend on number density since it is a scaling factor on the final extinction coefficient. By inspection, it is seen that between the angles of 20°- 55° the phase functions come close to sharing a common value illustrated in figure 21b. Figure 19b provides a cross-sectional view of the forty-five phase functions in figure 21a at specific scattering angles. To the right of the red bracket, in 21b, are scattering angles 20-55° that maintain an almost constant value across all particle distributions.

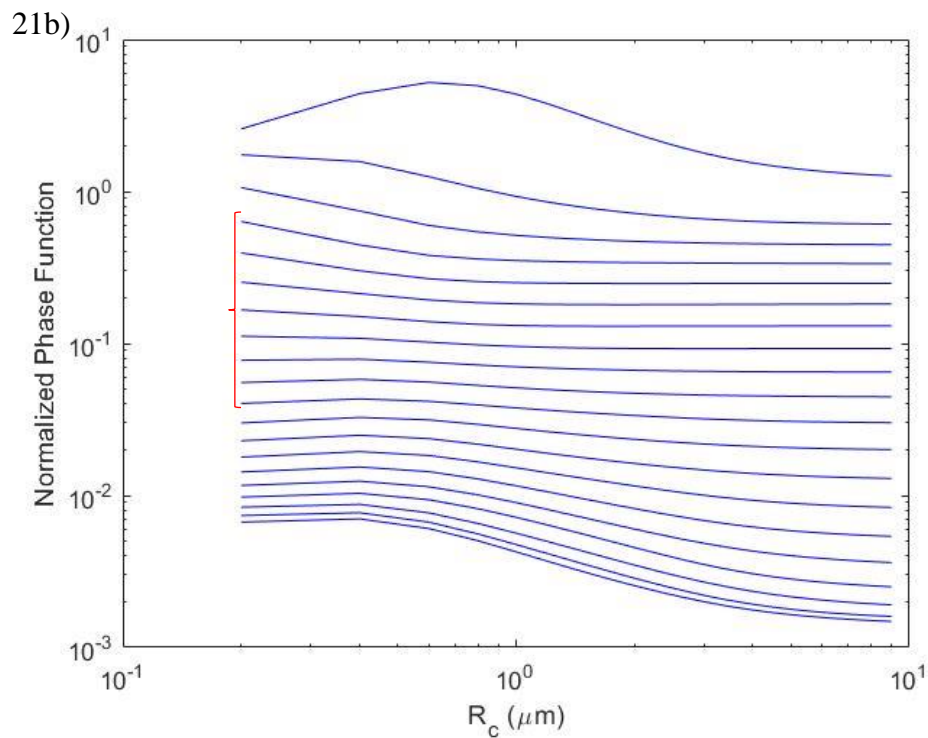
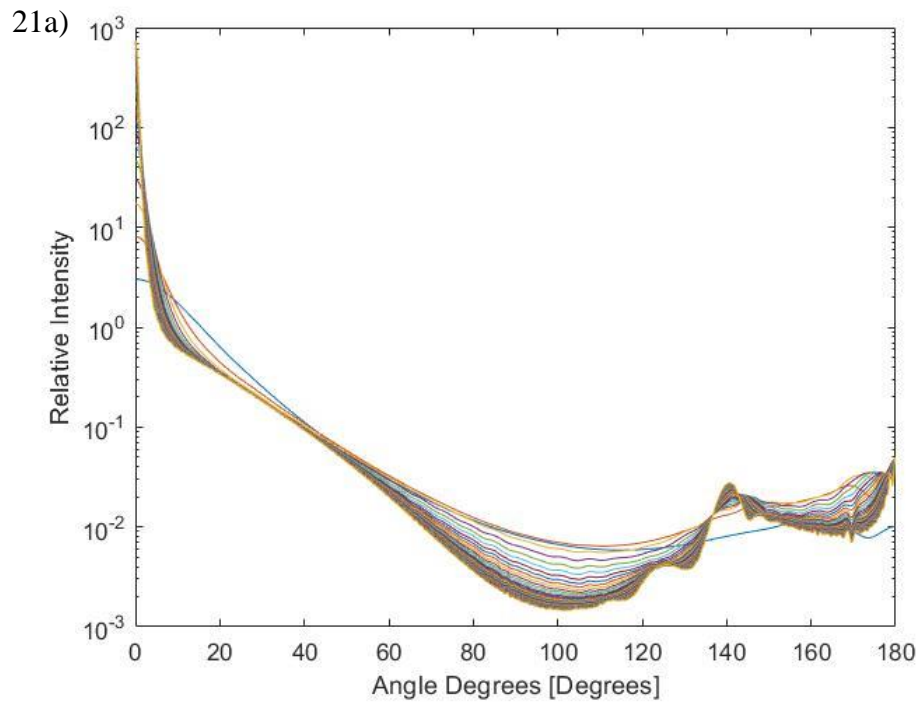


Figure 21: Forty-five phase functions (21a) with shape parameter $\alpha = 1$ with $0.850\mu\text{m}$ incident light and particle index of refraction of $1.329 - 2.93 \times 10^{-7}i$ [30]. (21b) is a cross-sectional plot of (21a), where the top line is the cross-section at 5° and moves down in increments of 5° where the last line represents 100° .

The shape parameter, α , is then varied between 1-6 with the same model radii and range of mean particle values for a total of 270 unique aerosol distributions with SSPFs of the form of equation 4.1.2. The cross-section of the phase functions is then taken for all variations of α and also determined to be most linear in the ranges 20°-55°.

The following example will show how to calculate the intensity at a specific angle, in this example $\theta = 35^\circ$. Using equations 4.1.2 and 2.5.1 (same equation as 4.1.3) with the substitution for θ , equation 4.1.4 will return the theoretical value of the scattered light intensity. This is how each of the phase function cross-sections are made only to be dependent on the distribution parameters in figure 21b.

$$I(\theta) = I_0 \sigma_{ext} \rho(r_c, r, \theta) \cdot \hat{I} \quad (4.1.3)$$

$$\rho(r_c, r, 35^\circ) = \frac{\sigma_{ext}(r_c)}{2} \left(\frac{P_1(r_c, 35^\circ)}{4\pi} + \frac{P_2(r_c, 35^\circ)}{4\pi} \right) \quad (4.1.4)$$

The normalized intensity, equation 4.1.5, is calculated for each angle within the range of 10°- 100° with a resolution of 1° along with the extinction coefficient, σ_{ext} , for each distribution.

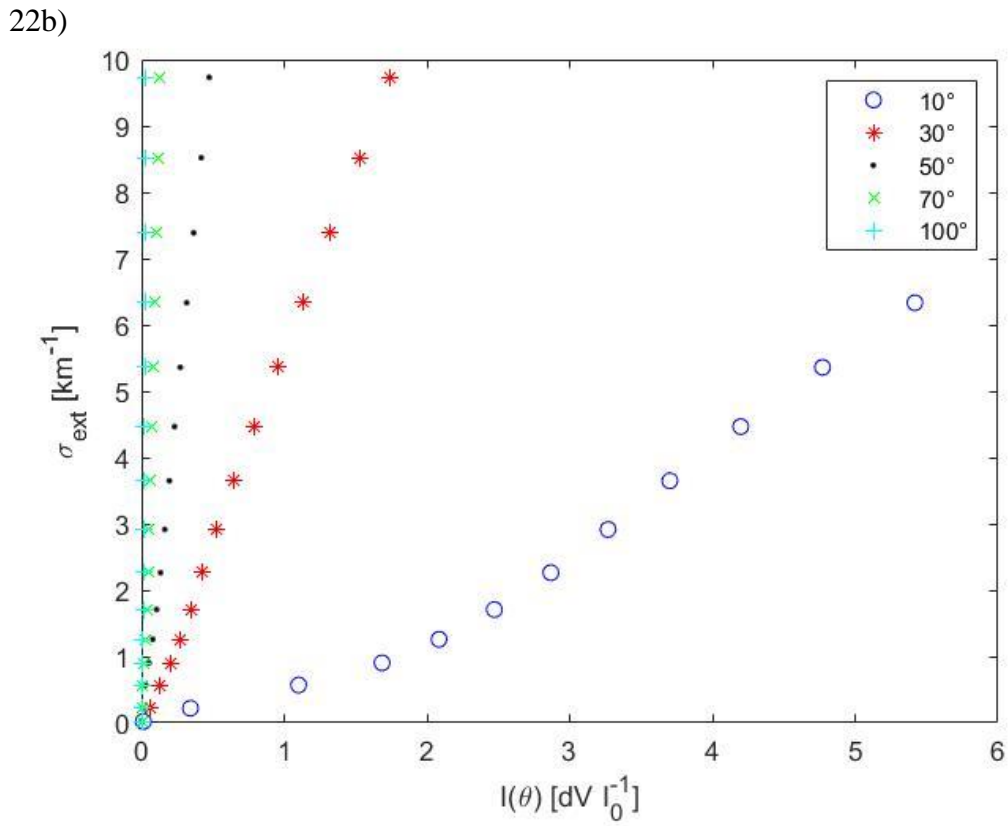
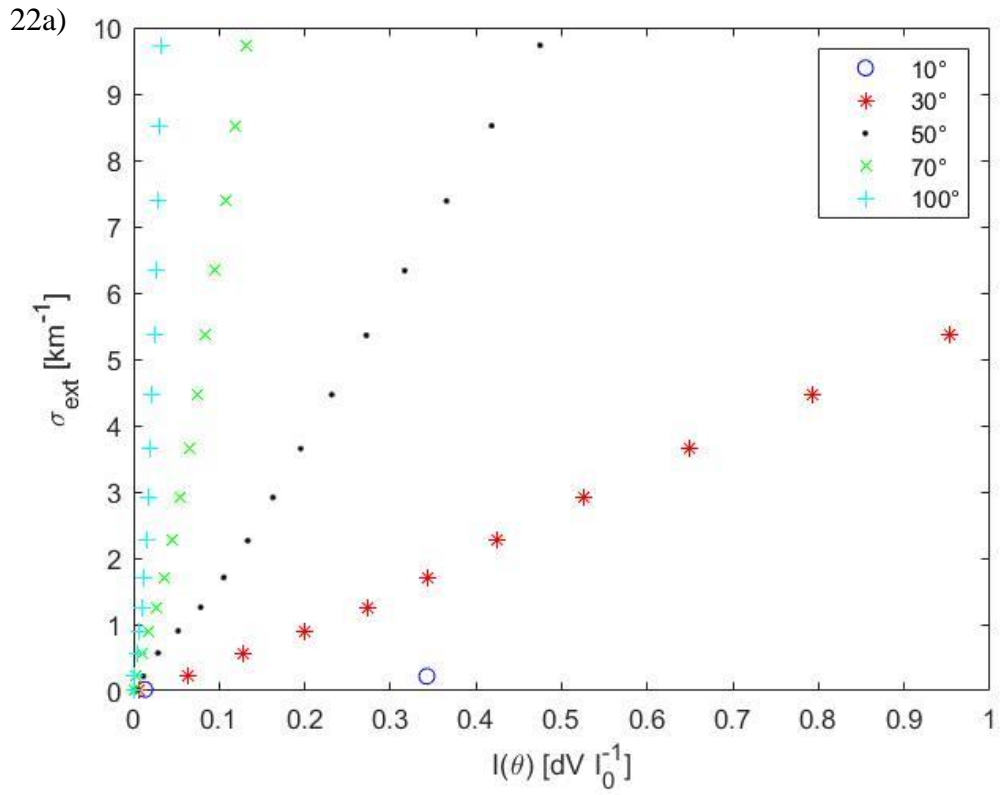
$$\frac{I(r_c, \theta)}{\sigma_{ext}(r_c)} = \frac{1}{2} \left(\frac{P_1(r_c, \theta)}{4\pi} + \frac{P_2(r_c, \theta)}{4\pi} \right) \quad (4.1.5)$$

The normalized intensity in equation 4.1.5 has an incident intensity, I_0 , of $1Wm^{-2}$ for all computational calculations but in practice will take on the incident power of the light source.

To find the scattered intensity the extinction coefficient is multiplied to the right side of equation 4.1.5

$$I(r_c, \theta) = \frac{1}{2} \sigma_{ext}(r_c) \left(\frac{P_1(r_c, \theta)}{4\pi} + \frac{P_2(r_c, \theta)}{4\pi} \right). \quad (4.1.6)$$

To show that the intensity is directly proportional to the extinction coefficient at a specific scattering angle the extinction coefficient is plotted against the scattered intensity, with units per unit incident intensity per unit volume, found in equation 4.1.6 for various values of θ . Each computed point on the graphs in figure 22-23 represent the scattered light of different particle distributions with a different r_c . The line is a “cross-section” of the phase functions in figure 21a. An example of this relationship is plotted in figure 22 where the computed points are for each distribution and the line of best fit is found by using a linear least square best fit.



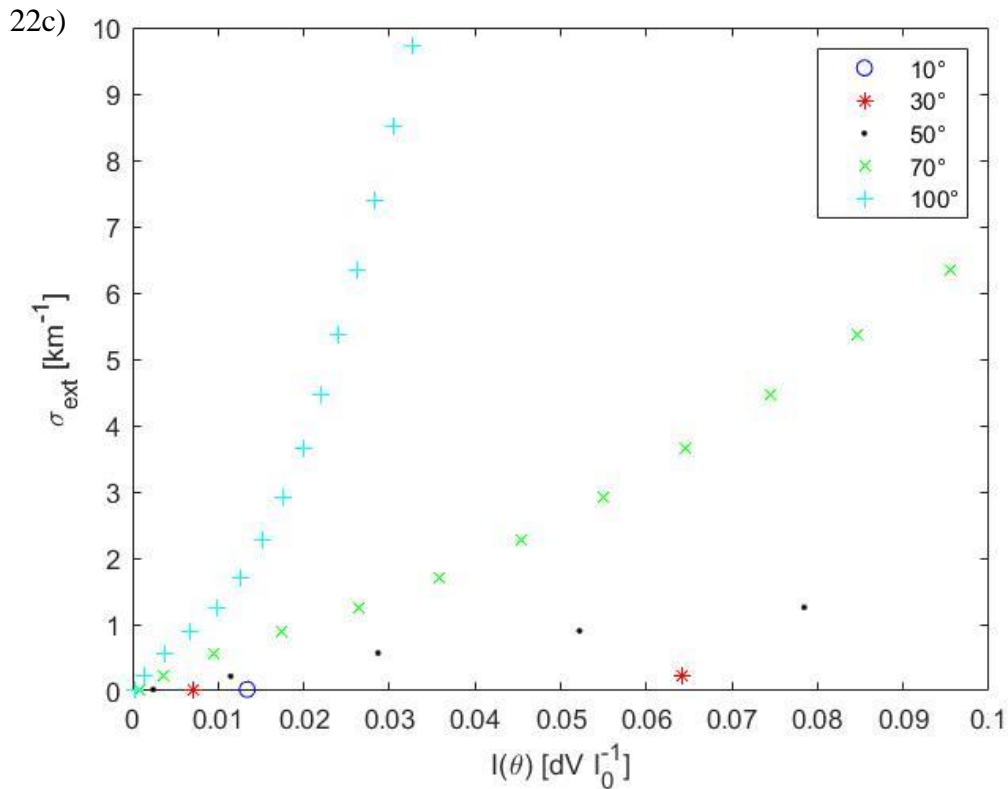


Figure 22: Plots to display the proportionality between the scattered intensity and extinction coefficient (22a). 22b shows points at 10° which do not fall on a line. 22c shows that points at large angles, 70° and 100° , do not fall on a line for small intensity.

In figure 22b some points do not fit a linear relationship of the extinction coefficient vs scattered intensity at 10° for large scattering intensity. The same phenomena can be seen for the higher scattering angles above 50° in figure 22c where 70° and 100° have points falling off a linear relationship at small scattering intensity. As the scattering intensity increases angles around 50° can be seen to have points that do not follow a linear relationship as seen in figure 22a. Angles around 30° are the best fit for finding the linear relationship between extinction coefficient vs. scattering angle. Each of these plots is obtained for the $\alpha = 1$ case for simplicity. To show that the angles

around 30° are the best fit for finding this linear relationship the best line of fit has been calculated for scattering angles 30° , 35° , 38° , 40° , and 42° shown in figure 23.

The best line of fit is calculated for each set of distributions and the most linear angle is found by finding the root mean squared error for each fit which is then plotted against angle in figure 24a. The most linear region is between 20° - 40° with a maximum value of the root mean squared error at 38° which will be used as the forward scattering angle of measurement. It can be seen that angles besides 38° also have a strong linear relationship between the extinction coefficient and scattered intensity. The scattering angle of 38° is not the same as the angle used in commercial designs that are mentioned in this paper (see table 2). This is because the particle distributions taken into account and procedure to determine the optimal angle in this thesis are different than commercial designs. In the user manuals for the FSMs mentioned in table 2, no discussion is added on how the scattering angle is proven. This means there is no way

of knowing the exact procedure each company determined their scattering angle since the information has seemed to be withheld.

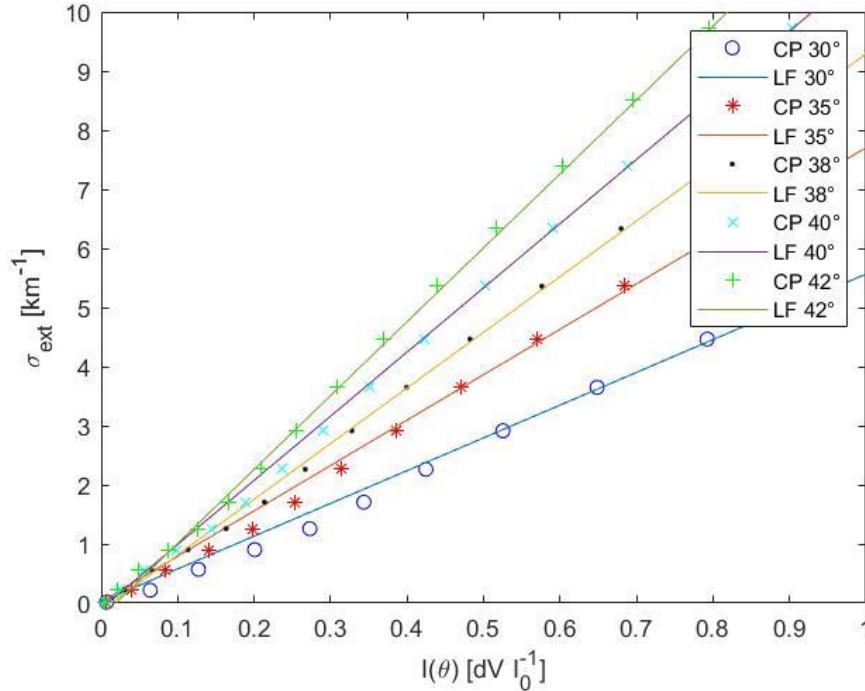


Figure 23: Computed points (CP) plotted with their best line of fit (LF) for specific forward scattering angles that linearize $\sigma_{ext}(r_c, r)$ vs. $I(r_c, r, \theta)$.

The difference in scattering angle can be from the approximations of Mie theory used or particle distributions were chosen or calculation parameters. Other aerosol distributions have not been considered which will limit the accuracy of the extinction coefficient measurement, especially in precipitation. Other distribution considerations will be mentioned in chapter 7. At this point, a forward scattering angle has been determined for use for the implementation of an FSM to measure atmospheric visibility through fog, mist, and haze. The foundation for this measurement is that for an angle of 38° the atmospheric extinction coefficient, σ_{ext} , is proportional to the intensity of the scattered light. The scattered light can be measured using photodetectors and an

extinction coefficient can be extracted where the Koschmieder formula equation 2.10.1 can be applied to determine the atmospheric visibility using a lab-built FSM.

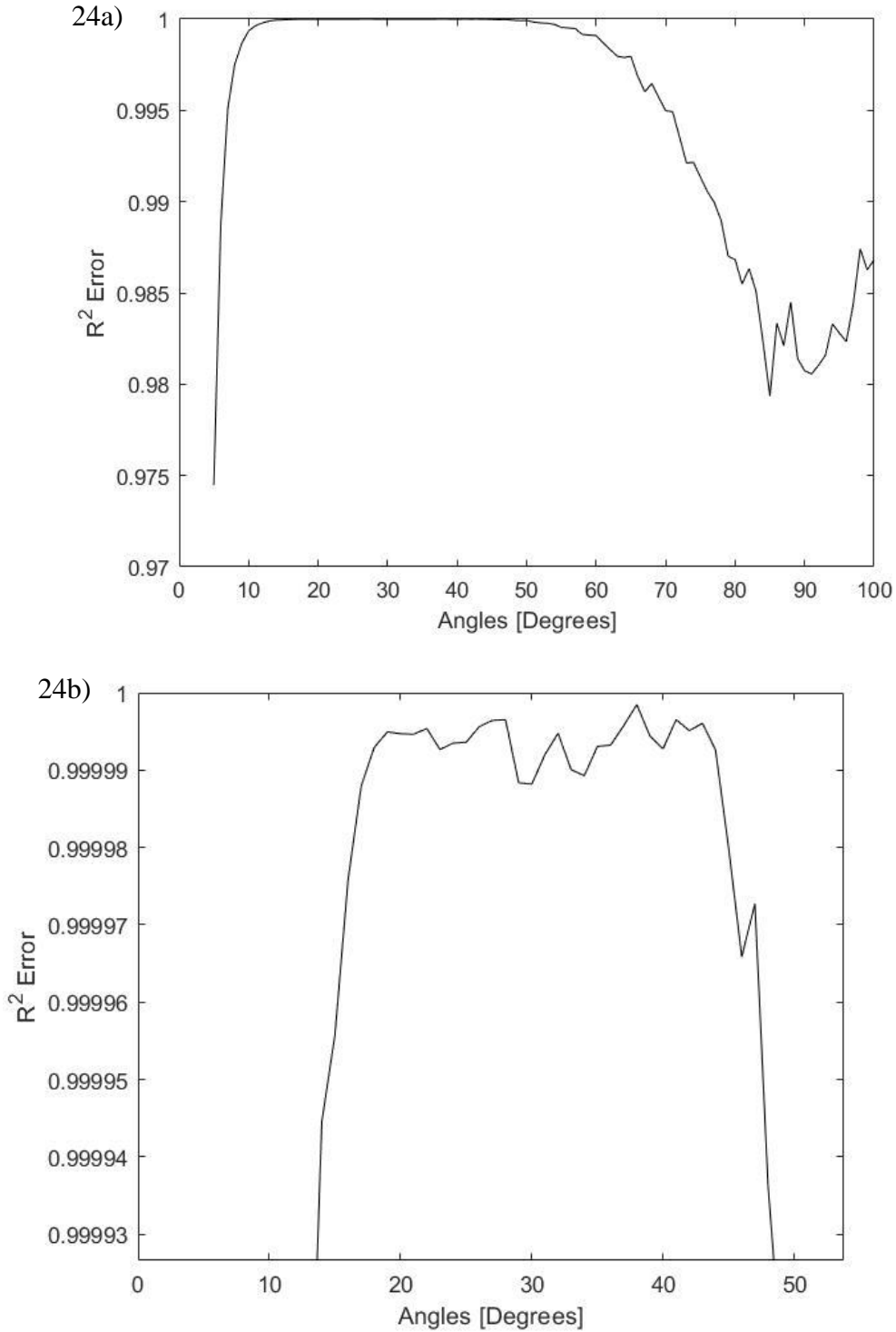


Figure 24: Root mean squared error for best lines of fits through all distributions for various forward scattering angles (24a) with a zoomed in image of the ideal range of scattering angles (24b).

Chapter 5: Experimental Design

Going through all the fundamental theory builds the foundation for the following experimental section where two designs of an FSM have been built. The first design is a small single structure device with a 2 ml sampling volume whereas the second device is a larger device with a 150 ml sampling volume. The main design parameters will be discussed in detail and how various problems with each design limit their measurement capability.

5.1 FSM Design One: 2ml Sampling Volume

5.1.1 Optical Design

To start the project, the optical layout is designed and tested on an optical table before making an enclosure. The optical design includes the pathlength, light source, detectors, lens, filters, and scattering volume. Before choosing other optical parts the pathlength must be chosen appropriately. To make the SSPF models in the previous chapter applicable to the FSM design the single scattering condition, $\sigma_{sca}l \ll 1$, must be met. To determine if this is true the estimated maximum extinction to be measured is 100 km^{-1} through a maximum distance between detectors of 0.4m. The product is 0.04 which is two orders of magnitude smaller than one and therefore satisfies the single scattering condition. The estimate of maximum attenuation comes from the previous calculations in chapter 4 of dense fog models.

The angle chosen for detector placement determined in the previous chapter was 38° . The original 2 ml sampling volume design included an earlier calculated angle of 35° from September that was used for the first design. The motivation of this scattering angle was developed from preliminary calculations similar to that mentioned

in chapter 4 but with less aerosol distributions. This angle was also convincing due to it being the same angle found by Winstanley and Adams in [35]. Later on, in this thesis the angle was recalculated to be 38° after considering more particle distributions for the 150 ml design which were not used in the 2 ml design. But, the angle of 35° is also still considered an acceptable scattering angles having a high linear correlation between the scattered intensity and extinction coefficient as shown in figure 24b.

The selected light source is a 200 mW $0.850\ \mu\text{m}$ unpolarized laser diode model L850P200. The polarization of the laser was confirmed by using polarizer sheets. The reasons leading to the choice of this light source choice include molecular scattering, molecular absorption, scattering properties, availability, and eye safety. The main reason is to increase the Mie scattering properties of the modeled aerosols by keeping $\lambda r^{-1} \approx 1$. In front of the laser diode, a 25.4 mm aspheric condenser lens is used to collimate the diode. The power is more than needed but due to the large beam divergence angles, parallel and perpendicular to the diode junction, an iris is placed in front of the lens to spatially filter the sides of the beam and keep the beam cleaner as it enters the scattering volume. The power going into the reference channel is $\sim 10\ \text{mW}$.

To measure the scattered light SM1PD1A Si-photodiodes are used due to their large area, mount threads, and large responsivity at $0.850\ \mu\text{m}$. The main disadvantage is the dark current of 600 nA. Both the reference and scattering channel contain the same photodiode.

Since this device will be used outside it is important to use bandpass filters at $0.850\ \mu\text{m}$ due to the large amount of background sunlight during the day. The bandpass filters used in this case are 10 nm wide. The use of 2 nm wide bandpass filters was

considered but due to the wavelength spectrum of the laser diode too much light would be rejected. A final picture of the optical layout is shown in figure 25.

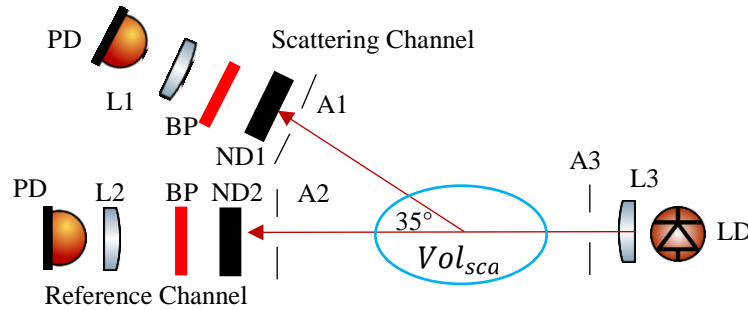


Figure 25: Optical layout of filters, lenses, photodiodes, and laser diode set at the scattering angle of 35°. L1, L2, L3 are 25.4mm aspheric condenser lenses. BPs represent bandpass filters. ND1 is the 2 neutral density filter whereas ND2 is the 0.3 neutral density filter. A1, A2, A3 all represent the apertures which are created by adjustable iris. LD is the 0.850 μm laser diode and PD are the photodiodes.

The scattering volume is calculated from cylindrical geometry where the volume is the intersection volume of two cylinders with a maximum radius of 25 mm. The volume can be calculated using equation 5.1.1 where θ is the angle offset. The maximum volume that this FSM samples is 2.0 ml. This is a much smaller volume compared to commercial visibility meters due to the mounts of the optics being SM1 threaded optical tubes. The SM1 optical tubes were chosen since they were easy to mount and scattering volume was not considered a problem yet in this design. The design was also based off of Winstanley [35] which had the same size scattering volume. But their testing was only done in thick fog which allowed for enough aerosols to fill the scattering volume. They did not publish data taken in clear weather conditions where a small sampling volume becomes a problem which will be discussed later on.

$$Vol_{sca} = \frac{16r^3}{3\sin(\theta)} \quad (5.1.1)$$

For calibration purposes, and increase in measurement sensitivity, neutral density filters (ND) are used. On the main reference channel, a 0.3 ND is used and on the scattering channel 2 ND. Adding NDs to the scattering channel also increase the measurable dynamic range so that greater extinction coefficients can be measured. The trade-off is calibrating the device to pick up the scattering signal in clear weather while also decreasing the maximum range in clear weather.

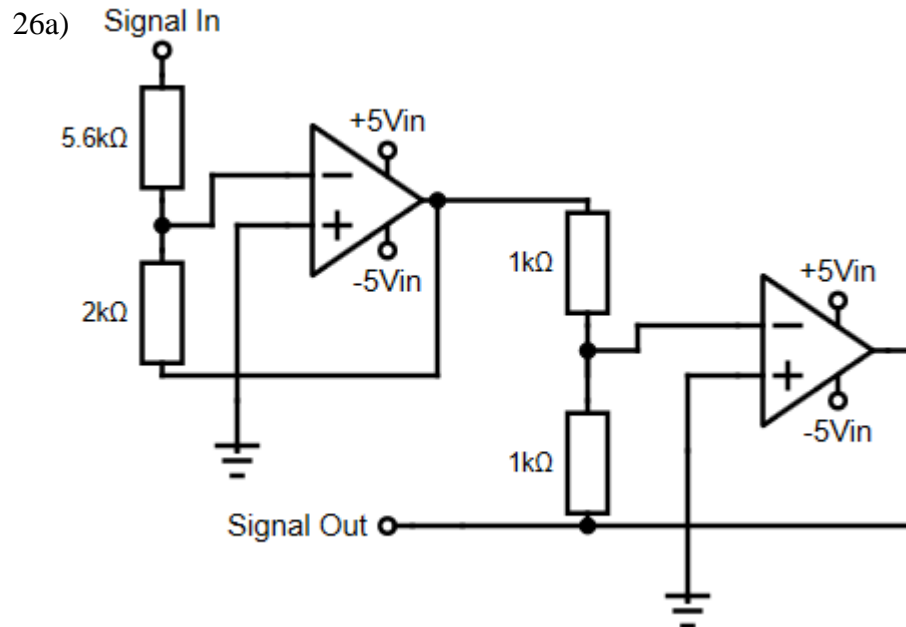
5.1.2 Electronics Design

The FSM electronics are made-up of four different electrical components: reference amplifier, scattering amplifier, power supply, and modulation circuit. All the circuits were tested on breadboards initially then mounted on printed circuit boards (PCB) that were designed to minimize noise and allow for portability. The PCB design was done in KiCad and ordered from JLC PCB.

The first circuits designed were transimpedance amplifiers (TIA), figure 26a, for the photodiodes to convert the photocurrent into a usable voltage. The amplifiers are powered with a ± 5 V DC input from an RS-0505D DC/DC converter using a 9 V battery located on the TIA PCBs in figure 27. The operational amplifiers originally used were OP27E's but due to the DC input current of 10 nA, a high DC offset limited the dynamic range. To bypass this issue AD823 op-amps are used with a 3 pA input bias current reducing the input DC offset. For the TIA design, a feedback resistor of 20 k Ω is chosen for the reference channel so that the main beam signal would not saturate at the 5 V voltage rail. The scattering channel feedback resistor of 10 M Ω is chosen due to the order of magnitude of the scattered light. Using an incident power of 10 mW upon the previous modeled aerosol distributions will place the scattering power

in fog to be $\sim 1 \mu W$. Whereas in clear weather the scattering signal will be on the order of magnitude of $\sim 0.1 \text{ nW}$. Each of the channels has a feedback capacitor of 68 pF to minimize the background noise of the amplifier.

There are also inverting amplifiers used to down step the voltage to a maximum of 3.3 V , figure 2ab, when a data acquisition board operating at this voltage. This circuit was initially placed on the board to deal with using the 3.3 V pins on an Arduino DUO with a 12-bit analog to digital converter (ADC).



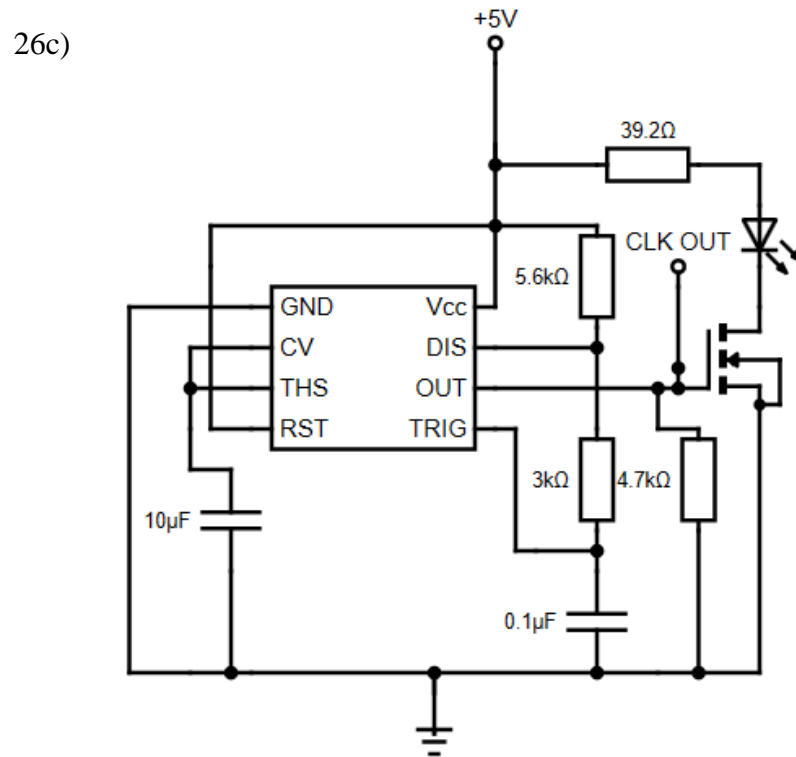
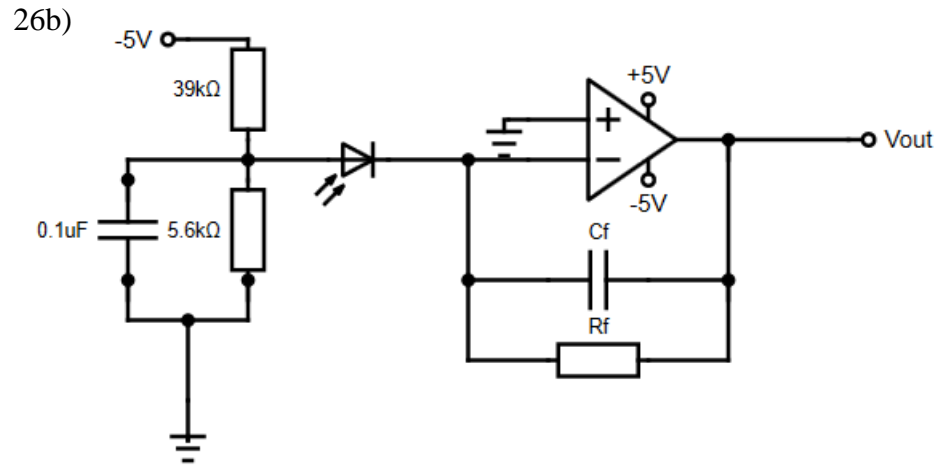


Figure 26: Circuit layout for the TIAs for the photodetectors (26a), 5V in to 3.3V out cascaded op-amps using AD823's (24b), and 555 timer laser diode modulation circuit (26c).

The modulation circuit, figure 26c, consists of a LM555 timer IC with components to produce a 10 Hz pulse with a 52% duty cycle. The modulation turns the laser diode on and off so that the scattered light can easily be extracted from the background signal. To drive the, rather large, laser diode an n-channel field effect

transistor (NFET) is used to produce the current needed of 50 mA. The modulation signal is very small, which means that the TIA circuit does not need to be designed to produce a large bandwidth of amplification.

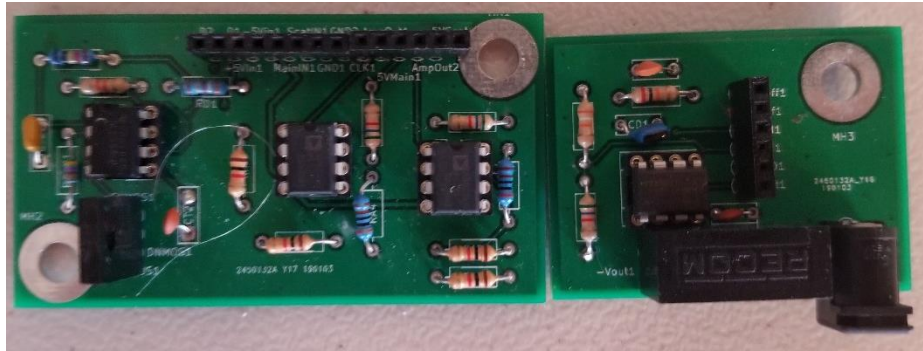


Figure 27: PCB design without the front copper ground plane for the modulation circuit (left) with down step amplifiers. TIA PCB is on the right containing the DC/DC converter power supply.

Outputs of the main board, containing the extra amplifiers and LM555 timer, are connected to the voltage output of the scattering, reference, and clock signal which are sent to an ADS1252 24bit ADC (18 effective bits) mounted on a Raspberry PI Model B+ in figure 28. The ADS1252 is chosen to provide more significant bits compared to an Arduino UNO (10 - bits) and Arduino DUO, initially used. This increased the performance of the scattering channel sensitivity for clear weather conditions assuming noise can be taken out of the circuit.

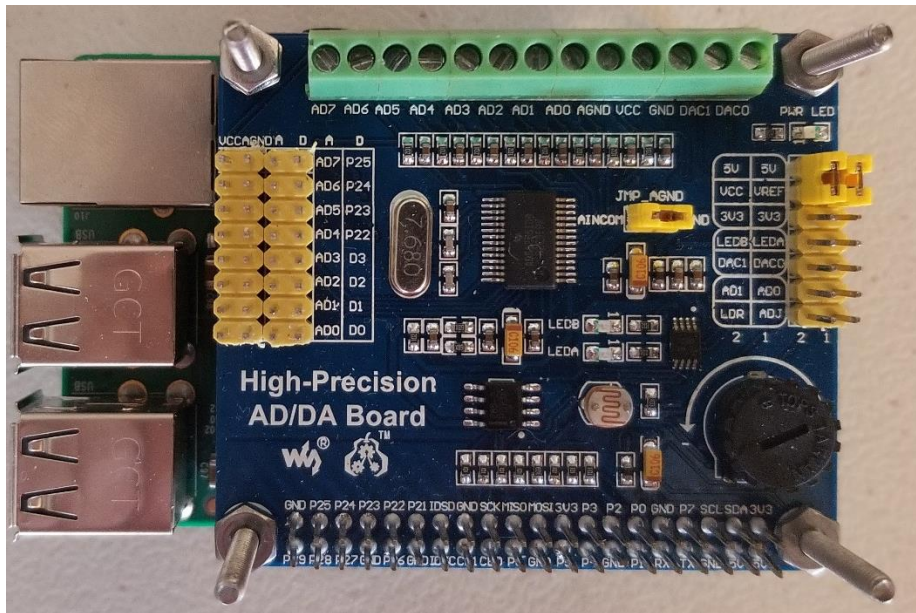


Figure 28: Raspberry Pi B+ above with attached ADS1256 board.

To reduce noise on the PCBs ground planes were added along with vias to maintain a constant voltage across the entire plane. The PCB in figure 25a contains the modulation circuit along with op-amps to step the voltage down to a 3.3 V dynamic range. The TIA PCB (figure 27 right) is made to fit close behind the output of the photodiodes to reduce the distance the un-amplified signal has to travel. Noise has been seen to be significantly reduced except when inside the lab directly next to live power cords.

5.1.3 Mechanical Design

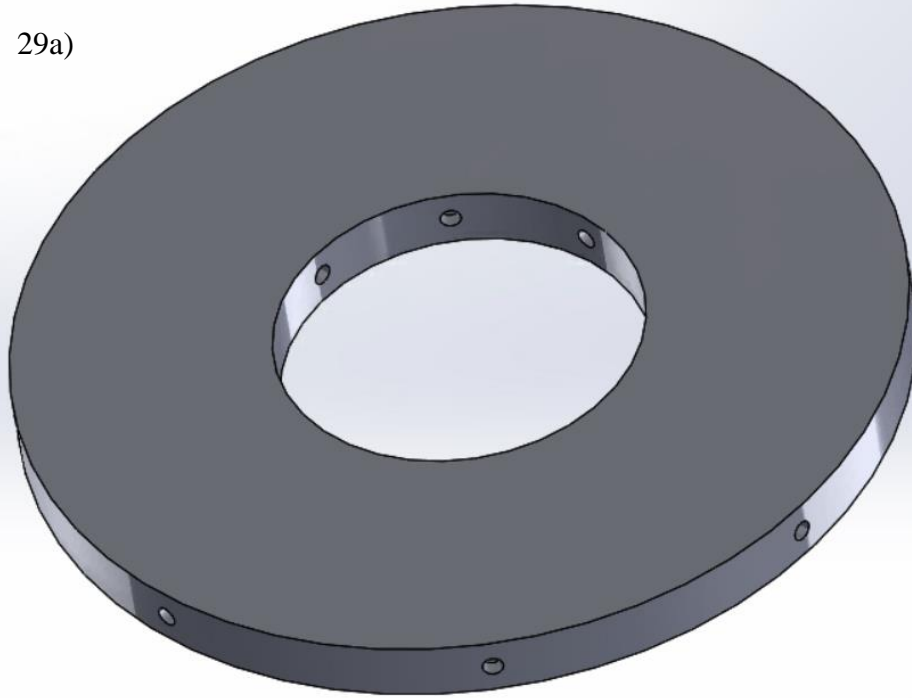
The encasing of the FSM is designed around the optical layout that monitors the scattering of aerosol within the sampling volume. The sampling volume, Vol_{sca} , is the region where the field of view (FOV) of the detector and beam intersect. By making the optical layout as compact as possible the design becomes simpler and more portable. The encasing for the optical layout and electronics is all 3D printed using

polylactic acid (PLA) and designed in SolidWorks along with the generation of the stereolithography (STL) files.

The design is made to mount the laser and photodetectors in 1-inch SM1 optical tubes at an angle of 35° . The inner circle diameter is 12.8cm which is the distance from the scattering channel input aperture to the laser diode output aperture as seen in figure 25. This distance is well within the single scattering regime to prevent multi-scattering effects. The outer diameter is 27.4cm and 9cm tall to house the electronics, power supplies, and Raspberry PI along with a top for the base in figure 29.

Later on, due to incorrect spacing requirements for the detector PCB's, a 3D printed add-on to the final design was made and printed in figure 30. The dimensions of the add-on are 10cm x 18cm x 9cm and a curve on one side to fit the curvature of the original base in figure 29b. To mount the detector outside screw holes were cut to mount the device on a tripod to raise it to 1.5m above the ground. The WMO guidelines state that visibility measurements should be made at this height because it is the average height of an observer [18].

29a)



29b)

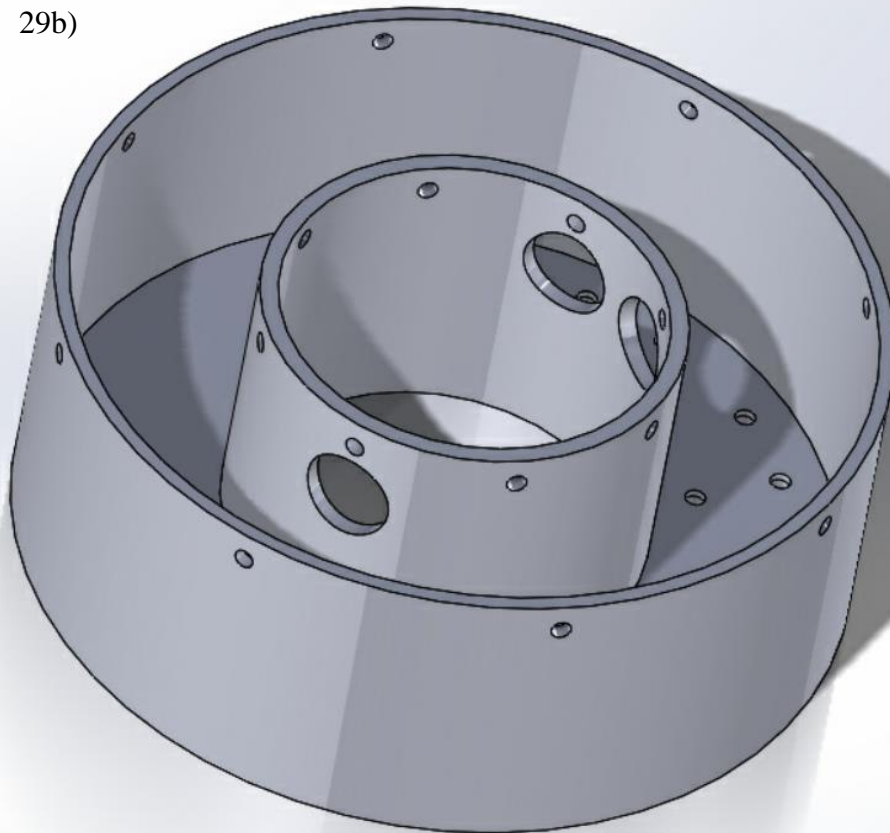
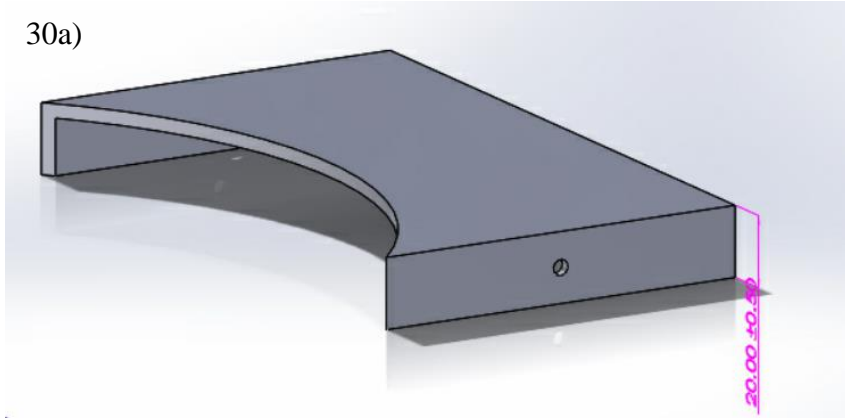


Figure 29: Top (29a) and base (29b) of the first design where the holes in 29b are made to fit 1-inch optical tubes and 0° and 35°.

30a)



30b)

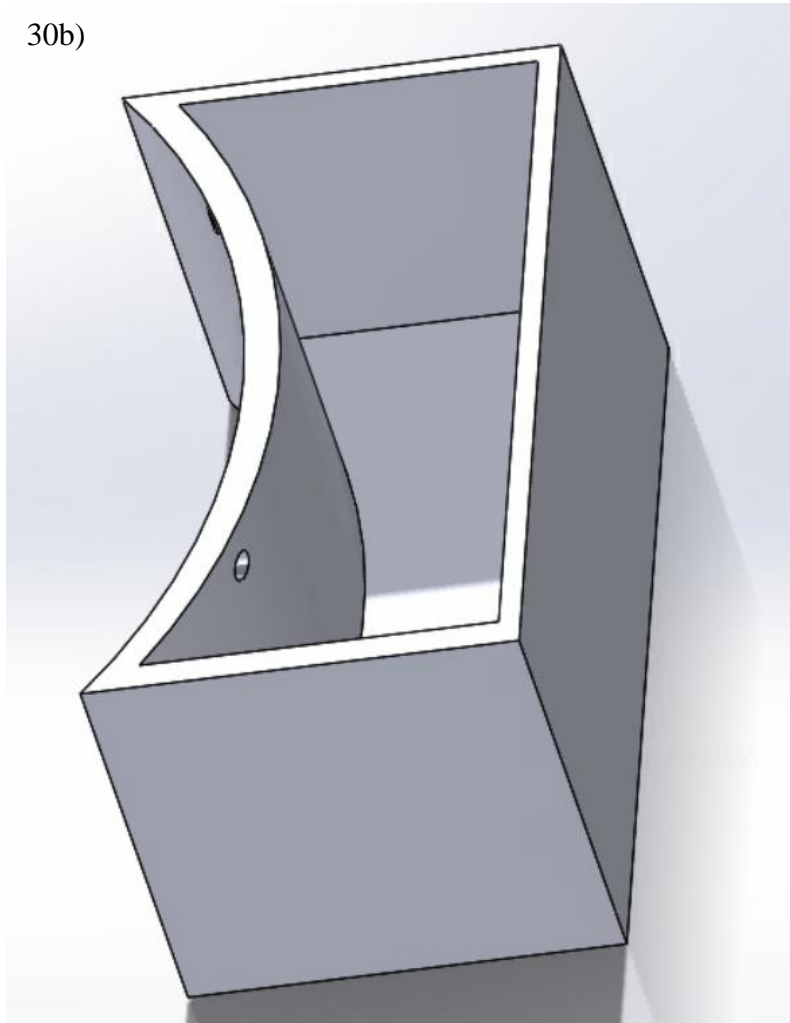


Figure 30: Top (30a) to addon base (30b) to fit the detector electronics

5.1.4 Data Processing

The voltage signals from the TIAs are read using an ADS1256 board adapted to fit on a Raspberry Pi (RP) programmed in C with the code provided in the appendix. The data is read in through the normal ADC channels and saved to a text file with a specific sample number to increase sampling speed. The ADC is sampling at 160 Hz which is more than enough resolution for a 10Hz signal without aliasing or under-sampling and to pick up quick transients caused by the movement of aerosol particles in the sampling volume.

The post-processing is done in MATLAB after importing the text files from the RP. To obtain the extinction coefficient as a function of time the samples are averaged over a window of 10 minutes to track changes in visibility. This window is subject to change depending on the length of the measurement. If the measurement duration is less than two hours, it was noticed, that a 10-minute averaging window provided poor visibility transients so it was changed to a 5-minute averaging window. If the measurement duration is greater than 2 hours then a 10-minute averaging window is used and provides enough transients in visibility. The visibility transients, to be considered as distinct changes in weather, should be on the order of a few minutes so averaging over 5-minute and 10-minute windows reduce the noise and quick variations in visibility.

To find the amount of scattered light from the scattering volume, the modulation clock signal is directly read into the ADC on the RP. Every ~15-seconds, or 2500 samples within the averaging window, the background signal is calculated when the

clock is low. The 15 second background signal is subtracted from the signal when the clock is high to determine the scattered light signal.

To calculate the scattered intensity the photocurrent can be related to the voltage of the TIA

$$V_{sca} = \frac{I_{pd}R_f}{1 + 2i\pi f R_f C_f}. \quad (5.1.2)$$

Equation 5.1.2 is the voltage output of a standard TIA amplifier where: I_{pd} is the photocurrent, R_f (Ω) is the feedback resistance, C_f (F) is the feedback capacitance, f (Hz) is the signal frequency, and V_{sca} is the output of voltage for the scattering channel. Equation 5.1.2 can be simplified to a simple linear relationship in equation 5.1.3 because fR_fC_f is much less than one for the scattering channel due to C_f being 68pF, R_f being 10M Ω and f being 10 Hz.

$$V_{sca} = I_{pd}R_f \quad (5.1.3)$$

The scattered power can then be found from equation 5.1.4

$$P_{sca} = \frac{V_{sca}}{R_f * Resp} N_d. \quad (5.1.4)$$

Where $Resp$ (A/W) is the detector responsivity and N_d is the calibrated neutral density filter value. For the case of this use R_f is 10 M Ω , $Resp$ is 0.64 at 0.850 μm , N_d is ND of 6.0441, and V is the voltage of the scattered signal. The ND value is calibrated using an 0.850 μm source before being placed on the scattering channel. The intensity of the scattered light can be found then by dividing equation 5.1.4, where $Area$ is that of the photodiode used which is $6.3 \times 10^{-5} \text{m}^2$.

$$I_{sca} = \frac{V_{sca}}{A * R_f * Resp} N_d. \quad (5.1.5)$$

The next step after averaging the voltage and finding the intensity is to find the extinction coefficient. The theory of concept, presented in chapter 4, states that the scattered intensity is directly proportional to the extinction coefficient with proportionately constant κ and offset β in equation 5.1.6,

$$\sigma_{ext} = \kappa I_{sca} + \beta \quad (5.1.6)$$

After time averaging the signal and converting the scattering channel voltage to the extinction coefficient the data can be presented in three different ways. If the interest is in the extinction coefficient itself then time versus extinction coefficient will suffice. The second and main uses of this instrument are visibility measurements which are found from using the Koschmieder equation, equation 2.10.1, with MOR contrast threshold. The last value of interest is the power loss per kilometer, $\sigma_{dB/km}$, for free space optical communications

$$\sigma_{dB/km} = 10\sigma_{km^{-1}} \log(e). \quad (5.1.7)$$

Equation 5.1.7 is the conversion from $\sigma_{km^{-1}}$ to decibels which will be used in the experimental portion of this paper to convey visibility conditions to adopt to standard literature.

5.1.5 Calibration

To find the proportionately constant, κ , and zero offset, β , a calibration procedure is devised. The line in equation 5.1.6 is fit between two points, the first being the zero offset from the inherent background noise of the detector and the second point is the light reflected off a glass plate at 35° as shown in figure 31. The second point can be obtained through other various methods such as scattering plates, a known aerosol volume/concentration, or a commercial visibility meter. A glass plate is chosen because the light reflected off the plate is easy to calculate with Fresnel coefficients at an oblique angle for unpolarized light. With a glass plate of index 1.517 the unpolarized power reflection coefficient is 0.0431.

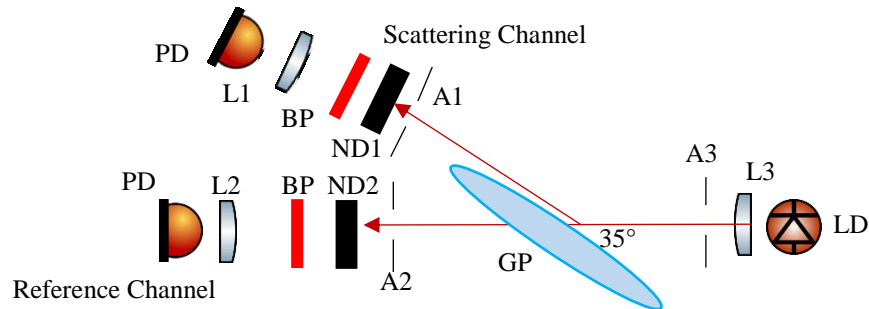


Figure 31: Experimental setup to scatter light into the scattering channel use a glass plate.

The procedure to obtain point one, P_{y1} , is done by turning off the light source and covering the detector from all background light and the intensity is obtained from equation 5.1.5 along with a known intensity, P_{x1} of 0 (W/m^2). Then the second point, P_{y2} is obtained from measuring the light scattered from the glass plate using a calibrated 3x ND filter so the detector is not saturated. The intensity, P_{x2} , is calculated with equation 5.1.4. Then the slope is found with the slope being

$$\kappa = \frac{P_{y2} - P_{y1}}{P_{x2} - P_{x1}}. \quad (5.1.8)$$

The instrument is now calibrated with respect to the known scattered intensity of the glass plate. This calibration technique will be used in all experiments in chapter 6 and the effectiveness will be shown.

The calibration is similar to that of the commercial visibility meters used in chapter one. Each meter uses a metal “scattering plate” with a known extinction coefficient to re-calibrate the device. This is similar to the above-mentioned technique except for the “scattering plate” being a glass plate and not metal.

5.2 FSM Design Two: 150ml Sampling Volume

5.2.1 Optical Design

The optical system for the second design has the same format as figure 25 but with a few changes as marked in figure 32. The changes were made to increase the sampling volume by at least 10 times. This is done by creating a beam expander in front of the collimated laser diode along with a diffuser plate before the beam expander. L3 and L4 in figure 32 make up a ~2x beam expander using a plano-convex lens, $f = 100 \text{ mm}$, with a meniscus, $f = -37 \text{ mm}$, placed at a distance of $f_1 + f_2$. The diffuser, marked in green on figure 32, is used to evenly distribute the laser light across the sampling volume which also helps to increase the effective sampling volume. L2 is changed to a 2-inch diameter plano-convex lens to catch light scattered within the larger sample volume which is then focused through a bandpass filter at $0.850 \mu\text{m}$ and then focused again onto the photodetector.

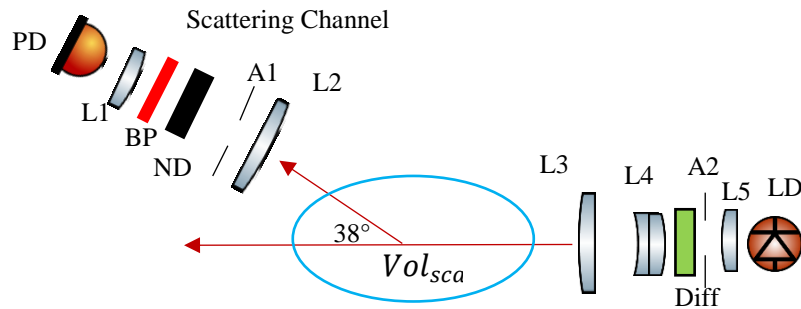


Figure 32: New optical layout for 150ml sampling volume.. PD is the scattering photodiode, LD is the laser diode, L represents the lenses, BP is an $0.850\ \mu\text{m}$ bandpass filter, ND is where a neutral density filter is placed if needed, and Diff is a 220 grit ground glass diffuser.

The reference channel was not used in this design due to it being unnecessary in the 2 ml FSM design after calibration of the scattering channel with the glass plate was implemented. This ended up being an issue in chapter 6 due to condensation building up on the lenses. The reference channel can be used to help fix the condensation problem which is discussed in chapter 7.

5.2.2 Electronics Design

The electronics design is the same as the first design, section 5.1.2, with the exception of using longer wires to carry the signal from the scattering PCB to the RP.

5.2.3 Mechanical Design

The design is placed on top of a wooden base using polyvinyl chloride (PVC) piping to house the optical tubes as shown in figure 33. The laser is fixed on the optical axis and the scattering channel is mounted in a swiveling base that is moved to 38° for this design and fixed for all measurements. The swiveling base is used due to the first design's static fixture being inconvenient to change the scattering angle if future calculations are made. This happened in the 2 ml design since an initial scattering angle of 35° was calculated and then after adding in more distributions was deemed the wrong choice of angle. By having the swivel this issue could be avoided in the future design

of the 150 ml FSM along with uses for future experiments outline in chapter 7. The electronics are stored below the base inside of an electrical box. As for waterproofing, the design is very water resistant when plastic bags are placed on the electrical box and top of the PVC. This allowed for extensive measurement time outside in the rain and the fog chamber compared to the 2ml FSM.



Figure 33: Mechanical design of the 150ml sampling volume meter with movable detector, fixed laser, and electrical box.

5.2.4 Data Processing

The same data processing and calibration techniques are used from section 5.1.4. The circuit calibration is redone due to the change in sampling volume but the same procedure outlined in 5.1.5 is used with the same glass plate.

Chapter 6: Experimental Verification

6.1 Florida December 2018: 2ml FSM

The first field test of the device was between December 3rd and 7th, 2018. The testing venue was on at NASA's Kennedy Space Center Shuttle Landing Facility (SLF)

runway. The experiments were done as part of the Atmospheric Propagation Studies for High Energy Lasers Program (APSHL) sponsored by the Office of Naval Research (ONR) done in conjunction with the University of Central Florida (UCF) Townes Institute Science and Technology Experimentation Facility (TISTEF) and AFIT.

This experiment, mounted in figure 31a and 31b, did not return any useable data due to no bandpass filters at 0.850 μm on the scattering channel and as a consequence, the detectors were saturated to the 5V rail. Due to the saturation, the scattered light pulses could not be differentiated from the background light. When this was discovered as the issue, ND filters were placed onto the scattering channel which brought the background down below the 5 V rail, but even then, the scattering signal could not be differentiated from the background light. This problem appears to be caused by the use of long pass and short pass glass filters on the scattering channel that did not work well outside and with the 0.850 μm light source. To solve these issues bandpass filters at 0.850 μm were bought which will be used in all future design.

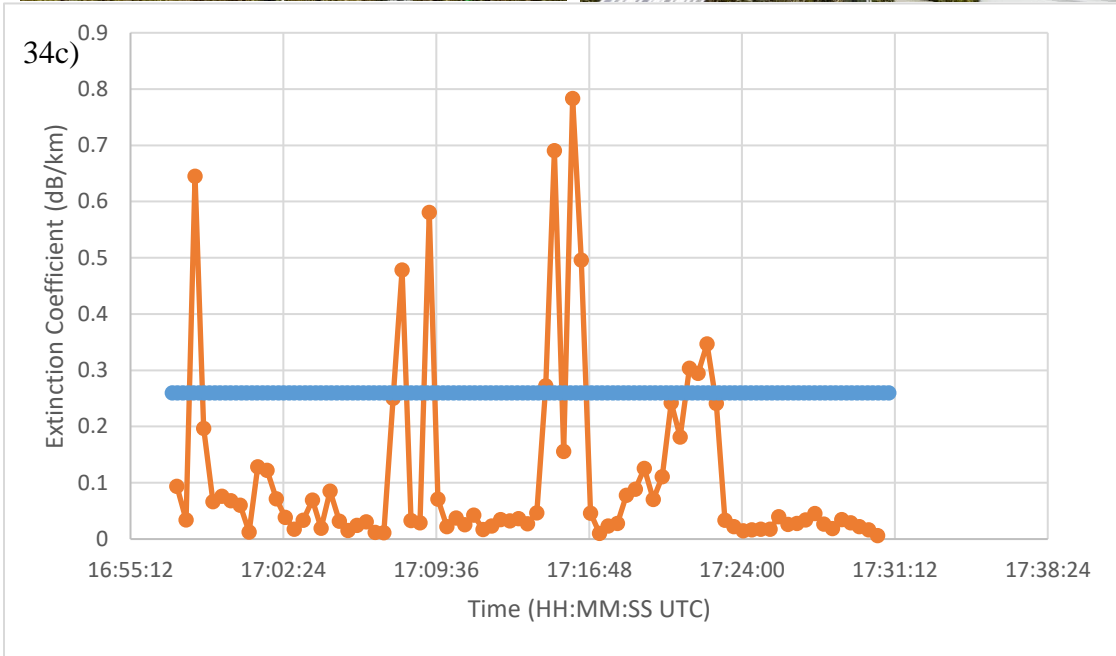
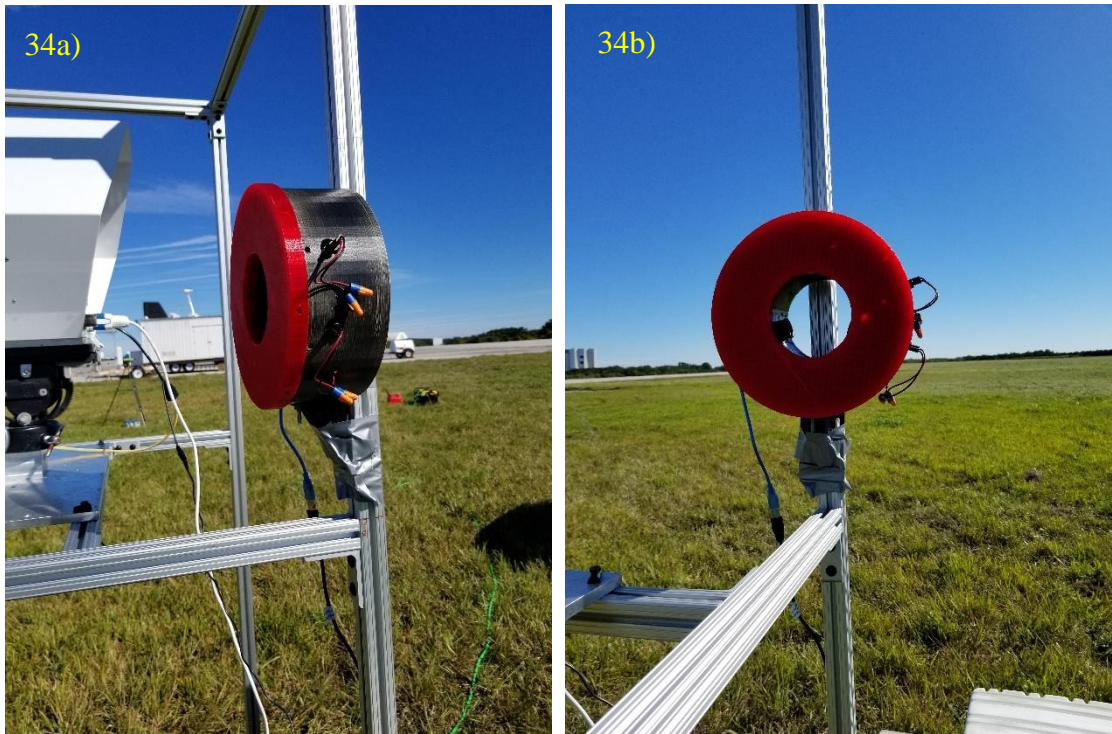


Figure 34: Original design of the 2ml FSM mounted next to the MOG transmissometer (31a-b). First runs of data obtained on December 5th, 2018 starting at 11:55 pm ending at 12:30 pm.

Another issue that is of intrinsic nature of FSM's is the visibility limit in clear weather. A Vaisala FD12P visibility meter, owned by UCF, was placed measuring visibilities of >50km on December 5th, 2018. This can be seen in figure 34c where the

Vaisala extinction coefficient in dB/km is saturated at its limit of 0.26 dB/km or 50 km visibility limit. This leads to the question of the 2 ml FSM design picking up aerosol scattering on a clear day. If the Vaisala FD12P is reaching its upper visibility limit then most likely the 2 ml detector is too. The FD12P has a sampling volume of 0.1 L which is 50 times larger than the 2 ml detector meaning the 2 ml FSM will not detect many aerosols. This is why the baseline extinction coefficient in figure 34c is running below 0.1 dB/km the scattering signal is too small and the data is just baseline noise. The functions are artifacts of incorrect signal processing. The data processing is not correct because the signal was sampled at ~9Hz which is not satisfactory for sampling a 10Hz signal. The first iteration of the 2 ml FSM used an Arduino as the ADC which could not sample the signal fast enough due to the communication time with the code on a PC. The averaging technique originally took an average over one minute of data but did not use a running window. The code and averaging technique are not discussed due to them being changed quickly into the project. To fix these issues a new ADC is considered along with a larger sampling volume.

Although the trip's FSM experiments did not come back with convincing visibility measurements, the trip was a first field test that bettered the future FSM designs along with long term outside use. The small circular device worked well outside and protected the electronics well. The casing of the 2 ml FSM, mounted on 8020 metal frames in figure 34, was knocked over by a fire truck water cannon and all electronics inside were safe after the event. This unexpected stress test meant the device could possibly be safe in adverse weather conditions for a short period of time.

6.2 Florida February 2019: 2ml FSM

A second field test was conducted at UCF's TISTEF range between the dates of February 18th to 22nd, 2019- with an updated design of the 2 ml FSM. The range includes a 1 km grass field whereas the SLF is an asphalt range of 5 km which is not considered a variable in visibility measurements. The updates included bandpass filters, a better data collection system using a Raspberry PI with an ADS1256 24-bit ADC, and updated signal processing procedure.



Figure 35: Setup on the morning of February 19th at UCF's TISTEF range alongside a Vaisala visibility meter. In the background it can be seen that there is a bit of cloud formation.

The second day of data collection returned a good comparison to the Vaisala visibility meter shown in figure 35. The data collection started around 9:30 am EST (14:30 UTC) and went on for two hours. Within this data collection period, the Vaisala measured extinction coefficients, between 0.5 – 0.8 dB/km (see figure 36a), that correspond to 20 km visibility. The FSM recorded similar values but then dropped off sharply around 11 am (16:00 UTC) which is believed to be an issue with the FSM. This is attributed to either misalignment of the laser, contamination of the lenses, or a clump of aerosols.

The inconsistent measurement shown in figure 36 could first be from the laser becoming misaligned in the 2 ml setup which is a possibility due to the lacking of strong support for the optical tube. If the laser comes misaligned the scattering volume will not be aligned with the scattering channel aperture leading to much of the scattered light not hitting the detector. The second source of error is the lens building up condensation in the presence of aerosols. Although the day itself is rather clear, in background of figure 32, condensation cannot be ruled out as it caused major issues in later experiments. The last and also, most prominent source of error is due to the small sampling volume. The small sampling volume of, 2 ml, is thought to be why the signal drops around 15:50:24 in figure 36a.

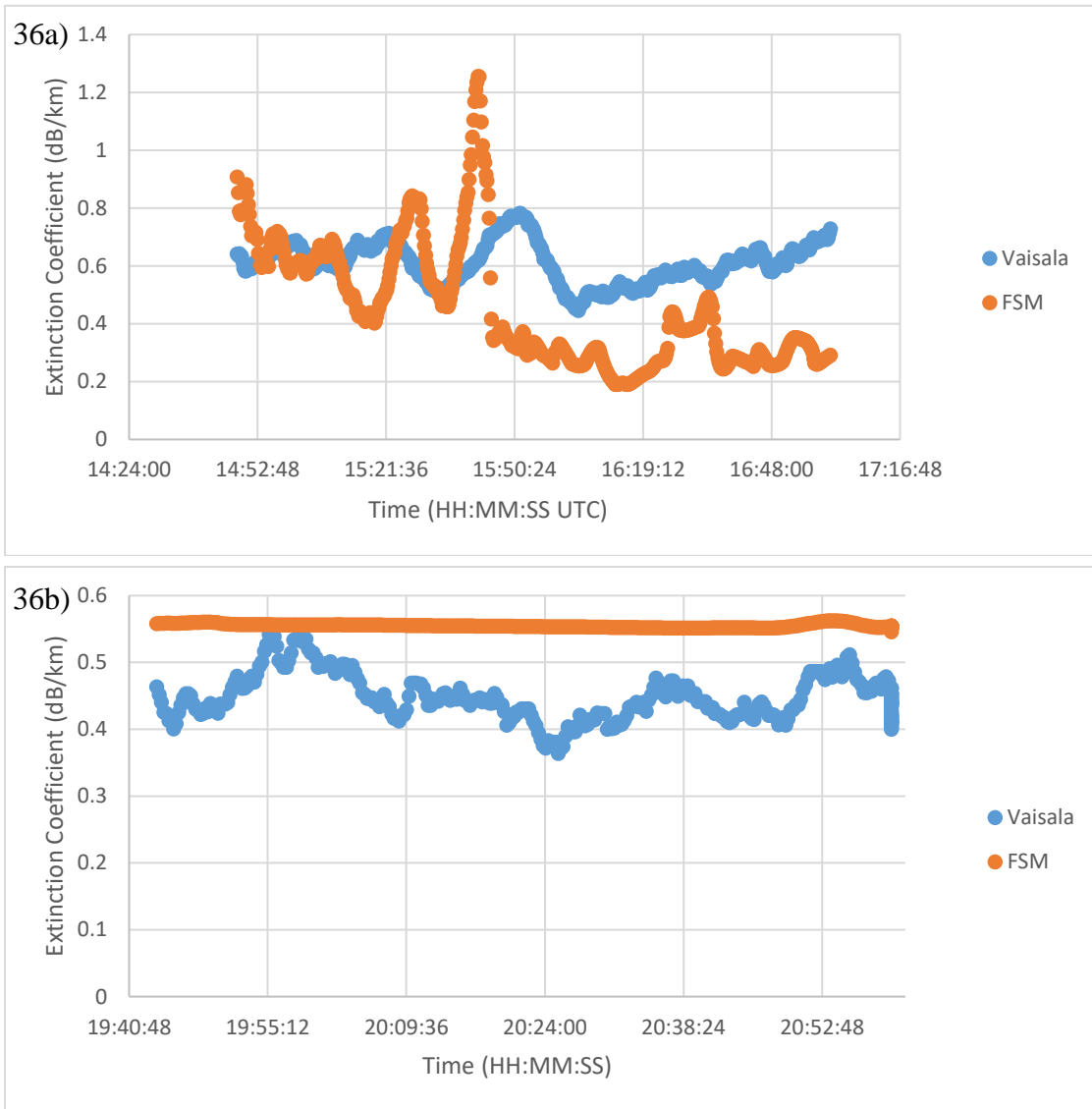


Figure 36: Comparison of the Vaisala to the 2ml FSM over a period of roughly 2 hours on the morning of February 19th, 2019 starting at 9:30am.

Although this experiment has sources of error that must be addressed the results of these experiments confirmed the calibration, data processing, and data acquisition techniques used to determine visibility. This experiment was successful at confirming that the first issue to address is redesigning the mechanical design to increase the scattering volume so that the visibility measurements will be more representative of the surrounding atmosphere. The visibility measurements shown in figure 33a determine

that the 2ml FSM works in a setting where there are a large number of aerosols in the air, but during clear conditions, when small numbers of aerosols are present, the meter does not receive enough scattered light to determine the real-time visibility. This conclusion was also reached during later data runs during the trip where the weather became clearer and the 2 ml FSM performed poorly compared to the Vaisala since the scattering signal could not be measured. This poor comparison can be seen in figure 36b where the 2 ml FSM is not detecting the scattering signal. This is thought to be due to the detectors only sensing the background light and no scattered signal meaning the scattered signal is too weak to detect compared to the background. This is thought to be, once again, due to small sampling volume because the scattering signal is so weak. But due to the scattering signal being weak also points to not enough sensitivity on the scattering channel TIA. To fix the sensitivity on the TIA the feedback resistor could be changed from 10 M Ω to 15M Ω or 20M Ω but the tradeoff would be decreasing the capacity for noise.

6.3 Qualitative Humidifier Experiment

After the experiments in Florida, it was concluded that a larger sampling volume would fix signal problems in high visibility along with aerosol clumps. The 2 ml design calibration and measurements were deemed reasonable from the previous section 6.2 so a comparison was done between the first and second design using a Crane ultrasonic cool mist humidifier. The experimental goal is to test if the 150 ml FSM is measuring extinction coefficients on the same order of magnitude of the 2 ml FSM. This is supported by the fact the 2ml FSM measured the correct order of magnitude and

in reasonable agreement with the Vaisala visibility meter from the previous Florida trip.

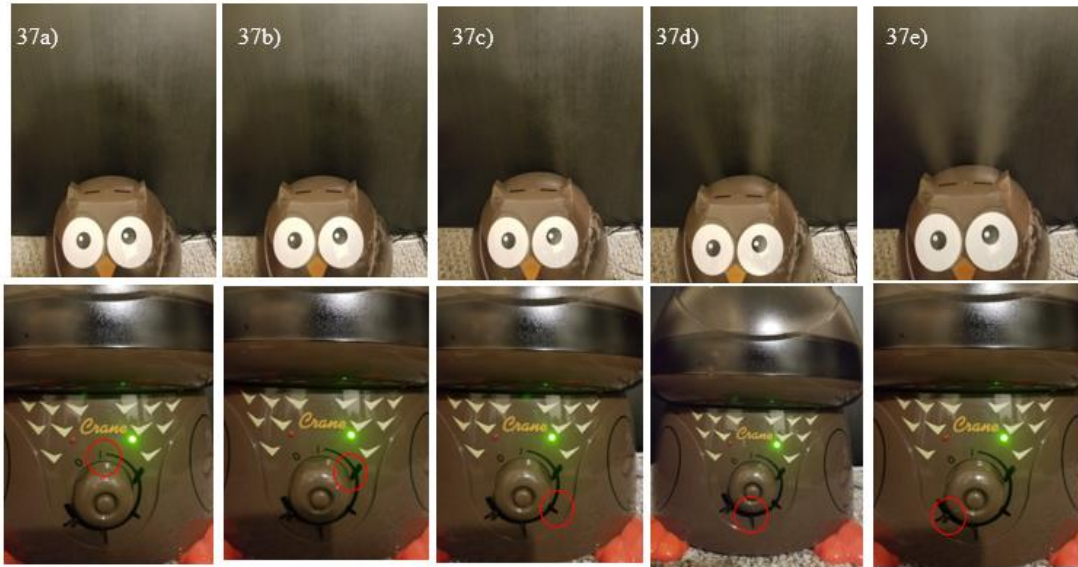


Figure 37: Four standards of measure starting with 37b as pre-set 1 and 37e as pre-set 4. The top shows the aerosol generation whereas the bottom shows the knob preset for each.

The humidifier does not come with pre-allocated settings or discussion on the number of aerosols produced. To qualitatively compare the extinction coefficients measured four settings were chosen as shown in figure 37 that will be the standards of measure. In the bottom picture for each figure, in figure 37, the dial is turned to one of 4 pre-set tick marks circled in red. A fan was also used to blow the aerosols through each design's respective sampling volume to prevent aerosol clumping and generate a more uniform aerosol distribution. The first set of data, figure 38a, is from changing the setting from pre-set 1 to pre-set 4 after a period of 30 minutes. The second set of data, figure 38b, is changing the pre-set from 4 to 3 to 2 to 1 in increments of 15 minutes. The red lines in figures 38a and 38b represent when the knob is changed settings.

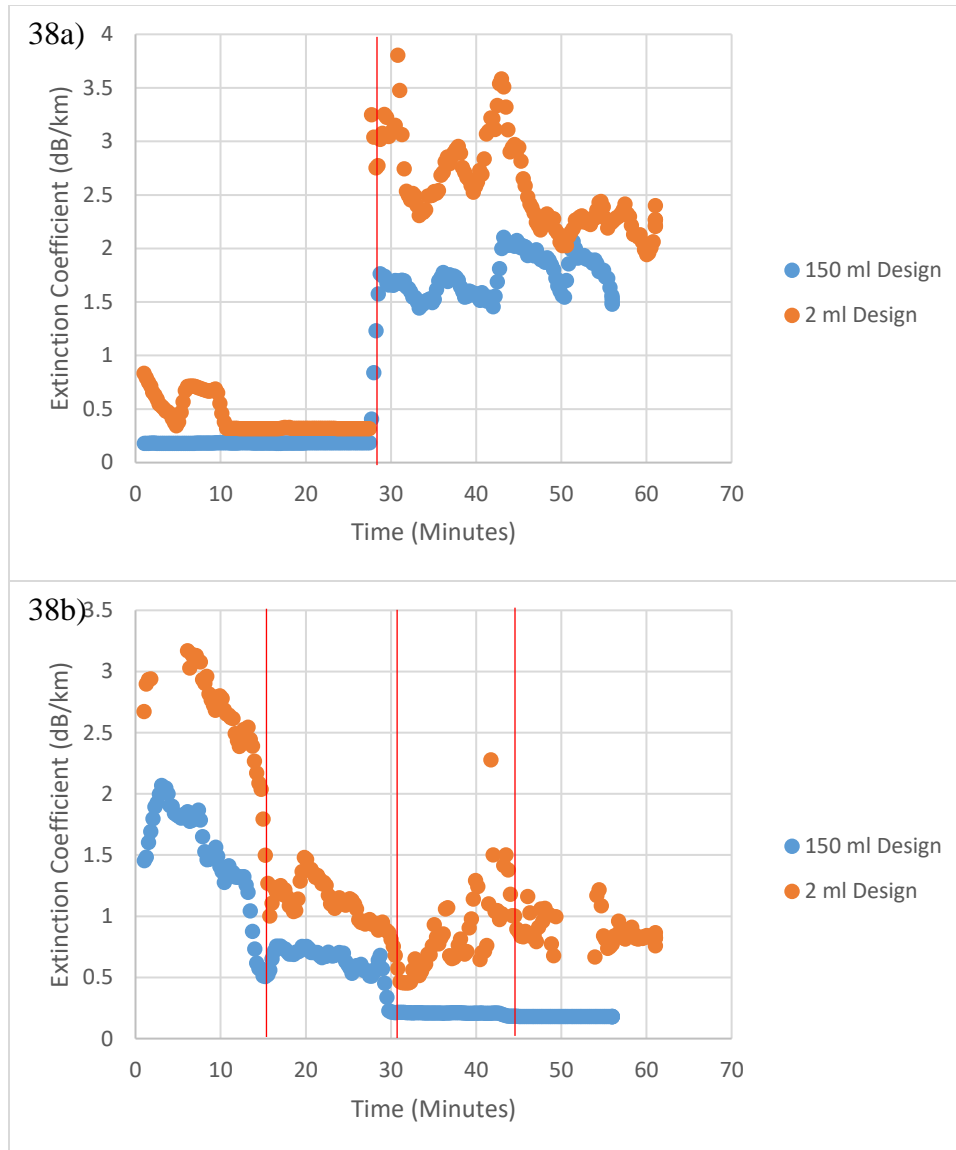


Figure 38: The top graph (35a) is of changing the humidifier from pre-set 1 to pre-set 4 after 30 minutes. The bottom graph (35b) is changing the pre-set from 4-3-2-1 in intervals of 15 minutes represented by each red line.

In both figure 38a and 38b when the knob is turned to a different preset aerosol level the extinction coefficient also changes which is shown at each red line on figure 38. When the knob is set at setting 3 and 4 there are more aerosols present that at setting 1 and 2. The graph is showing what extinction the 2 ml ad 150 ml FSMs are measuring after being calibrated. The difference in measurement when the humidifier is pre-set to 3 or 4 can be attributed to the sampling volume. Electronic sensitivity is ruled out because the same light source and photodetectors are used in each design for this

experiment. It is noted that the 2 ml FSM still works reasonably well when enough aerosols are put into the sampling volume. The large differences in figure 38b between 30 – 60 minutes are attributed to condensation building on the 2 ml FSM lenses since after the measurement a lot of water was present in the PLA case and optical tubes.

The main takeaway is that the calibration procedure of the 150ml FSM design is on the same order of magnitude as the 2 ml design which was compared to the Vaisala. This comparison was successful at verifying the calibration technique for the 150ml design which will be used in the next few experiments.

6.4 Fog Chamber

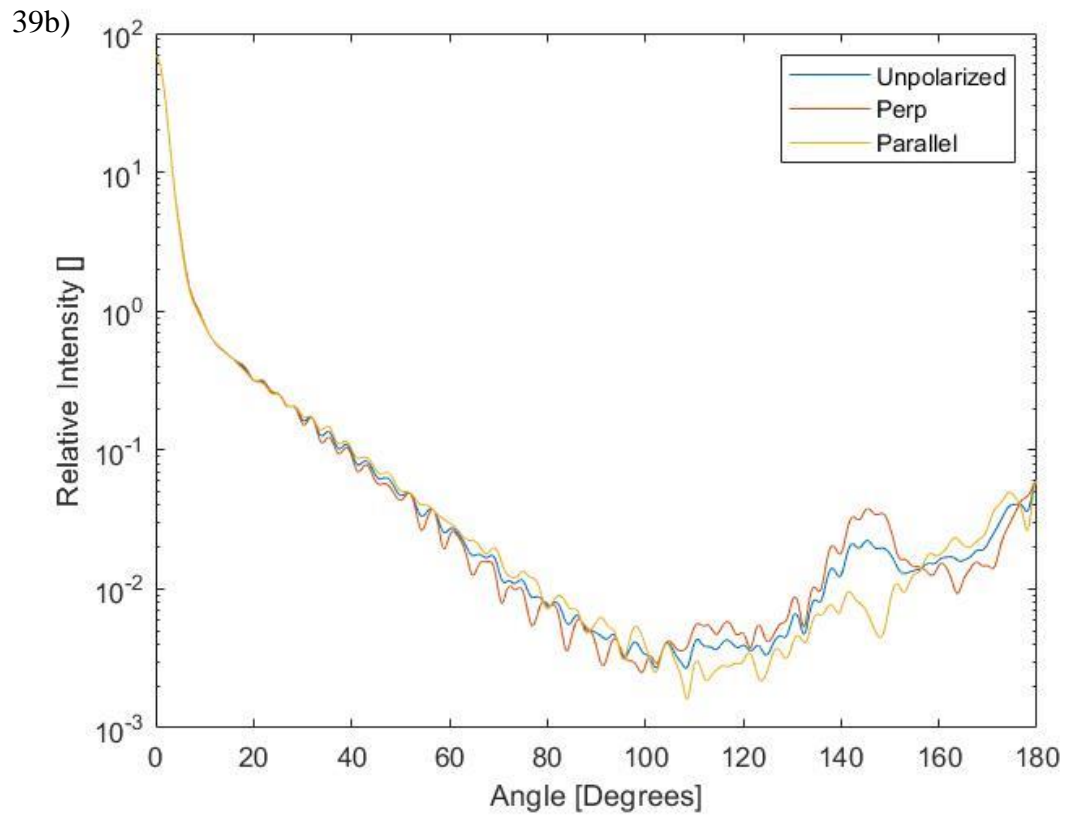
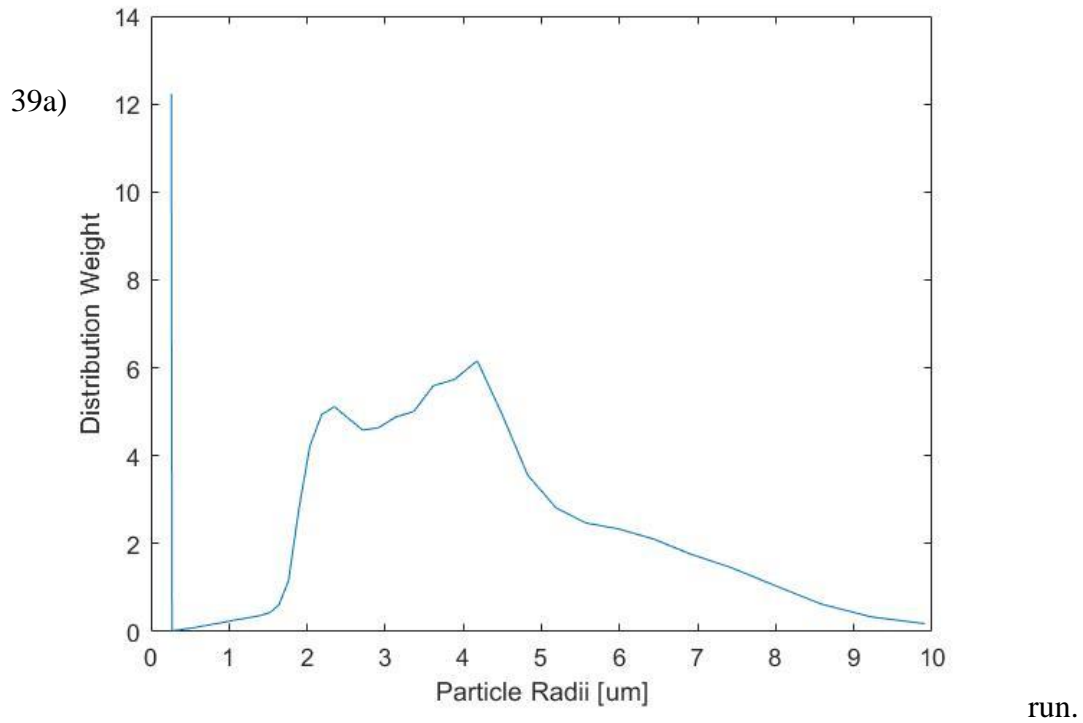
The next experiments are done inside of a 2.5m x 2.5m x 1.5m fog chamber provided by the Naval Research Lab (NRL) in Washington DC. The fog chamber is meant to produce and simulate haze to heavy fog conditions originally for spectral attenuation through fog from an idealized blackbody source. In this thesis the 150 ml FSM will be placed inside the fog chamber to measure the fog extinction. The experimental goal is to see if the visibility meter can measure different fog conditions, especially heavy fog, due to the difficulties of finding consistent fog outside the lab.

The fog machine used is a FOGCO misting pump with various nozzle sizes, the nozzle size is not specified so it is assumed to be the 0.008-inch diameter nozzle.

6.4.1 Fog Chamber Distribution Spectra

The fog machine had previously been characterized by NRL using an aerodynamic particle sizer spectrometer 331 from TSI incorporated for various nozzle sizes. The particle distribution for the 0.008-inch nozzle, figure 39a, has the same bimodal distribution shape as the other nozzles but with varying concentrations due to

the variance of the fog produced every data



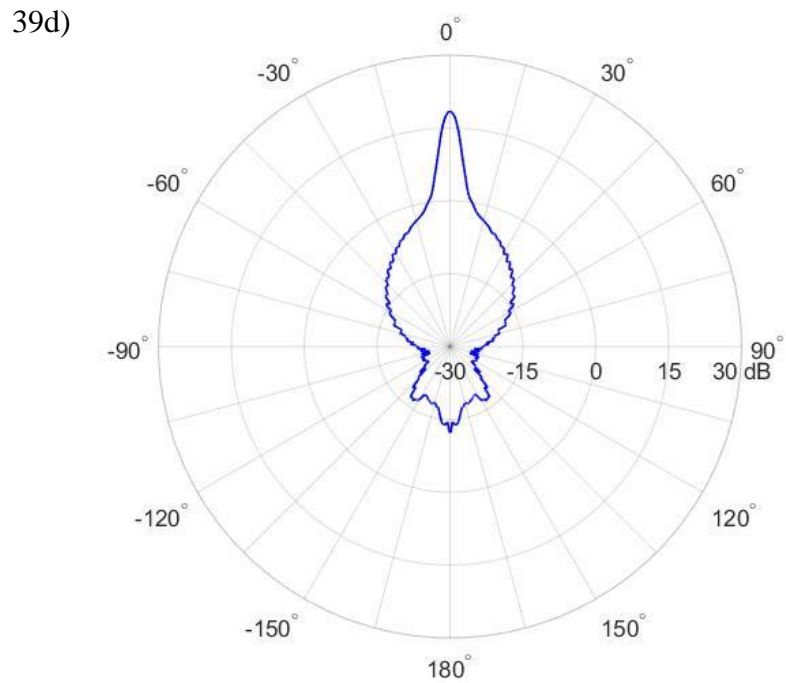
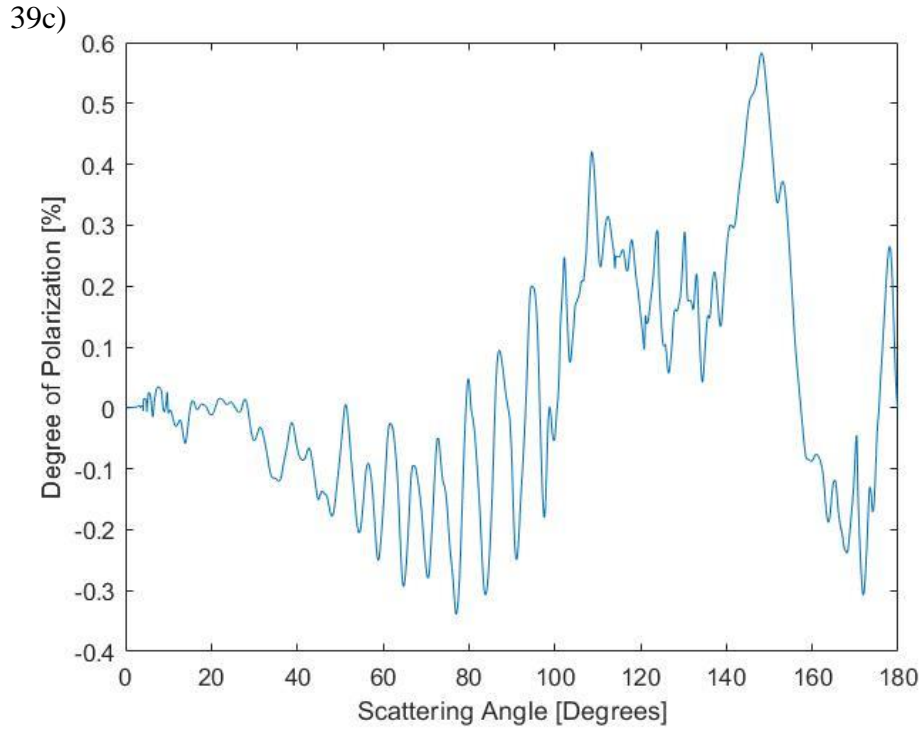


Figure 39: Characterization of the fog chamber where 39a is the general shape of the particle distribution created by the FOGCO. (39b-d) characterize the angular dependent scattering through the fog chamber.

The distribution in figure 39a has a sharp peak, greater than 12 seen to the far left of the graph, at a particle radius of $0.273 \mu\text{m}$ due to the particle spectrometer binning all particles smaller than this radius into the same bin. The phase function in

figure 36b is seen to have a lot of structure at all angles which is a consequence of the binning of the particle distribution. The particle spectrometer coarsely placed particles into 54 bins based on radii ranges which makes for a discrete particle distribution compared to the distributions in the previous chapter.

To estimate the extinction of the fog Mie theory was applied to the distribution in figure 39a. The distribution was normalized to a total particle density of 100 particles/cm³ to stay consistent with the previous chapters. The extinction coefficient, $\sigma_{km^{-1}}$, was calculated to be 9.66 km⁻¹ and in decibels as 41.9 dB/km. This number is used to estimate what conditions will be replicated in the fog chamber for thick fog and to see if this can be measured experimentally by the 150 ml FSM.

6.4.2 Fog Chamber Experiment

Various fog chamber data runs were made between the dates of March 18th to March 22nd, 2019 to determine the 150 ml FSM performance in haze to thick fog conditions. The fog chamber was setup in a personal garage due to limited space at the University of Maryland. The device consisted of a metal frame with plexiglass windows (figure 40a), the FOGCO fog pump, and a small water pump (figure 40b). A note about the fog chamber, as seen in figures 40c-d, is the fog distribution is not uniform in the chamber even after letting the machine run for an hour to fill the chamber and taping all edges and holes. The chamber also produces a large amount of water and condensation so the water-resistant design of the 150ml FSM will hold up in these conditions compared to the 2ml FSM.

The fog quickly dissipates, as will be shown in experimental data, away from the nozzles meaning the fog near the nozzles is thicker than the fog away from the

nozzles. Both conditions were tested to see their visibility conditions. The first experiment had the 150 ml FSM placed away from the nozzles as seen in figure 40d.



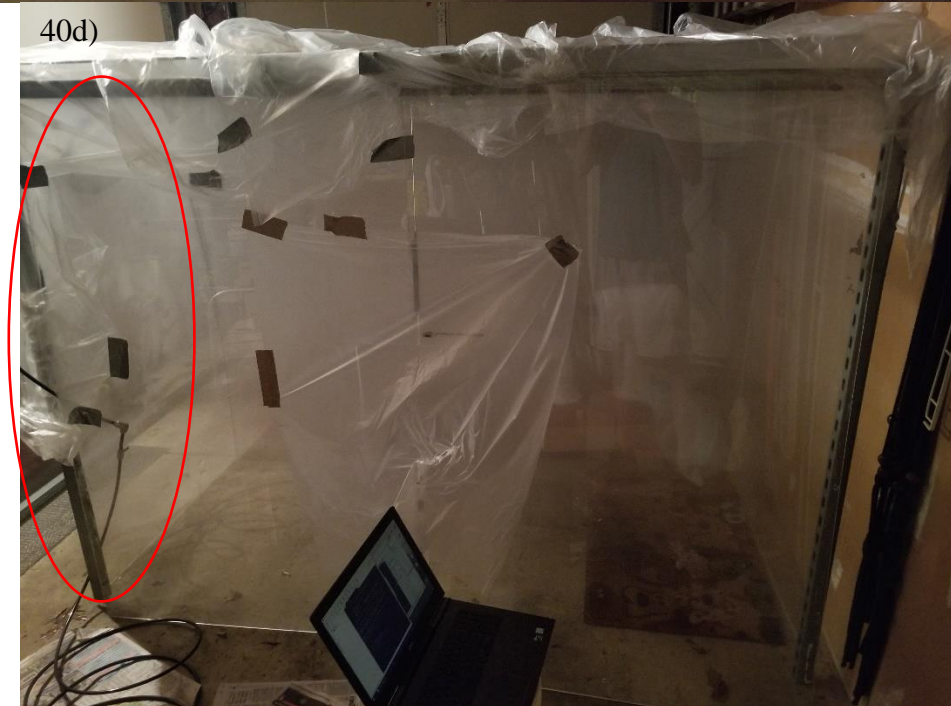


Figure 40: Experimental setup and fog recorded on March 18th, 2019. 40a is when the fog chamber started to fill up. 40b is the FOGCO fog machine. 40c is the first test of the 150 ml FSM and 40d highlights where the nozzles are placed in the chamber.

Before the first run the FOGCO was turned on for about an hour meaning there is already a lot of background aerosols in the garage that will add to the background at the start. This effect is not noticeable in this run due to the start time of the FOGCO being turned on before the RP started data logging. In the back of the chamber, it can be seen that the fog levels reach max extinction of 20 dB/km in figure 38 a where the visibility reaches a minimum of 610 meters falling in the range of light to moderate fog. Given the conditions in the back of the chamber where the fog is starting to dissipate and the pictures of the fog in figure 40, the visibility and extinction are considered reasonable. The next thing to note is the relaxation time of the fog to return

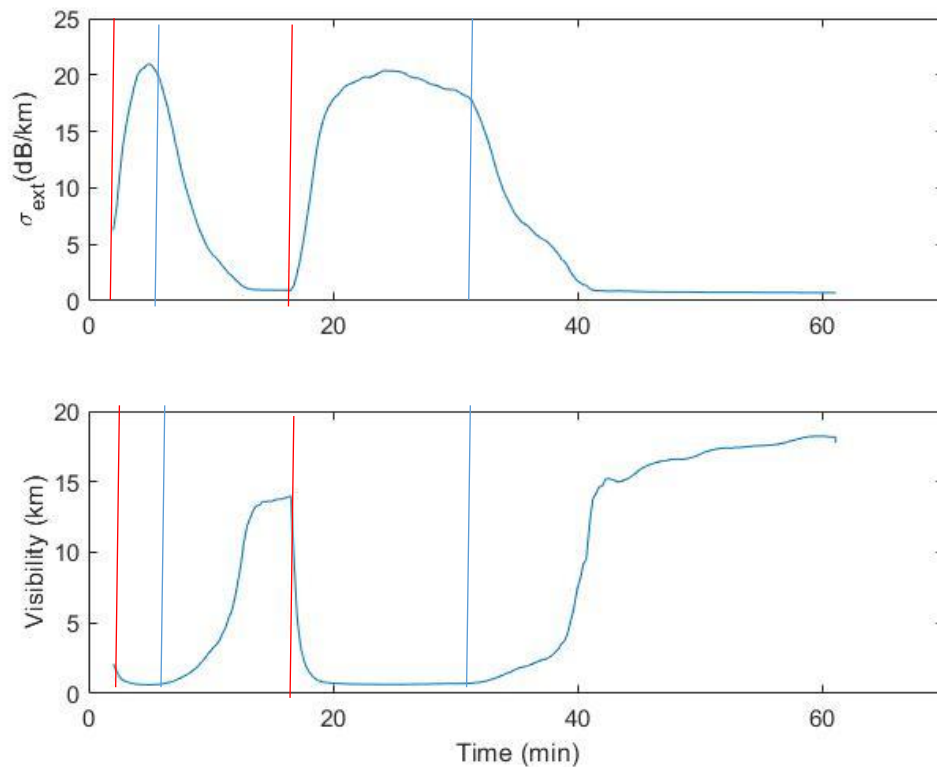


Figure 41: Data for March 18th, 2019 in the back of the fog chamber furthest away from the nozzles. The FOGCO is turned on at the red lines and turned off at the blue lines on figure 38. Extinction in dB/km versus time on top and visibility versus time on the bottom.

to the background the first peak takes about 7 minutes to relax whereas the second peak

takes about 9 minutes. The fog is quick to disperse once the source is turned off due to leak and not a perfect seal around the entirety of the chamber.

The second experiment was placing the 150 ml FSM in the center of the chamber closer to the source nozzles. The setup is shown in figures 42a and 42b with a black target seen through the center of the scattering volume. The data collected is surprising that the fog content in the center of the chamber is less than noticed at the edge of the chamber along with a decreasing trend in the fog. This is attributed to condensation building on the lenses which was not noticeable in the first measurements due to the distance away from the nozzles. This data is important to note the issue of condensation that limits the 150 ml FSM in fog and precipitation. The max extinction measured this data run, shown in figure 43, is 15 dB/km with a minimum visibility of 850 meters falling into the category of light fog. A black target is used to gauge how thick the fog is qualitatively by looking at the contrast of the black and white. In figure 39 the contrast of the black target is seen to decrease significantly when fog fills the chamber meaning that the visibility also decreased in the fog presence,

It is important to note that the steady decrease in extinction is possible from power drift, movement of fog nozzles, decrease in fog production from loss of water, along with the lens condensation.

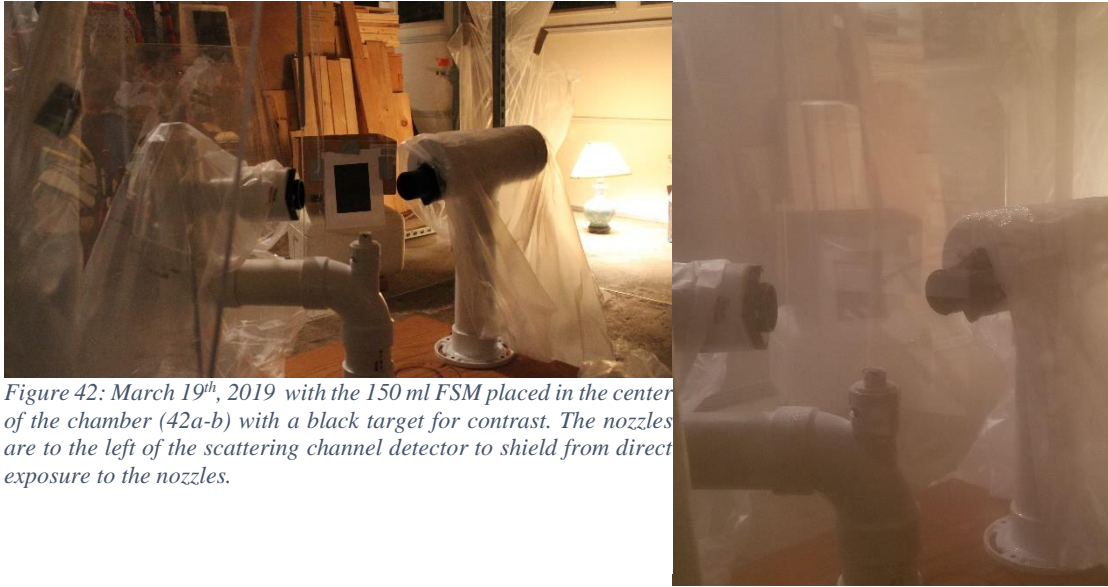


Figure 42: March 19th, 2019 with the 150 ml FSM placed in the center of the chamber (42a-b) with a black target for contrast. The nozzles are to the left of the scattering channel detector to shield from direct exposure to the nozzles.

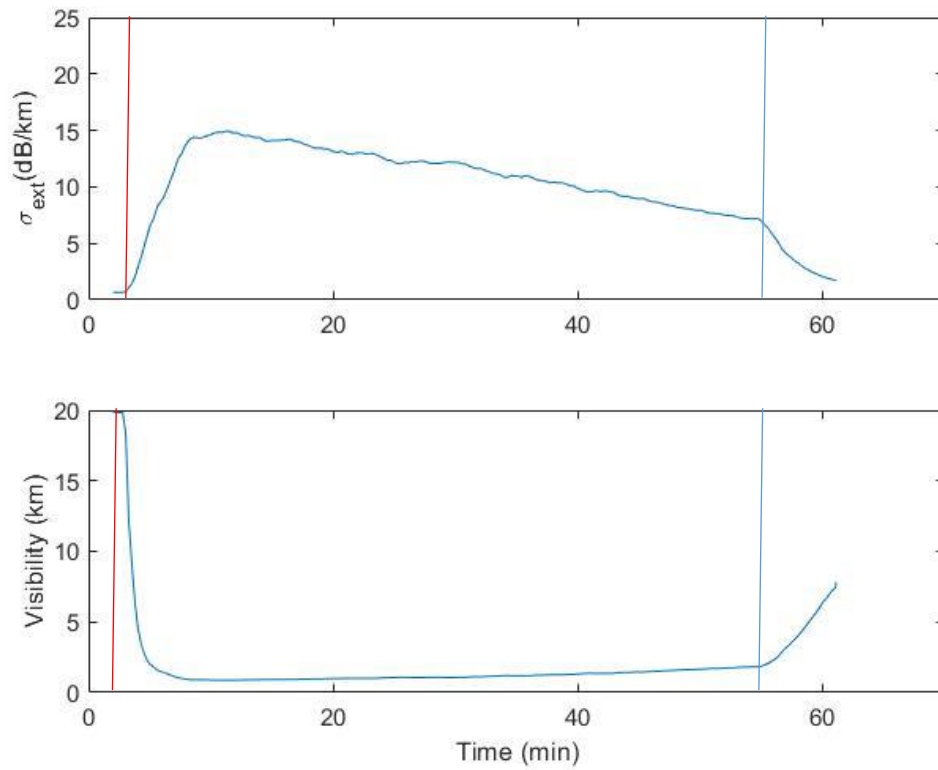


Figure 43: Data runs on March 19th, 2019 with the 150 ml FSM placed in the center of the fog chamber. The red lines are when the FOGCO is turned on and blue lines are when the FOGCO is turned off.

The last fog chamber experiment is placing the 150 ml FSM directly in the path of the nozzles. This is expected to give the largest extinction since the fog has not dissipated at all closest to the nozzles. Figure 44 is a time-lapse using a Canon EOS 60D DSLR camera recording at a resolution of 1280x720 for 20 minutes when the FOGCO is initially turned on. The black target is placed at the center of the scattering volume 2 meters away from the camera. Over a period of ~8 minutes, the scattering volume can be seen to fill with a thick layer of fog quickly.



Figure 44: Frames saved from a video showing the change in the fog level over the first 25 minutes of data collection. This was taken on March 20th, 2019.

The frames in figure 44 correspond to the large extinction measured at the start of the data run in figure 45. In figure 45 the data peaks with extinction of 46.68 dB/km

and minimum visibility of 280m corresponding to moderate and thick fog. As the measurement continues for 2 hours with the FOGCO running continuously the aerosol extinction can be seen to drop and the visibility increases. The extinction coefficient represents light to moderate fog, as described in figure 7, averaging around extinction of 25 dB/km from 25 to 50 minutes and 8 dB/km from 50 to 110 minutes. The decrease in extinction coefficient is attributed to condensation building up on the lenses along with the movement of the fog nozzles as time goes on.

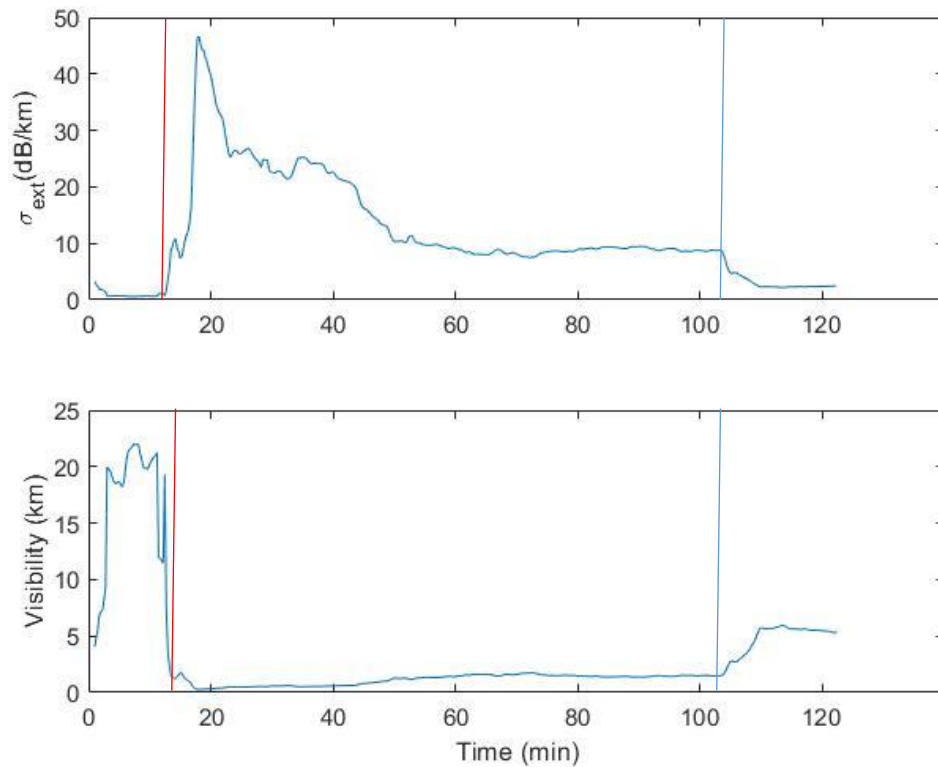


Figure 45: Largest fog extinction measured around the 20-minute mark when the 150ml FSM is placed directly in the path of the nozzles. Extinction in dB/km vs. time on top and visibility versus time on the bottom.

6.5 Outside testing: Design 2



Figure 46: Outside placement of the 150 ml FSM on the clear day of March 19th, 2019.

The third experiment was to place the 150ml FSM outside in clear weather as seen in figure 46. The device is placed 1.5 m above the ground from WMO guidelines on visibility measurements. Figure 47 displays the data recorded as being a clear day due to visibility measurements being above 50km with a strong falloff of signal later on after 90 minutes of data acquisition. The outside testing of the 150 ml FSM in clear weather is important due to this weather condition being one of two extremum operating conditions. The 150 ml FSM performs poorly in clear weather conditions just as the 2 ml FSM due to the small number of aerosols in the sampling volume. The scattering signal becomes comparable to the noise levels of the detector making it difficult to extract the scattering signal. The 150ml FSM is also susceptible to the background sunlight due to the saturation of the detector to the 5 V rail. To help block much of the light directly entering the aperture a board is placed directly in front of the

detector as shown below in figure 46. This board disrupts air flow but must be used to block the background light.

Originally the saturation issue in the 2 ml FSM was taken care of by using an $0.850\ \mu\text{m}$ bandpass filter which is also used on the 150ml FSM design. The filter does not block enough background light due to the larger light collection aperture. Even with a cylindrical baffle to block light coming from most extreme angles too much light comes into the aperture directly.

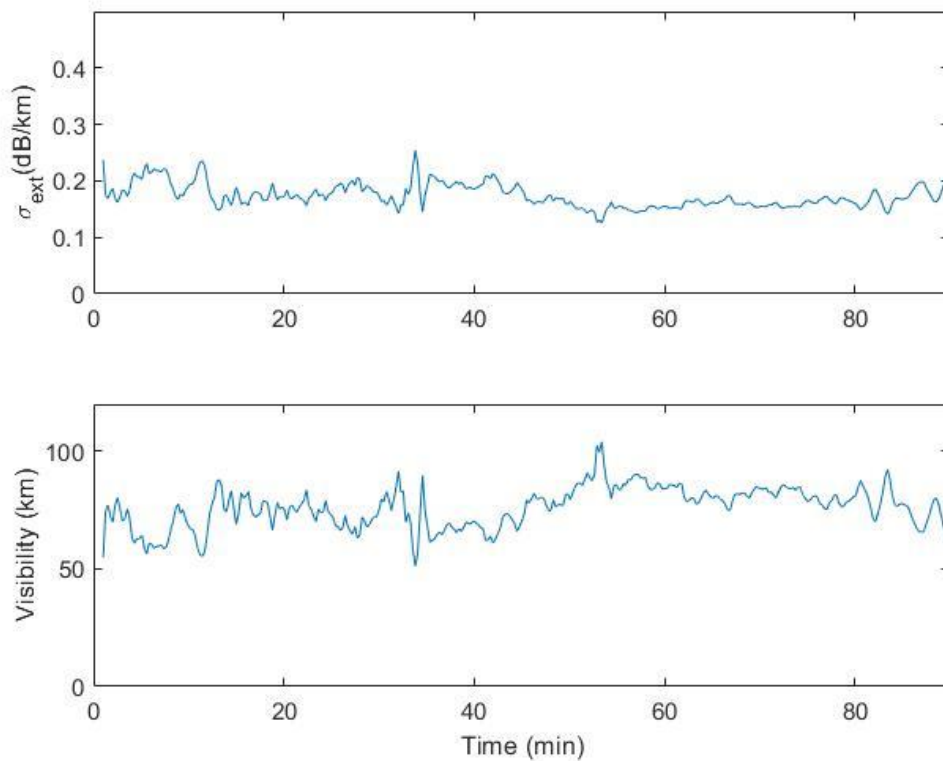


Figure 47: Data runs on March 19th in clear weather with extinction in dB/km versus time on top and visibility vs. time on the bottom.

The second outdoor test of the 150 ml FSM is performed during moderate to heavy rain on the afternoon of March 21st, 2019 to test the durability and also the performance in precipitation. In the overcast and rain, a board is still placed in front of

the detector in the event of saturation due to background sunlight. The data recorded in figure 48 shows the effect of saturation on the extinction and visibility measurements since most of the data is cut off except between 60-80 minutes and 105-120 minutes. The cut off data is due to the voltage being the maximum of 5 V and no possibility of recovering the scattered light. The data seen in figure 45 is when the saturation stopped and the scattering signal could be recovered. The data recovered shows an average extinction of 4 dB/km with corresponding visibility of 2 to 6 km which is the expected visibility in light to heavy rain [19]. Although the data shows a large variation in the rain the 150 ml FSM did not include rainy conditions in the original design along with no intention of it working correctly in the rain due to the scattering effects of large particles such as water droplets.

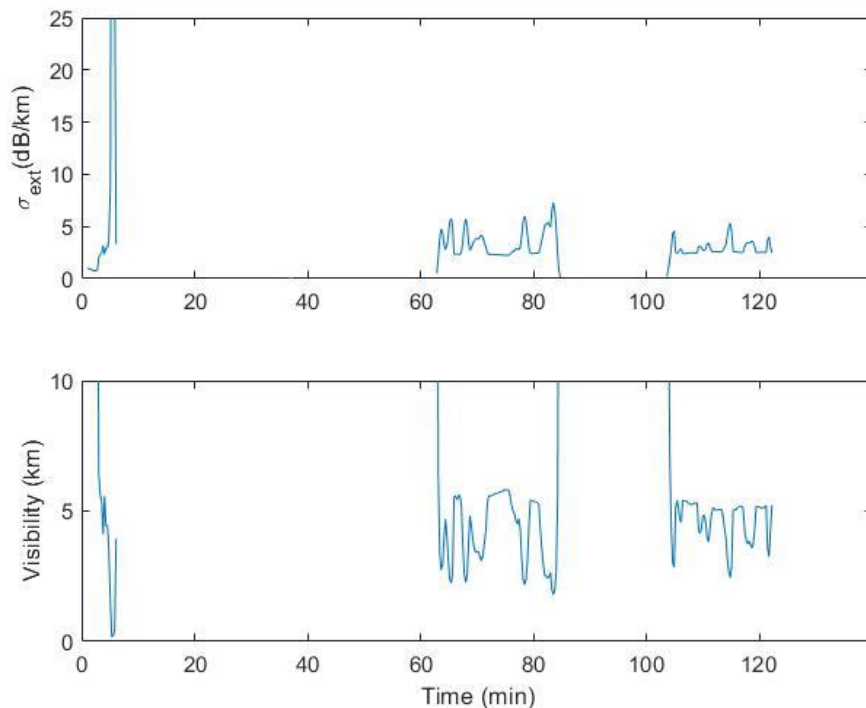


Figure 48: Data recorded on March 21st during light to heavy rain with overcast with plots of extinction in dB/km vs. time (top) and visibility versus time (bottom)

The outdoor tests provided evidence of outside the lab environment proof of concept of the 150 ml FSM. Although a makeshift solution to unsaturated the scattering detectors is used the 150 ml FSM still provided reasonable data for each test. The fog chamber experiments and outside experiments provided a wide range of operating conditions for the 150 ml FSM to record data in.

Chapter 7: Discussion

The discussion of this project will entail the explanations for various error that appeared in the 2 ml and 150 ml FSM designs and their solutions or proposed solutions. Along with proposed experimental ideas that could better quantify the operation of the proposed FSM in this thesis along with future directions of quantifying aerosol scattering properties.

7.1 Experimental Results

After performing the experiments described in chapter 6, the FSM proposed to measure visibility has been drastically improved since the first design taken to Florida in December 2018. There have been various problems along the way along and problems still in the current designs of the 2 ml and 150 ml FSMs. The problems lie in the dynamical range of the instruments and scattering volume. The main operating characteristics, determined experimentally and theoretically, of the lab-built FSM's are placed alongside the commercial meters mentioned in this paper in table 12. One huge benefit of the 2 ml and 150 ml designs is that they are significantly cheaper than the commercial visibility meters while providing the same range of visibility measurements. To make this conclusion true more thorough tests and experimental confirmation must be done.

Maker	Type	Range (km)	λ (nm)	Angle (°)	Pulse Rate (kHz)	Sample Volume (L)	Cost (Thousand Dollars)
CS	CS120A	0.01-75	850 LED	42°	1	-	4-6
Vaisala	FD12P	0.01-50	875 LED	33°	2.3	0.1	31
Vaisala	PWD22	0.01-20	875 LED	45°	2	0.1	10.3
RMYC	7300	0.03-16	850 LED	42°	-	-	8-10
-	2 ml	0.15-50	850 Laser	35°	0.01	0.002	0.73
-	150 ml	0.1-60	850 Laser	38°	0.01	0.150	1.02

Table 12: Reference table back to the original commercial meter specifications compared to the lab build FSM's

7.1.1 2ml FSM Intrinsic Problems and Solutions

The first design of the 2 ml FSM had issues during the first field test in Florida from December 2nd-7th, 2018. The scattering detector quickly saturated due to using a short pass glass filter and not a bandpass filter at 0.850 μm . The saturation was fixed by using the correct bandpass filter in the second iteration of the 2ml FSM.

The second issue was the pickup of electromagnetic interference (EMI) at 60Hz on the scattering channel. The amplifier has a large gain of $\sim 10^6$ which amplifies any significant noise in the signal wires from the photodetector to the amplifier. To solve this issue the wires from the scattering detector were shortened along with making PCBs. The problem is still pertinent if next to live power cables or a generator.

The 2 ml FSM design maintains the main problems of waterproofing and small scattering volume. The small scattering volume hinders its performance in high visibility conditions along with incorrectly sampling the air due to its small sample of the surrounding, assumed to be homogenous, atmosphere. The meter will perform best when in low visibility conditions when the sampling volume can be totally immersed

in aerosols. The design of the 2 ml FSM, is also not water-proof thus making this device not suitable to work in rainy conditions.

Due to the experimental evidence and static mechanical design of the 2 ml FSM this design will no longer be followed but will be tested when conditions are very foggy to determine if the smaller sampling volume is still relevant in visibility measurements.

7.1.2 150ml FSM Intrinsic Problems and Solutions

The first problem with the 150 ml FSM is the illumination of the larger sampling volume. An aperture is placed in front of the collimated laser diode to get the most circular beam shape and then a 220-grit diffuser is placed after the aperture to evenly illuminate the scattering volume. The diffuser redistributes the, assumed to be Gaussian, laser power profile to the whole volume which in turn should have no effect on the scattered light. In the experiments, the diffuser is kept on at all times and works properly to illuminate the whole volume but it would be more effective to expand the main beam itself and not use the diffuser. In this case, the beam is highly elliptical so it was deemed ineffective to expand the beam and the diffuser was used. In another iteration of the 150 ml FSM the beam will be expanded and no diffuser will be used to test this design.

The second problem with the 150 ml design is background light being received in the scattering channel saturating the detector even with neutral density filters attached. This means that the sunlight is not entirely being blocked by the bandpass filters at $0.850 \mu\text{m}$. When the 2ml design was placed directly into the sun the detectors would have increased background so a cylindrical baffle to block direct sunlight was considered to be enough. To solve this issue a complex baffle system will have to be

devised to block the light since a simple cylindrical baffle does not block all the light entering the system.

The third problem of the 150 ml FSM is condensation forming on the lenses in precipitative and foggy conditions. The first solution to this problem is to add back a reference channel for the monitoring of laser power through the transmitter lens. This procedure is mentioned in [35] for the same reason, condensation. When condensation occurs on the transmitter lens light is scattered and refracted away from the scattering volume decreasing the amount of light reaching the scattering detector. To help normalize this issue a reference channel can be used in a feedback loop to vary the current the light source receives to either increase or decrease the laser power to make up for the condensation. To solve the condensation problem in a much simpler manner lens heaters can be installed on either side of the transmitter and receiver lenses. This will keep condensation from forming in adverse weather conditions. All four of the commercial visibility meters mentioned in the introduction solve the condensation problem by installing heated optics.

The three previously mentioned problems were determined from the experiments described in chapter 6 and the solutions mentioned above will be put into the next iteration of the 150 ml FSM. One note is that, even with the new 150 ml FSM, the particle density of the particle distribution in the scattering volume can still not be found. To obtain this measurement an FSM must be used in conjunction with a particle counter. No other information can be extracted from the particle distribution since more angles of scattering light must be known in order to rebuild the scattering phase

function. Even if the scattering phase function can be measured there is not a unique particle distribution to produce it.

Overall the design of the 150 ml FSM worked well but as a qualitative conclusion, the fog is underestimated for all measurements. This is due to how dense the fog is in images compared to the data. This is the case for figure 39 and 41c since the black target is seen to have much lower contrast between the white and black meaning the visibility is low. The visibility, at most output an extinction coefficient of 46 dB/km corresponding to moderate fog but visually it looks like shown fog as shown in table 8. This issue will be solved by working out a finer balance between the neutral density filters, calibration, TIA gain, sampling volume size, and how the sample volume is illuminated. By optimizing these parameters the visibility measurement can be made to be more accurate in foggy conditions. In foggy conditions, the wavelength dependence of visibility, described in chapter two, also plays a small role in the visibility being incorrect for fog in the fog chamber experiments.

7.2 Future Work

7.2.1 Multi-Wavelength Forward Scattering Meter

Mentioned in section 2.9 is the wavelength dependence of visibility in fog. One instrument that has been commercially developed is the TSI model 3563 integrating nephelometer that measures the total scattering coefficient of aerosols for three wavelengths [40]. The same idea could be employed using a forward scattering meter with three laser diodes or light emitting diodes (LED) at different wavelengths. The forward scattering angle for each wavelength can be determined and implemented. If

there is a small change in angle a detector array will have to be created to separate and filter each wavelength which will become complicated.

The benefits of this design would be seeing how different fog conditions can affect the visibility at different wavelengths. This would be important to help verify the discussion in section 2.9. This design would provide a unique forward scattering meter compared to what is available on the market since most commercial variants use infrared light. The proposed variant of FSM will contain multiple detectors and multiple light sources compared to the original design in this thesis.

7.2.2 Multi-Angle Measurements to Determine Wavelength Dependence of Extinction

This idea is proposed based off of reading two papers by Peng and Li on multi-angle forward scattering measurements to account for the wavelength dependence on scattering in fog [41] [42]. Both papers take into account similar scattering properties, visibility constraints, and wavelength dependence on visibility as chapter 2 of this thesis. Both [41] and [42] use a forward scattering angle of 35° for visibility measurements at $0.850 \mu\text{m}$ along with another forward scattering angle. In [41] two other forward scattering angles are measured at 20° and 50° to determine the parameter, q , in equation 2.9.2. The same is done in [42] but instead, the forward scattering angles of 35° and 90° are used to determine the q parameter. The ratio of the aforementioned scattering angles is taken to determine, q , based on the fact that the ratio of forward scattering angles is fixed for various kinds of aerosol content in the atmosphere.

To determine the forward scattering angles an approximation of the phase function in equation 2.5.58 is used called the Henyey-Greenstein phase function

(HGPF). The HGPF approximates the SSPF using the asymmetry parameter, as defined in chapter 2.5.5, which can be estimated for different weather conditions. This estimation of the asymmetry parameter used in [41] and [42] can be studied by applying computational Mie theory to determine the asymmetry of various aerosol distributions. The results of this can be used to build a multi-angle FSM using the same ideas proposed by Peng and Li [41] [42].

In summary, the ratio of the forwarding scattering angles for different weather conditions in haze, mist, or fog can determine which value of q will be used to determine the wavelength dependence of visibility in equation 2.9.2. This can be done by measuring two pre-calculated forward scattering angles and taking their ratio. The ratio is predefined and fixed for different weather conditions such as haze, mist, fog, and precipitation. The proposed FSM will contain a single light source and up to three forward angles photodetectors to determine the wavelength dependence of the extinction coefficient and visibility.

7.2.3 Multi-Angle Single Scattering Phase Function Measurements

Another add-on that can be studied is using a rotatable detector to measure the full phase function of aerosol distributions. This will be useful in confirming what kind of phase functions are produced by various aerosol distributions. This kind of measurement is similar to that of a polar nephelometer which estimates the total scattering coefficient by measuring the amount of scattered light at various forward angles and integrating over all angles [8]. The FSM proposed will contain a fixed forward scattering angle and up to two detectors that can swivel about the scattering volume to measure various scattering angles to build the shape of the SSPF.

This kind of measurement will be tricky in the atmosphere due to the constant transient in the particle distribution that will affect the SSPF. The best way to determine the phase function would be to pick an averaging time for each angle and quickly perform the measurement at specific angle increments to build the phase function before the aerosol distribution and concentration vary too much. The measurements would be similar to that of Sakunov [37] who measured light scattering phase functions over the world's various oceans.

7.2.4 Inclusion of Precipitation

A drawback of the current 150 ml FSM design is the inaccuracy of visibility measurements in precipitation. To measure visibility accurately in precipitative conditions is important since visibility is severely impaired in rainfall and snow. Commercial visibility meters take these conditions into account already such as the Vaisala FD12P using a rainfall meter in conjunction with the visibility optics.

To determine conditions in rainfall and snow the size distributions of rain and snow must be included. The distributions for rain that are suggested are the well-known Marshall-Palmer distributions [43]. The snow distributions must be accounted for along with rain which takes on similar exponential forms as rain but depends on the temperature and icing conditions [44] [45]. It is necessary to add precipitative conditions due to their ability to strongly impair visibility and any form of optical measurements for optical communications. The proposed FSM would contain rainfall meters for their use in determining the precipitation conditions and the inclusion of rain and snow particle distributions in Mie calculations in chapter 4.

7.2.5 Image Processing

Using the definition of visibility as defined in section 2.7 a black target can be used to determine the contrast threshold. To study the contrast using imaging methods, a black target can be viewed through the FSM sampling volume to qualitatively determine visibility. The contrast of the image could be determined through image processing techniques and calibrated to return a visibility value for various fog densities and then a qualitative visibility model could be formed.

7.3 Conclusion

The overall goal of this project is to understand how atmospheric aerosols scatter light to measure visibility in non-ideal weather conditions by constructing a forward scattering meter. The FSM is designed to measure the atmospheric extinction coefficient that can be related to visibility by Koschmieder's formula with WMO contrast guidelines. The two FSMs built in this thesis are cheaper than commercial visibility meters making it possible to build many devices if needed. The final products will then be used to calibrate the MOG's multi-aperture transmissometer alongside commercial visibility instruments. Although two finished devices have been built most testing and calibration must be done before their visibility measurements will be considered accurate.

To reach the thesis objective multiple main points of understanding were met on how to measure visibility through the atmosphere. The first main point is understanding how the atmosphere affects light propagation through attenuation described by Beer's law. The total attenuation in the atmosphere is due to absorption and scattering of light due to molecules and aerosol particles. Molecular absorption and

scattering have been considered negligible due to their small effects on total attenuation in the presence of larger aerosol particles. During non-ideal weather conditions such as haze, mist, or fog, the dominant aerosols are water-bearing particles that are better light scatterers than absorbers due to their small complex index of refraction. Mie theory and, its approximation in the small particle limit, Rayleigh theory have been applied to aerosol distributions through computational procedures. To then consider a real environment a distribution of aerosol particles must be taken into account. The computations applied to single particles are then redone to take into account various aerosol distributions to prove the operational procedure of a forward scattering meter to determine the visibility in the atmosphere. It has been determined, for the distributions used, that a forward scattering angle of 38° is best suited to measure visibility. This scattering angle creates the strongest linear relationship between the atmospheric extinction coefficient and scattered light intensity. A method has been devised to measure the extinction coefficient that can be related to the visibility by Koschmieder's formula during the daytime.

The second point of understanding how to measure visibility is by performing visibility experiments with a lab-built FSM. Two iterations of a forward scattering meter with different optical and mechanical designs to test two scattering volumes were built and tested. The first iteration contained a 2 ml volume, deemed unrepresentative of the surrounding homogenous atmosphere, so a second iteration was constructed with a 150 ml sampling volume. The 2 ml design is tested against a Vaisala visibility meter to confirm the forward scattering meter theory, operating procedure, and calibration procedure. Two experiments with the 2 ml design were performed in Florida which

taught many lessons on how to use an optical instrument outside in the presence of a large background light source. Along with lessons on averaging over a data set to obtain a meaningful extinction coefficient measurement absent of small fluctuations. The experiments also provided insight into how the scattering volume of the device affects measurements. If the device has too small a scattering volume it becomes prone to aerosol clumping which is resolved by increasing the scattering volume. By increasing the scattering volume, the extinction coefficient is averaged over a larger volume decreasing the effect of aerosol clumps. The confirmation of these procedures is important since they carry directly over to the new 150 ml FSM design due to the electronics, calibration, and data acquisition methods remaining constant.

The 150 ml FSM was testing against the 2 ml FSM using a humidifier to qualitatively see their performance against each other. This is used to confirm the design of the 150 ml FSM which is then tested in various conditions including clear weather, medium-heavy rain, and light to heavy fog. The first iteration of the 150ml FSM is deemed to be successful due to its capabilities to distinguish between various kinds of weather with visual confirmation. The 150 ml FSM has yet to be compared to a commercial visibility meter to solidify these conclusions. This will be done on the next trip to Florida with UCF. This thesis' goal of devising a lab built FSM based off of first principles has been completed but there many areas for further improvement.

Appendix

Mie Scattering Code

The general Mie Scattering code presented in this paper has been uploaded to my GitHub account for general use and any public comments.

GitHub Repository: <https://github.com/NateFe/Mie-Scattering-Code>

The code below is used as a base to build polar distribution plots and numeric integration algorithms.

Mazin Mustafa (2019).

Polar_dB (https://www.mathworks.com/matlabcentral/fileexchange/67721-polar_db), MATLAB Central File Exchange.

Retrieved January 17, 2019.

Jered Wells (2012).

Simpson's 1/3 and 3/8 Rules

(<https://www.mathworks.com/matlabcentral/fileexchange/33493-simpson-s-1-3-and-3-8-rules>), MATLAB Central File Exchange.

Retrieved August 6th 2018.

Code for ADS1256 ADC

The code used on the Raspberry PI B+ to use the ADS1256 for experimental applications is provided below along with the header files to compile it.

GitHub Repository: <https://github.com/NateFe/ADS1256>

References

- [1] World Meteorological Organization, "Guide to Meteorological Observing and Information Distribution Systems for Aviation Weather Services," World Meteorological Organization, Geneva, 2014.
- [2] Cornell Law School, "14 CFR § 135.609 - VFR ceiling and visibility requirements for Class G airspace.," 2019. [Online]. Available: <https://www.law.cornell.edu/cfr/text/14/135.609>. [Accessed 13 March 2019].
- [3] D. A. Paulson, C. Wu, J. R. Rzasas, J. Ko, M. Van Iersel, J. Coffaro, C. Smith, R. Crabbs and C. C. Davis, "A multi-aperture laser transmissometer for detailed characterization of laser propagation over long paths through the turbulent atmosphere," in *SPIE Optical Engineering + Applications, 2018*, San Diego, 2018.
- [4] Vaisala, "Transmissometer LT31," 2018. [Online]. Available: <https://www.vaisala.com/en/products/instruments-sensors-and-other-measurement-devices/weather-stations-and-sensors/lt31>. [Accessed 2 April 2019].
- [5] A. A. Rahmah, W. P. Arnott and H. Moosmuller, "Integrating nephelometer with a low truncation angle and an extended calibration scheme," *Measurement Science and Technology*, vol. 17, pp. 1723-1732, 2006.
- [6] J. A. Garland and J. B. Rae, "An integrating nephelometer for atmospheric studies and visibility warning devices," *Journal of Physics E: Scientific Instruments*, vol. 3, pp. 275-280, 1970.
- [7] T. L. Smith and L. D. Witter, "Inexpensive Laboratory - Constructed Nephelometer," *Applied and Environmental Microbiology*, vol. 44, no. 6, pp. 1476-1478, 1982.
- [8] W. Kaller, "A New Polar Nephelometer for Measurement of Atmospheric Aerosols," *Quantitative Spectroscopy & Radiative Transfer*, vol. 87, pp. 107-117, 2004.
- [9] Ecotech, "Aurora 4000 Polar Nephelometer," 2011. [Online]. Available: <https://www.ecotech.com/wp-content/uploads/2015/02/Aurora-4000-User-Manual.pdf>. [Accessed 13 March 2019].
- [10] Scientific, Campbell, "CS120A Atmospheric Visibility Sensor," 2019. [Online]. Available: <https://www.campbellsci.com/cs120a>. [Accessed 13 March 2019].
- [11] Vaisala, "FD12P User Guide in English," 2019. [Online]. Available: <https://www.vaisala.com/en/media/5456>. [Accessed 13 March 2019].
- [12] Vaisala, "Present Weather Detectors PWD22 and PWD52," 2019. [Online]. Available: <https://www.vaisala.com/en/products/instruments-sensors-and-other-measurement-devices/weather-stations-and-sensors/pwd22-52>. [Accessed 13 March 2019].

- [13] R.M. Young Company, "Sentry Visibility Sensor Model 73000," 2019. [Online]. Available: <http://www.youngusa.com/products/15/83.html>. [Accessed 13 March 2019].
- [14] C. F. Bohren and D. R. Huffman, *Absorption and Scattering of Light by Small Particles*, New York: Wiley & Sons Inc., 1983.
- [15] H. C. van de Hulst, *Light Scattering by Small Particles*, New York: Dover Publications, Inc., 1957.
- [16] W. E. K. Middleton, *Vision Through the Atmosphere*, Toronto: University of Toronto, 1952.
- [17] M. R. Peres, *The Focal Encyclopedia of Photography 4th Edition*, Burlington: Elsevier, 2007.
- [18] W. M. Organization, "Guide to Meteorological Instruments and Methods of Observation," World Meteorological Organization, Geneva, Switzerland, 2008.
- [19] H. Kaushal, V. Jain and S. Kar, *Free Space Optical Communication*, New Delhi: Springer, 2017.
- [20] C. Li, Y. Xue, W. Von Hoyningen-Huene, J. Zhang and P. Pan, "Quantitative evaluation of uncertainties in satellite retrieval of dust-like aerosols induced by spherical assumption," *Journal of Quantitative Spectroscopy & Radiative Transfer*, vol. 126, pp. 45-57, 2014.
- [21] D. Deirmendjian, "Electromagnetic Scattering on Spherical Polydispersion," The RAND Corporation, Santa Monica, 1969.
- [22] C. Mobley, "Overview of Optical Oceanography," Sequoia Scientific, 16 February 2010. [Online]. Available: http://www.oceanopticsbook.info/view/overview_of_optical_oceanography/the_volume_scattering_function. [Accessed 23 January 2019].
- [23] D. Deirmendjian, "Scattering and Polarization Properties of Water Clouds and Hazes in the Visible and Infrared," *Applied Optics*, vol. 3, no. 2, 1964.
- [24] J. R. Howell, S. Robert and P. M. Mengüç, *Thermal Radiation Heat Transfer*, Boca Raton : Taylor & Francis Group LLC, 2010.
- [25] B. A. Bodhaine, N. B. Wood, E. G. Dutton and J. R. Slusser, "On Rayleigh Optical Depth Calculations," *Atmospheric and Oceanic Technology*, vol. 16, pp. 1854-1861, 1999.
- [26] D. Bates, "Rayleigh Scattering by Air," *Planetary and Space Science*, vol. 32, no. 6, pp. 785-790, 1984.
- [27] H. Horvath, "Atmospheric Visibility," *Atmospheric Environment*, vol. 15, no. 10/11, pp. 1785-1796, 1981.
- [28] R. Nebuloni, "Empirical Relationships Between Extinction Coefficient and Visibility in Fog," *Applied Optics*, vol. 44, no. 18, pp. 3795-3804, 2005.
- [29] I. I. Kim, M. Bruce and K. Eric, "Comparison of Laser Beam Propagation at 785nm and 1550nm in Fog and Haze for Optical Wireless Communications," in *SPIE 4214, Optical Wireless Communications III*, Boston, 2001.
- [30] G. M. Hale and M. R. Querry, "Optical Constant of Water in the 200-nm to 200-um Wavelength Range," *Applied Optics*, vol. 12, no. 3, pp. 555-562, 1973.

- [31] N. W. Service, "Restrictions to Visibility," 2001. [Online]. Available: <https://www.google.com/search?q=nws&aq=chrome.0.016.523j0j4&sourceid=chrome&ie=UTF-8>. [Accessed 27 January 2019].
- [32] B. Hassler, "Atmospheric Transmission Models for Infrared Wavelengths," Linköping University, Linköping, 1998.
- [33] W. G. Durbin, "Droplet Sampling in Cumulus Clouds," *Tellus*, vol. 11, no. 2, p. 202, 1959.
- [34] N. L. Miles, J. Verlinde and E. E. Clothiaux, "Cloud Droplet Size Distributions in Low-Level Stratiform Clouds," *Journal of the Atmospheric Sciences*, vol. 57, no. 2, 2000.
- [35] J. V. Winstanley and M. J. Adams, "Point Visibility Meter: A Forward Scatter Instrument for the Measurement of Aerosol Extinction Coefficient," *Applied Optics*, vol. 14, no. 9, 1975.
- [36] J. V. Dave, "Scattering of Electromagnetic Radiation by a Large, Absorbing Sphere," IBM, 1969.
- [37] G. Sakunov, O. D. Barteneva and R. V.F, "Experimental Studies of Light Scattering Phase Functions of the Atmospheric Surface Layer," *Atmospheric and Oceanic Physics*, vol. 31, no. 6, pp. 750-758, 1996.
- [38] J. E. Tyler, "Measurement of the Scattering Properties of Hydrosols," *Journal of the Optical Society of America*, vol. 51, no. 11, pp. 1289-1293, 1961.
- [39] G. V. Rozenberg, "Light Scattering in the Earth's Atmosphere," *Soviet Physics Uspekhi*, vol. 3, no. 3, pp. 173-213, 1960.
- [40] P. J. Sheridan and J. A. Ogren, *TSI Model 3563 Integrating Nephelometer Operations Reference Manual*, Boulder, Colorado: World Meteorological Organization, 2014.
- [41] P. Peng and C. Li, "Visibility Measurement Using Multi-Angle Forward Scattering by Liquid Droplets," *Measurement Science and Technology*, vol. 23, no. 10, 2012.
- [42] P. Peng and C. Li, "Visibility Measurements Using Two-Angle Forward Scattering by Liquid Droplets," *Applied Optics*, vol. 55, no. 15, pp. 3903-3908, 2016.
- [43] S. Kobayashi, T. Oguchi, S. Tanelli and E. Im, "Backscattering Enhancement on Spheroid-Shaped Hydrometers: Considerations in Water and Ice Particles of Uniform Size and Marshall-Palmer Distributed Rains," *Radio Science*, vol. 42, 2006.
- [44] A. J. F. P. Heymsfield and B. Aaron, "Exponential Size Distributions for Snow," *Journal of the Atmospheric Sciences*, vol. 76, no. 3, pp. 4017-4031, 2008.
- [45] C. P. Woods, T. M. Stoelinga and J. D. Locatelli, "Size Spectra of Snow Particles Measured in Wintertime Precipitation in the Pacific Northwest," *Journal of the Atmospheric Sciences*, pp. 189-205, 2008.

- [46] R. Thalman, K. J. Zarzana, T. M.A and V. R, "Rayleigh Scattering Cross-Section Measurements of Nitrogen, Argon, Oxygen, and Air," *Journal of Quantitative Spectroscopy & Radiative Transfer*, vol. 147, pp. 171-177, 2014.
- [47] W. C. Malm, "Introduction to Visibility," Colorado State University, Fort Collins, 1999.
- [48] W. Kaller, "A new polar nephelometer for measurement of atmospheric aerosols," *Journal of Quantitative Spectroscopy & Radiative Transfer* , vol. 87, pp. 107-117, 2004.